The Fabrication of PBCO Buffered Step-edge Josephson Junctions

by

Wynand Fourie van Staden

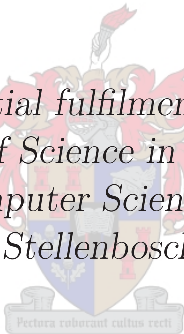

Thesis presented in partial fulfilment of the requirements for the degree of Master of Science in Engineering (Electronic Engineering with Computer Science) at the University of Stellenbosch

Supervisor: Prof W.J. Perold

March 2007

Declaration

I, the undersigned, hereby declare that the work contained in this thesis is my own original work and that I have not previously in its entirety or in part submitted it at any university for a degree.

Signature: ....

W.F. van Staden

Date: ....

Abstract

A major challenge in the design and operation of High Temperature Superconducting (HTS) devices is the fabrication of reproducible Josephson junctions with good I_cR_n products. One objective of this thesis was to fabricate successfully HTS step-edge junctions. This objective necessitated a critical evaluation of the available facilities to provide much needed improvements. These improvements included a newly optimised photolithography process, the incorporation of a three-gridded extraction system into the in-house argon ion mill as well as alterations to the Pulsed Laser Deposition (PLD) system to improve thin film quality. These process modifications finally allowed for the fabrication of novel $PrBa_2Cu_3O_{7-\delta}$ buffered step-edge junctions. These junctions were tested for dc and ac Josephson effects and displayed I_cR_n products of 1.5 mV at 55 K as well as well-defined Shapiro steps.

A second objective was to introduce a high quality thin film deposition system that could produce smooth superconducting films for use in filters and multilayer technology. An Inverted Cylindrical Magnetron system was built and optimised to grow $YBa_2Cu_3O_{7-\delta}$ thin films on MgO (001) substrates. A complete optimisation process of these films are presented by utilising several growth and electrical characterisation methods such as XRD, RBS and AFM.

Opsomming

Een van die belangrikse uitdagings in die ontwerp en werking van Hoë Temperatuur Supergeleiers is die vervaardiging van herproduseerbare "Josephson Junctions" met goeie I_cR_n produkte. Een doelwit van hierdie tesis was om "step-edge junctions" suksesvol te vervaardig. Hierdie doelwit het 'n kritiese evaluering van die beskikbare geriewe genoodsaak om nodige verbeteringe aan te bring. Dit sluit in 'n nuut-geoptimeerde fotolitografiese proses, die inkorporasie van 'n drie-plaat onttrekkingsisteem in die "argon ion mill" sowel as veranderinge aan die gepulsde laser deposisie (PLD) sisteem. Hierdie modifikasies het die geleentheid geskep om innoverende "$PrBa_2Cu_3O_{7-\delta}$ buffered step-edge junctions" te vervaardig. Die "junctions" was getoets vir moontlike gs- en ws Josephson effekte. I_cR_n produkte van 1.5 mV by 55 K sowel as wel-gedefinieerde "Shapiro steps" is waargeneem.
'n Tweede doelwit was om 'n hoë kwaliteit dun film deposisie sisteem te ontwikkel om sagte supergeleidende films te vervaardig vir gebruik in filter en multi-laag tegnologieë. 'n "Inverted Cylindrical Magnetron" sisteem was vervaardig en geoptimeer om $YBa_2Cu_3O_{7-\delta}$ dun films op MgO (001) substrate te groei. 'n Volledige optimeringsproses van hierdie films word voogelê waartydens verskeie groei- en elektriese karakteriseringsmetodes soos XRD, RBS en AFM aangewend is.

Pectora roborant cultus recti

Acknowledgements

I would like to express my sincere gratitude to the following people and organisations for contributing to my research.

First and foremost a special thanks goes out to my research advisors, Prof. W.J. Perold and Dr. C.J. Fourie. An important thanks to Ulrich Buttner for his insight and technical support in countless situations. Without your assistance, this thesis could not have reached its full potential.

Furthermore I would like to acknowledge the following persons involved in post-deposition characterization of YBCO samples: Dr. Chris Theron from iThemba Labs for your help and expertise with the RBS measurements and to Akram Elkaseh for countless hours spend performing AFM analyses. Thanks to the physics department for allowing me the use of the laser system as well as to the chemistry department for the use of the XRD unit. I would also like to thank and acknowledge the National Research Foundation that provided funding to make this research possible.

I would like to express my thanks to my colleagues and friends, Hennie de Villiers and Hein van Heerden for always being willing to listen and to give advice.

Finally, I would like to thank my family for their continuous support, understanding and encouragement during my studies.

Contents

Declaration **i**

Abstract **ii**

Opsomming **iii**

Acknowledgements **iv**

Contents **v**

List of Figures **viii**

List of Tables **xii**

Acronyms **xiii**

1 Introduction **1**

1.1 Historic Overview 1

1.2 Thesis Outline 2

2 Josephson Junctions **4**

2.1 The Josephson Effects 4

2.2 Modeling the Josephson Junction 7

2.3 DC Characteristics of Josephson Junctions 8

2.4 RF Characteristics of Josephson Junctions 10

2.5 Magnetic Behaviour of Josephson Junctions 13

2.6 High-Temperature Superconductor Josephson Junctions 15

2.7 Grain Boundary Junctions 15

2.8 Extrinsic Barrier Junctions 19

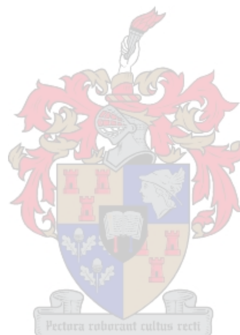

2.9 General Properties of HTS Josephson Junctions . . . 20
2.10 Chapter Overview . . . 20

3 Photolithography 21
3.1 Process Description . . . 21
3.2 Process Optimisation . . . 24
3.3 Chapter Overview . . . 26

4 Argon Ion Milling 27
4.1 The Argon Mill System . . . 27
4.2 Initial Optimisation . . . 30
4.3 Gridded Accelerator System . . . 31
4.4 Etch Profiles . . . 40
4.5 Chapter Overview . . . 43

5 Thin Film Deposition: Pulsed Laser and DC Magnetron Deposition 44
5.1 Theory of Thin Films . . . 44
5.2 Substrate Considerations . . . 48
5.3 Growth Mechanisms in PVD . . . 49
5.4 Conventional Pulsed Laser Deposition . . . 51
5.5 Inverted Cylindrical Magnetron Sputtering . . . 53
5.6 Chapter Overview . . . 56

6 Characterisation of YBCO Films Deposited by ICM 57
6.1 X-Ray Diffraction . . . 57
6.2 Rutherford Backscattering Spectroscopy . . . 58
6.3 Atomic Force Microscopy . . . 60
6.4 Susceptibility Tests . . . 60
6.5 Characterisation of ICM . . . 61
6.6 Experiments . . . 63
6.7 Chapter Overview . . . 82

7 Buffered Step-edge Josephson Junctions 83
7.1 Underlying Mechanisms in Step-Edge Junction Formation . . . 83
7.2 General Properties of Step-Edge Junctions . . . 85
7.3 History of Step-edge Fabrication at Stellenbosch . . . 86

Pectora roborant cultus recti

7.4 Step-edge Fabrication . . . 86
7.5 Step Patterning . . . 87
7.6 Annealing of Steps . . . 101
7.7 Thin Film Deposition . . . 102
7.8 Circuit Patterning: Photolithography and Argon Milling . . . 103
7.9 Establishing Electrical Contact . . . 105
7.10 Chapter Overview . . . 107

8 Experimental Results 108
8.1 IV-Characteristics . . . 108
8.2 Test Setup . . . 109
8.3 Buffered Step-edge Measurements . . . 111
8.4 Chapter Overview . . . 118

9 Conclusion and Recommendations 119
9.1 Thesis Review . . . 119
9.2 Future Research Proposals . . . 121
9.3 Conclusion . . . 122

List of References 123

Appendices 128

A $PB_2C_3O_{7-\delta}$ Fabrication 129

B Bicrystal Fabrication 131

C Argon Ion Mill Operation Procedure 134

D ICM Operation 138

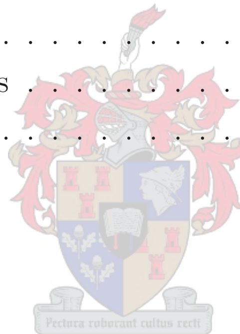

List of Figures

2.1 A SIS Tunnel junction 5
2.2 Equivalent circuit model for a Josephson junction element 7
2.3 Current-Voltage characteristics for different values of β_c 10
2.4 The Voltage Source Model 10
2.5 Theoretical IV characteristics according to the Voltage Source Model 12
2.6 The Current Source Model 12
2.7 Illustration of experimentally observable Shapiro steps 13
2.8 I_c as a function of the flux, Φ, in the junction 14
2.9 Schematic illustration of (a) a [001]-tilt boundary, (b) a [100]-tilt boundary and (c) a [100] twist grain boundary 16
2.10 A grain boundary illustrating a region of disorder where the two lattices mismatch 16
2.11 Three popular types of grain boundary junctions 17
2.12 A Ramp-edge junction 19

3.1 An example of an under-exposed mask pattern on YBCO 25
3.2 The effect of under-development (left) and over-development (right) 25
3.3 Shadowing of the resist profiles caused by excess resist (left) and after edge bead removal with gap free contact (right) 25
3.4 Ineffective resist removal after exposure to excessive heat 25
3.5 Optimal resist sidewall profile 26

4.1 Matching Network of the Argon Mill 28
4.2 Old Extraction System used for Argon Ion Milling 29
4.3 Resist on 2 x 2 cm^2 Alumina substrates milled for 45 minutes at various working distances (WDs) below the extraction plates 30

Pectora roborant cultus recti

4.4 An illustration of apertures used with their corresponding etch profile below. These etch runs were done on 2 x 2 cm^2 Alumina substrates covered with resist or gold . . . 31
4.5 Illustration of beam extraction under typical operating conditions . . . 32
4.6 Electric field distribution for increased plasma density . . . 33
4.7 Potential distribution through grids (V_P denotes the plasma potential) . . . 34
4.8 Milled resist on an Alumina substrate illustrating the spot size obtained with the 3-gridded extraction system . . . 35
4.9 Illustration of an electron source . . . 38
4.10 Plasma Bridge Neutraliser . . . 39
4.11 Complete Three-gridded Ion Beam System . . . 39
4.12 Isotropic and anisotropic etch profiles . . . 40
4.13 Features characteristic to ion milling . . . 41
4.14 Typical etch resolution obtainable for circuit patterning . . . 42
4.15 A three dimentional view of an edge profile . . . 42

5.1 Illustration of heteroepitaxial growth for lattice-matched, strained and relaxed structures . . . 46
5.2 Layer-by-layer growth . . . 46
5.3 Stepflow growth . . . 47
5.4 Island growth . . . 47
5.5 Mixed growth . . . 48
5.6 A conventional Pulsed Laser Deposition system . . . 51
5.7 Pulsed Reactive Crossed-Beam Laser Ablation . . . 53
5.8 Schematic view of Magnetron Sputtering System . . . 54

6.1 The scattering of X-rays from atomic planes . . . 58
6.2 Backscattering of incident alpha particles by a stationary target atom . . . 59
6.3 The effect on arc voltage for varying O_2 partial pressure . . . 62
6.4 Growth Characterisation Measurements for an O_2:Ar ratio of 1:2 . . . 65
6.5 Growth Characterisation Measurements for an O_2:Ar ratio of 1:1 . . . 66
6.6 Growth Characterisation Measurements for an O_2:Ar ratio of 2:1 . . . 67
6.7 Growth Characterisation Measurements for an O_2:Ar ratio of 4:1 . . . 68
6.8 (a) Stoichiometry and (b) RMS Roughness as a function of oxygen partial pressure 69

Pectora roborant cultus recti

6.9 Susceptibility Tests for Oxygen/Argon ratios of (a) 1:2 (b) 1:1 (c) 2:1 and (d) 4:1 at a constant total pressure of 150 μmHg . . . 70
6.10 Growth Characterisation Measurements for a Total Pressure of 225 μmHg . . 72
6.11 Growth Characterisation Measurements for a Total Pressure of 300 μmHg . . 73
6.12 (a) Stoichiometry and (b) RMS Roughness as a function of total pressure . . . 74
6.13 Susceptibility tests for varying total pressures of (a) 225 μmHg and (b) 300 μmHg . . . 74
6.14 Growth Characterisation Measurements for a Substrate Temperature of 680°C 76
6.15 Growth Characterisation Measurements for a Substrate Temperature of 700°C 77
6.16 Growth Characterisation Measurements for a Substrate Temperature of 720°C 78
6.17 Growth Characterisation Measurements for a Substrate Temperature of 760°C 79
6.18 (a) Stoichiometry and (b) RMS Roughness as a function of substrate temperature 80
6.19 Susceptibility Tests for Temperature Variation with T_{dep} (a) 680°C, (b) 700°C, (c) 720°C and (d) 760°C . . . 81

7.1 Grain boundary formation on a perovskite substrate with a 45° step-edge . . . 84
7.2 Typical grain boundary formation on a non-perovskite substrate step-edge . . 85
7.3 Model of step-edge process . . . 88
7.4 Shading angle as a function of β . . . 90
7.5 Etch rates of (a) MgO and (b) SPR700 photoresist as a function of beam angle 91
7.6 Relative etch rates as a function of ion-beam angle . . . 91
7.7 Step angle as a function of shading angle . . . 92
7.8 Step profile in (a) 3D and (b) 1D for $\beta = 0^o$ and $\omega = 17^o$ . . . 93
7.9 Step profile in (a) 3D and (b) 1D for $\beta = 20^o$ and $\omega = 11^o$ . . . 93
7.10 Step profile in (a) 3D and (b) 1D for $\beta = 45^o$ and $\omega = 8^o$ . . . 93
7.11 Predicted and measured MgO step angles . . . 94
7.12 Lift-off of a niobium metal mask . . . 95
7.13 XRD analysis of a PBCO thin film deposited at 700°C . . . 98
7.14 XRD analysis of a PBCO thin film deposited at 720°C . . . 98
7.15 AFM analysis of PBCO thin films deposited at (a) 700°C and (b) 720°C . . . 99
7.16 Results of PBCO etching: (a) PBCO etch rates and (b) relative etch rates . . 100
7.17 Predicted versus measured PBCO step angles . . . 101
7.18 Step profile of a PBCO step-edge for $\alpha = 60^o$, $\beta = 15^o$ and $\omega = 25^o$ . . . 101
7.19 Optical microscope images of milled step (a) before and (b) after an YBCO layer is deposited . . . 103

7.20 Susceptance measurement of YBCO film on PBCO step 103
7.21 Chrome mask used during contact exposure 104
7.22 Optical microscope images of (a) patterned photoresist before milling (b) patterned YBCO after milling 105
7.23 PCB used for circuit packaging 106
7.24 Illustration of 4 wirebonds on a gold pad 107

8.1 A depiction of junction-like and flux-flow behaviour 110
8.2 Schematic of the basic test setup 110
8.3 Measured IV characteristics at 70 K 111
8.4 (a) I_c and (b) R_n as a function of temperature 112
8.5 Shapiro Steps measured at 40 K at 8.891 GHz 114
8.6 (a) I_c and (b) R_n as a function of temperature for the second 10 μm track . . 115
8.7 (a) The measured IV-characteristic at 70 K and (b) the corresponding Shapiro steps at 11.54 GHz 116
8.8 (a) I_c and (b) R_n as a function of temperature for a 6 μm track 116

A.1 Temperature profile for bake process of PBCO target 130

B.1 Illustration of bicrystalline 132

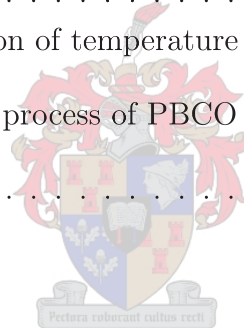

List of Tables

3.1 Optimal parameter set for MgO, YBCO and PBCO materials 24

4.1 Ion current as a function of RF power 36
4.2 Optimal mill parameters for 2 modes of operation 37

5.1 Properties of popular HTS substrates [1] 49

6.1 Deposition rates for varying O_2:Ar ratios 69
6.2 Superconducting properties for varying O_2:Ar ratios 70
6.3 Deposition rates for varying total pressure 74
6.4 Superconducting properties for varying total pressure 75
6.5 Deposition rates for varying substrate temperature 80
6.6 Superconducting properties for varying substrate temperature 81
6.7 Optimal parameter set for YBCO deposition with ICM 82

7.1 Measured surface roughnesses for 6 PBCO depositions 99
7.2 Optimal parameter set for PBCO deposition 99
7.3 Optimal parameter set for YBCO deposition 102
7.4 Parameter set for Argon Ion milling of YBCO 104
7.5 Optimal parameter set for gold deposition 106

A.1 Compound weights used for PBCO fabrication 129

B.1 Parameter set used for bicrystalline milling 132
B.2 The parameter set used for gold deposition 133

Acronyms

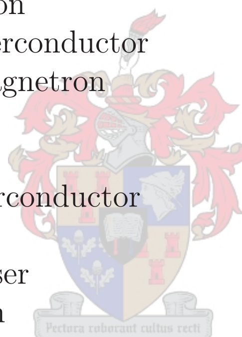
Pectora roborant cultus recti

ac	Alternating Current
AFM	Atomic Force Microscopy
CD	Critical Dimension
dc	Direct Current
FIB	Focused Ion Beam
GBJ	Grain Boundary Junction
HTS	High Temperature Superconductor
ICM	Inverted Cylindrical Magnetron
IV	Current-Voltage
JJ	Josephson Junction
LTS	Low Temperature Superconductor
PBCO	$Pr_1Ba_2Cu_3O_{7-\delta}$
PBN	Plasma-bridge Neutraliser
PLD	Pulsed Laser Deposition
PVD	Physical Vapour Deposition
RBS	Rutherford Backscattering Spectroscopy
RSFQ	Rapid Single Flux Quantum
RCSJ	Resistively and Capacitively Shunted Model
rf	Radio Frequency
SEJ	Step-Edge Junction
SGB	Symmetric Grain Boundary
SIS	Superconductor/Insulator/Superconductor
SQUID	Superconducting Quantum Interference Device
TEM	Transmission Electron Microscope
UV	Ultra-Violet
XRD	X-Ray Diffraction
YBCO	$Y_1Ba_2Cu_3O_{7-\delta}$

Chapter 1

Introduction

1.1 Historic Overview

The discovery of high-temperature superconductivity (HTS) by Bednorz and Müller in 1986 marked the beginning of an exciting new era in the field of superconductivity. The first HTS material to be discovered was $La_{2-x}Ba_xCuO_{4-y}$ which demonstrated a critical temperature, T_c, of 30 K. Other cuprate oxides with superconducting transition temperatures exceeding the boiling point of liquid nitrogen (77 K) were soon discovered.

Today, reproducible preparation techniques for a number of HTS materials are available. Research tended to converged on two major compounds: $YBa_2Cu_3O_{7-\delta}$ and the bismuth compound Bi-Sr-Ca-Cu-O. The vast application potential of these HTS materials has driven significant efforts in exploring their formation as thin films. This led to the development of innovative deposition techniques to grow these films epitaxially, such as co-evaporation, molecular beam epitaxy, pulsed laser deposition, sputtering and liquid-phase epitaxy.

The efforts to synthesise high quality thin films were matched by intense research on Josephson junctions in HTS materials. The development of this technology was pioneered by work done by IBM on bicrystal junctions in 1988 [2]. Since then several other HTS junction technologies have emerged such as step-edge junctions, biepitaxial junctions and ramp-edge junctions. The vision to manufacture Josephson junctions with acceptable parameter spreads have, however, eluded researchers over the past twenty years.

Continued research of high-temperature superconductors is warranted by the advantages

offered over their semiconductor counterparts. This include the ability of a Josephson junctions to switch from a zero to a finite voltage state within a few picoseconds with minimal power dissipation. Superconducting microstrip transmission lines are also able to transfer picosecond waveforms with low attenuation, dispersion and crosstalk. These attributes make this technology ideal for application in high precision and high-frequency electronics. Additionally, these junctions can be configured into superconducting quantum interference devices (SQUIDs) capable of detecting minute magnetic fields.

1.2 Thesis Outline

The scope of this thesis is quite broad. The initial objective to fabricate step-edge Josephson junctions was always seen as the conclusion to this research, but required a study of several underlying processes. The chapter progression will illustrate this fact.

- Chapter 2 gives a theoretical background into the operation of the generalised Josephson junction (JJ) in response to dc and ac excitation. This description is extended to High Temperature Superconductor JJs with special focus on grain boundary junctions.

- Chapter 3 provides a brief description of the underlying mechanisms of photolithography. The entire process is accordingly optimised in preparation for dry etching.

- Chapter 4 introduces the Argon ion mill and identifies and solves relevant problems to yield homogeneous etch profiles.

- In Chapter 5 the basic theory of thin film deposition is presented. This if followed by a brief description of the Pulsed Laser Deposition (PLD) system and the introduction of a newly designed Inverted Cylindrical dc Magnetron (ICM) system.

- Four methods of thin film characterisation are listed in Chapter 6. These methods are subsequently used in the optimisation process for YBCO thin films deposited by ICM.

- Chapter 7 presents a method to successfully fabricate PBCO buffered step-edge junctions on (001) MgO substrates. The method is aided by a theoretical model to predict dry etching characteristics.

Pectora roborant cultus recti

- In Chapter 8 the fabricated junctions are tested for IV-characteristics. Tests included determining critical currents, normal resistances, the presence/absence of Shapiro steps and the magnetic modulation characteristics.

- Finally, Chapter 9 gives an overview of the research done followed by some recommendations for future research projects.

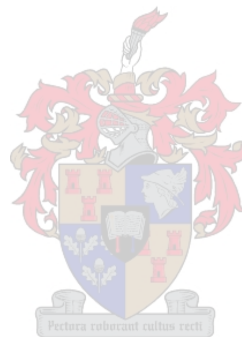

Chapter 2

Josephson Junctions

The active device in superconducting electronics is the Josephson junction, first proposed by Brian Josephson in 1962 [3]. In its simplest form, this device consists of two superconducting electrodes weakly coupled by a thin insulating barrier that allows quantum mechanical tunneling of Cooper pairs from one electrode to the other. From an engineering perspective, interest in Josephson junctions are fueled by the prospect of incorporating these devices into complex Rapid Single Flux Quantum (RSFQ) circuits operating at ultrafast speeds of several hundred gigahertz [4].

One of the main objectives in this thesis is to fabricate and characterise HTS Josephson junctions successfully. Accordingly, this chapter focuses on the development of a qualitative model for the generalised Josephson junction, followed by a discussion on the structural and electrical properties of HTS junctions.

2.1 The Josephson Effects

Initial research of Josephson junctions were predominantly performed on so-called tunnel junctions (see Fig. 2.1). Today, this junction geometry is well understood and plays a prominent role in low-temperature superconducting electronics. For these reasons, it makes sense to use the tunnel junction to introduce general concepts concerning Josephson junction operation.

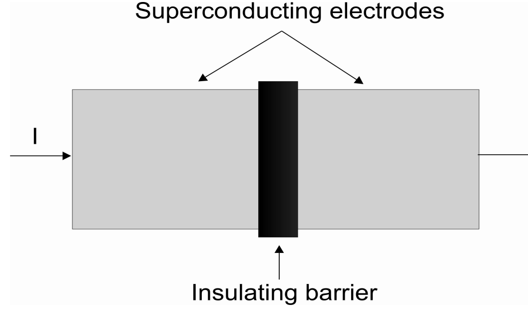

Figure 2.1: A SIS Tunnel junction

On a macroscopic level, Josephson junctions demonstrate two characteristic effects. The first effect is a zero voltage supercurrent that flows through the insulating barrier when a difference in wavefunction phase exists between the superconducting electrodes. The second effect is observed when the junction is biased with a dc voltage, resulting in a time-varying phase difference. These effects are known as the dc- and ac Josephson effects respectively.

To gain some insight into the mechanisms governing these effects, a simple but elegant derivation of the Josephson relations for an arbitrary location in the plane of the junction will be given (as suggested by R.P. Feynman [5]).
From general superconductor theory, it is known that a superconducting condensate can be described by a single macroscopic wavefunction $\Psi(\vec{r}) = |\Psi(\vec{r})|e^{i\theta(\vec{r})}$ known as the order parameter. It is helpful to think of this parameter as the centre of mass motion of the Cooper pair. In a superconductor/insulator/superconductor (SIS) structure such as a tunnel junction, the wavefunctions in the respective superconducting electrodes become weakly coupled. The resulting time evolution of the coupled wavefunctions can now be formulated as

$$i\hbar\frac{\partial\Psi_1}{\partial t} = U_1\Psi_1 + K\Psi_2 \tag{2.1.1}$$

$$i\hbar\frac{\partial\Psi_2}{\partial t} = U_2\Psi_2 + K\Psi_1 \tag{2.1.2}$$

where U_1 and U_2 represent the energies of the wavefunctions and K is the coupling factor signifying the interaction between the wavefunctions. By assuming a voltage source is applied between the two electrodes, an energy difference $e^*(V_2 - V_1) = e^*V$ will result so

that $U_2 - U_1 = e^*V$, where $e^* = -2e$. By now taking the zero of energy midway between U_1 and U_2, (2.1.1) and (2.1.2) become

$$i\hbar\frac{\partial\Psi_1}{\partial t} = \frac{-e^*V}{2}\Psi_1 + K\Psi_2 \tag{2.1.3}$$

$$i\hbar\frac{\partial\Psi_2}{\partial t} = \frac{e^*V}{2}\Psi_2 + K\Psi_1. \tag{2.1.4}$$

For convenience the wavefunction can be expressed in terms of the Cooper pair density, n_s^*, formulated as

$$\Psi_k = \sqrt{n_{sk}^*}e^{i\theta_k} \tag{2.1.5}$$

where $k = 1$ or 2. After Substituting (2.1.5) into (2.1.3) and (2.1.4), separating real and imaginary terms and defining the phase difference $\varphi = \theta_2 - \theta_1$, the following equations result:

$$\frac{\partial n_{s1}^*}{\partial t} = \frac{2}{\hbar}K\sqrt{n_{s1}^* n_{s2}^*}sin\varphi \tag{2.1.6}$$

$$\frac{\partial n_{s2}^*}{\partial t} = -\frac{2}{\hbar}K\sqrt{n_{s1}^* n_{s2}^*}sin\varphi \tag{2.1.7}$$

$$\frac{\partial\theta_1}{\partial t} = -\frac{K}{\hbar}\sqrt{\frac{n_{s2}^*}{n_{s1}^*}}cos\varphi + \frac{e^*V}{2\hbar} \tag{2.1.8}$$

$$\frac{\partial\theta_2}{\partial t} = -\frac{K}{\hbar}\sqrt{\frac{n_{s1}^*}{n_{s2}^*}}cos\varphi - \frac{e^*V}{2\hbar} \tag{2.1.9}$$

From (2.1.6) and (2.1.7), it is evident that the rate of decrease of pair density in one superconductor is the negative of the other. The current through the junction must be equal to this change in density and is therefore equal to $\frac{\partial n_{s1}^*}{\partial t} = -\frac{\partial n_{s2}^*}{\partial t}$, or

$$J = \frac{2}{\hbar}K\sqrt{n_{s1}^* n_{s2}^*}sin\varphi = J_c sin\varphi \tag{2.1.10}$$

where J_c is the critical current density and reflects the strength of the electrode coupling. By subtracting (2.1.8) from (2.1.9) and equating n_{s1}^* and n_{s2}^*, the time evolution of the phase difference across the junction can be obtained as

$$\frac{\partial \varphi}{\partial t} = \frac{2e}{\hbar} V. \tag{2.1.11}$$

Equations (2.1.10) and (2.1.11) are the famous Josephson relations which form the basis of understanding the behaviour of JJs.

2.2 Modeling the Josephson Junction

The Josephson relations alone cannot account for all demonstrated junction characteristics. A Josephson junction can instead be modeled phenomenologically as a lumped circuit element consisting of a Josephson element (governed by the Josephson relations) in parallel with a resistor and a capacitor. This model is called the Resistively and Capacitively Shunted Junction (RCSJ) model (see Fig. 2.2).

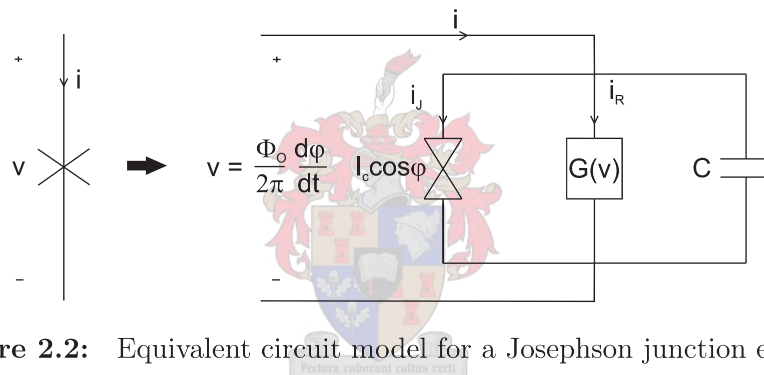

Figure 2.2: Equivalent circuit model for a Josephson junction element

2.2.1 Junction Resistance and Capacitance

On a microscopic level, the junction resistance can be thought of as the breaking of Cooper pairs into normal electrons that tunnel across the insulating barrier. Cooper pairs can become unbound if a voltage exceeding twice that of the energy gap value is applied to the junction. The resistance associated with this normal-electron-tunneling is appropriately called the normal resistance, R_n. This description of the junction resistance is, however, incomplete. According to the two fluid model, normal electrons already exist in a superconductor at non-zero temperatures without applying voltage. The resistance in this region is denoted by $R_{sg}(T)$, called the subgap resistance. A complete representation of the junction conductance is now given by

$$G(v) = \begin{cases} \frac{1}{R_{sg}(T)} & if \ \ |v| < 2\Delta(T)/e \\ \frac{1}{R_n} & otherwise. \end{cases} \tag{2.2.1}$$

To complete the model for a generalised Josephson junction, a capacitive channel should be included to account for the displacement current which flows between the superconducting electrodes. For tunnel junctions this capacitance can be formulated as that for a parallel plate capacitor,

$$C = \frac{\epsilon_0 \epsilon_\mu A}{d} \tag{2.2.2}$$

where d is the thickness of the barrier and A is the area of the superconducting electrodes. The influence of the capacitive channel is sometimes ignored due to the dominating effect of the resistive channel. This simplified model is known as the Resistive Shunted Junction (RSJ) model.

In spite of its simplicity and the availability of more sophisticated theories, the RCSJ model remains popular. It gives a reasonable approximation of the measured IV-characteristics of Josephson junctions and is easy to implement in models of larger electronic circuits [6].

2.3 DC Characteristics of Josephson Junctions

Pectora roborant cultus recti

Using the RCSJ model as an accurate representation of the Josephson junction, insight can be gained into junction behaviour when excited by either a dc or an ac source. When a dc driving current, i, is connected to the junction, combining Kirchhoff's current law and the voltage phase relation reveal

$$i = I_c sin\varphi + \frac{1}{R}\frac{\Phi_o}{2\pi}\frac{d\varphi}{dt} + C\frac{\Phi_o}{2\pi}\frac{d^2\varphi}{dt^2}. \tag{2.3.1}$$

For convenience, the conductance channel is replaced by a constant resistive value, R. By rewriting this equation with dimensionless parameters it follows that

$$\frac{i}{I_c} = sin\varphi + \frac{d\varphi}{d\tau} + \beta_c \frac{d^2\varphi}{d\tau^2} \tag{2.3.2}$$

where

$$\tau = \frac{t}{\tau_J}, \tag{2.3.3}$$

$$\tau_J = \frac{\Phi_o}{2\pi}\frac{1}{I_c R} \tag{2.3.4}$$

and

$$\beta_c = \frac{RC}{\tau_J} = \frac{\tau_{RC}}{\tau_J}. \tag{2.3.5}$$

From these equations, it is clear that the dc operation of the circuit is governed by two characteristic times: τ_{RC} associated with the resistive/capacitive elements and τ_J, associated with the basic junction element. The ratio of these two time constants is called the Stewart-McCumber parameter, β_c. This parameter gives an indication of the relative importance of junction capacitance on junction behaviour. The circuit dynamics will be explained by considering two limiting cases where $\beta_c \ll 1$ and $\beta_c \gg 1$, before the general case is addressed.

When $\beta_c \ll 1$, $\tau_{RC} \ll \tau_J$ implying that the circuit dynamics follows the evolution of junction phase, φ. The effect of the capacitive channel can thus be neglected from the model, resulting in the non-hysteretic I-V characteristic as depicted in Fig. 2.3(a). The junction voltage is now given by:

$$\langle v(t)\rangle = \begin{cases} 0 & for\ i < I_c \\ iR\sqrt{1-(\frac{I_c}{i})^2} & for\ i > I_c \end{cases} \tag{2.3.6}$$

When $\beta_c \gg 1$, $\tau_{RC} \gg \tau_J$ and the resistive/capacitive combination dominates circuit behaviour. For the operating region where $i < I_c$, there still exist a possibility for Josephson current to flow (assuming the initial current is zero). If, however, a finite voltage state has been reached, the circuit operation would exhibit hysteresis introduced by the capacitive channel. In this region,

$$\langle v(t)\rangle = iR, \tag{2.3.7}$$

and the corresponding I-V curve follows a straight line as shown in Fig. 2.3(b).

For the general case, a quantity $\frac{i_{min}}{I_c}$ can be defined to illustrate the amount of hysteresis that will occur. As $\beta_c \to \infty$, $\frac{i_{min}}{I_c} \to 0$ and as $\beta_c \to 0$, $\frac{i_{min}}{I_c} \to 1$ (see Fig. 2.3(c)).

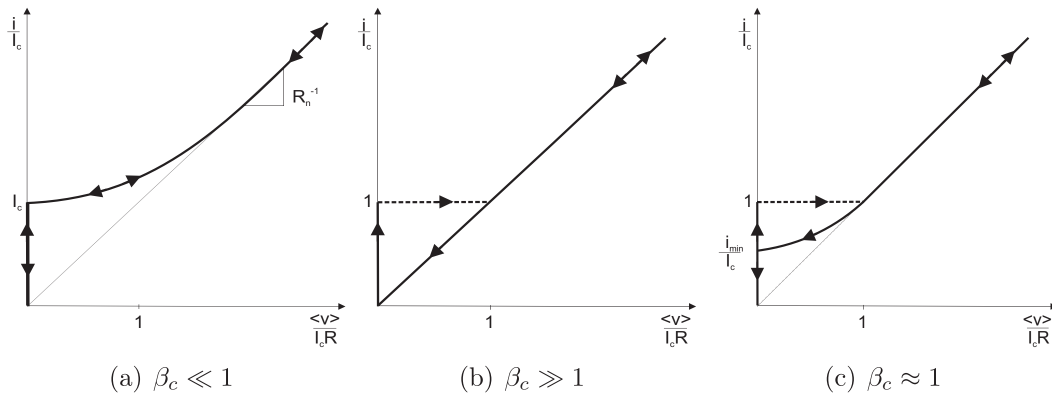

(a) $\beta_c \ll 1$ (b) $\beta_c \gg 1$ (c) $\beta_c \approx 1$

Figure 2.3: Current-Voltage characteristics for different values of β_c

2.4 RF Characteristics of Josephson Junctions

To gain an appreciation for the RF operation of a Josephson junction, two operating scenarios have to be considered. The first case employs dc and ac voltage sources (zero internal impedance) as a means of excitation while the second uses dc and ac current sources (infinite internal impedance). By utilising voltage sources in our initial model, analytical results will be obtained which can be qualitatively transformed to incorporate the response to current sources. Both models will assume that the junction capacitance is negligible and $\beta_c \ll 1$.

2.4.1 Voltage Source Model

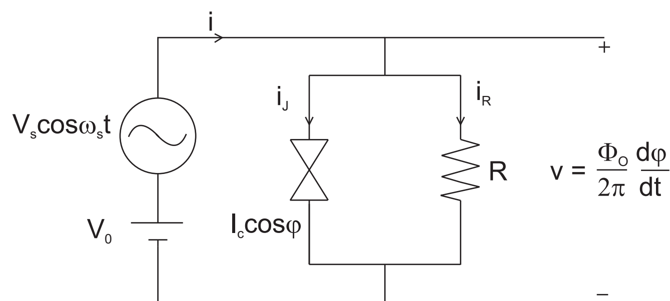

Figure 2.4: The Voltage Source Model

For the voltage source model (as depicted in Fig. 2.4), the applied voltage is given by

$$v(t) = V_0 + V_s cos \omega_s t. \tag{2.4.1}$$

The resulting current through the junction is given by

$$i_J(t) = I_c \sum_{n=-\infty}^{n=\infty} (-1)^n J_n(\frac{2\pi V_s}{\Phi_0 \omega_s}) sin[(2\pi f_J - n\omega_s)t + \varphi(0)] \tag{2.4.2}$$

where $f_J = \frac{V_o}{\Phi_o}$ and $\varphi(0)$ is a constant of integration. The corresponding current through the resistive channel is

$$i_R(t) = \frac{V_o}{R} + \frac{V_s}{R} cos\omega_s t, \tag{2.4.3}$$

giving a total current

$$i(t) = i_R + i_J. \tag{2.4.4}$$

The dc component of the current, $\langle i \rangle$, is the superposition of the average dc current through the resistor and the basic junction. The current through the junction is made up of a series of sinusoidally time dependent terms. Consequently its dc component will be zero unless the time dependence is made to cancel. This occurs when $2\pi f_J = n\omega_s$. Accordingly:

$$\langle i \rangle = \frac{V_o}{R} + I_c \sum_{n=-\infty}^{n=\infty} (-1)^n J_n(\frac{2\pi V_s}{\Phi_0 \omega_s}) sin\varphi(0) \delta_{2\pi f_J, n\omega_s}. \tag{2.4.5}$$

where

$$\delta_{x,y} = \begin{cases} 1 & if\ x = y \\ 0 & otherwise. \end{cases} \tag{2.4.6}$$

From this equation, we conclude that the current-voltage characteristics are the sum of a straight line due to the resistive channel, and current spikes due to the JJ. This is illustrated in Fig. 2.5. At each current spike the voltage is given by

$$V_0 = n(\frac{\Phi_0}{2\pi})\omega_s. \tag{2.4.7}$$

The current can be anywhere along the spike depending on the value of $\varphi(0)$.
Actual measurements do not reveal these spikes in the I-V characteristics. This is because of the low junction resistances that allow the excitation sources to act more like current sources.

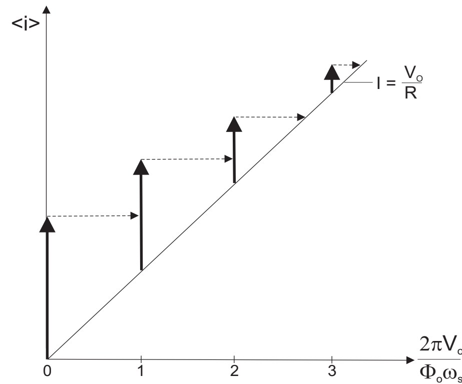

Figure 2.5: Theoretical IV characteristics according to the Voltage Source Model

2.4.2 Current Source Model

By substituting the voltage sources for current sources (see Fig. 2.6), reasonable agreement can be found with experimental data.

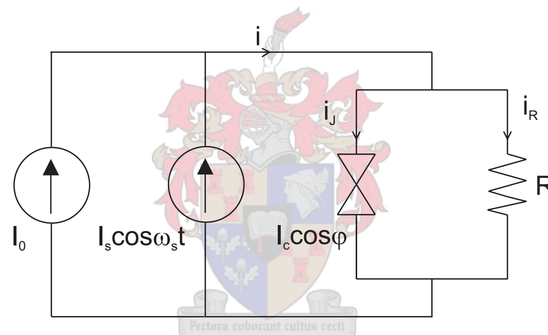

Figure 2.6: The Current Source Model

The total current is now given by

$$i(t) = I_o + I_s sin\omega_s t. \tag{2.4.8}$$

If it is attempted to solve this model mathematically, non-linear differential equations will result. Instead, we can qualitatively consider the model as an adaptation of the voltage source model and simply alter the I-V characteristics exhibited in Fig. 2.5 to incorporate current excitation. In this case we expect the average dc voltage to remain zero as the dc component of the driving current, I_o, is increased from zero. As I_o exceeds the height of the current spike at zero voltage, the voltage increases with a slope of the junction resistance until the voltage reaches the next current spike. As the current increases up this current

spike, the voltage will remain relatively fixed. This I-V relation will continue as current is increased, tracing out a staircase pattern. This phenomenon is known as Shapiro steps (see Fig. 2.7).

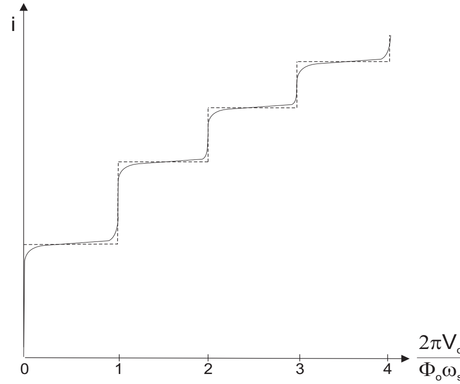

Figure 2.7: Illustration of experimentally observable Shapiro steps

The height measurement of these Shapiro steps are a very sensitive test for the Josephson effect [7].

2.5 Magnetic Behaviour of Josephson Junctions

A defining property of superconductors is their ability to screen magnetic fields. An applied field can, however, penetrate a superconductor a short distance known as the London penetration depth, λ. The size of λ is material-dependent, but is in the order of 140 nm for YBCO[1] [7]. When a Josephson junction is patterned in a superconductor, there exist a similar phenomenon. In this case, the Josephson currents will screen the magnetic fields from the interior of the junction. The magnetic field can penetrate the junction a distance λ_J known as the Josephson penetration depth, formulated as

$$\lambda_J = \sqrt{\frac{\Phi_o}{2\pi\mu_o J_c(2\lambda + d)}} \tag{2.5.1}$$

where d is the thickness of the insulating barrier, J_c is the critical current density and Φ_o is the magnetic flux quantum. From this equation it is clear that λ_J can vary with orders of magnitude depending on the current-carrying ability of the junction. To get an estimate of the typical values for λ_J in YBCO junctions, let $J_c = 10^6\ A/cm^2$ and $d = 100\ nm$,

[1]This value represents the penetration depth in the ab-plane of YBCO, $\lambda_{ab}(T \rightarrow 0)$

resulting in $\lambda_J \approx 25\ \mu m$. λ_J is a critical parameter when studying Josephson junctions since it determines the "magnetic size" of the junction. For a junction where the width, w, of the junction is larger than $4\lambda_J$ (a long junction), the junction self-field and screening currents cannot be ignored when studying the effects of an externally applied magnetic field. In the case where the junction width is smaller than $4\lambda_J$ (short junction), an applied field will penetrate the junction uniformly and the flux dynamics can be neglected.

The application of an external field has severe implications for the critical current of a Josephson junction. The applied flux introduces flux vortices (also known as Josephson vortices) in the junction. These vortices causes the critical current to fluctuate as a function of the external flux Φ according to

$$I_c(\Phi) = I_c \left| \frac{sin \frac{\pi\Phi}{\Phi_o}}{\frac{\pi\Phi}{\Phi_o}} \right|. \tag{2.5.2}$$

This Fraunhofer pattern (see Fig. 2.8) of the modulation of the maximum current is a common phenomenon in high-temperature JJs due to the relatively large junction areas in this technology. Another inherent problem is the noise that is induced by the Josephson vortices which limits the operation of HTS circuits in the presence of magnetic fields [7].

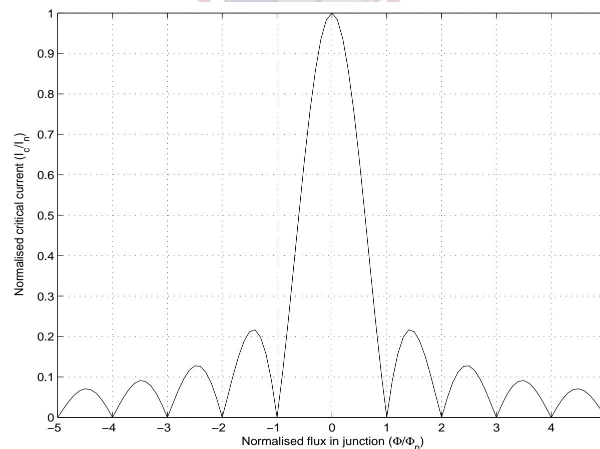

Figure 2.8: I_c as a function of the flux, Φ, in the junction

2.6 High-Temperature Superconductor Josephson Junctions

Although most initial studies of the Josephson effects are related to tunnel junctions, it was soon realised that the general concept of overlapping wavefunctions can be extended to other junction geometries. Amongst these, microbridges, point contacts and SNS junctions proved quite successful.
Tunnel junctions have, however, prevailed as the geometry of choice in low-T_c applications due to the possibility to create robust and reproducible devices with acceptable parameter spreads. A typical example of such technology is Nb-AlO_2-Nb SIS junctions. These junctions, however, possess high intrinsic capacitance necessitating an externally shunt resistor to give non-hysteretic current-voltage characteristics.

Following the discovery of high-T_c superconductors, it soon became clear that the inherent difficulties associated with HTS materials would make it very hard to reproduce a trilayer device such as a tunnel junction. Accordingly, interest in alternative junction geometries was reignited. Typical difficulties prevalent in HTS are:

- HTS have very short coherence lengths and is highly anisotropic
- Fundamental physics are significantly different from LTS
- Epitaxial growth is essential which leads to challenging film deposition conditions
- HTS are sensitive to structural and chemical changes

Luckily, grain boundaries in oxide superconductors act as natural Josephson weak links. This is in strong contrast to conventional low-T_c superconductors where grain boundaries typically enhance the critical current by acting as flux pinning centres. For this reason, grain-boundary junctions formed the basis for explorations in HTS electronics.

2.7 Grain Boundary Junctions

By definition, grain boundaries are structural defects which interrupt the lattice structure of the adjacent crystals and thereby affect most of the properties of the correlated electron system.

Grain boundaries are categorised according to the displacement and the rotation of adjoining crystals. Rotational grain boundaries are characterised by crystal misorientations which are tilted and/or twisted [8]. A tilt refers to a rotation of the crystal grains around an axis in the plane of the grain boundary and a twist to a rotation around an axis perpendicular to the grain boundary plane. Typical grain boundaries that are encountered in HTS are illustrated in Fig. 2.9.

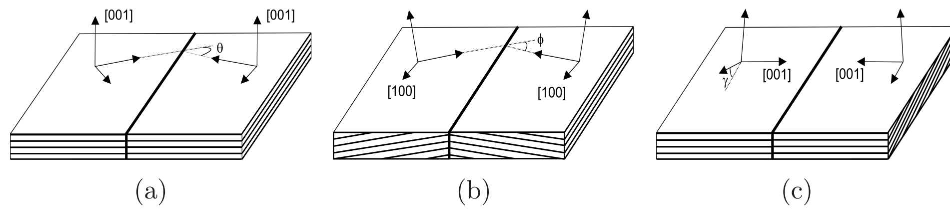

Figure 2.9: Schematic illustration of (a) a [001]-tilt boundary, (b) a [100]-tilt boundary and (c) a [100] twist grain boundary

The grain boundary plane is generally described as a region of structural disorder shown to be insulative with a resistivity of 10^{-9}-10^{-7} Ω-cm. The degree of disorder is determined by the angle of misfit between the two adjoining crystal axes (see Fig. 2.10). The idea is thus to introduce disorder in a controlled manner by regulating the angle between the abutting crystals. For small angle grain boundaries (typically less than 10° misfit), the current carrying ability of the HTS film would be limited without displaying any Josephson-like behaviour. As soon as angles increase beyond a certain threshold, excellent Josephson junctions can be created.

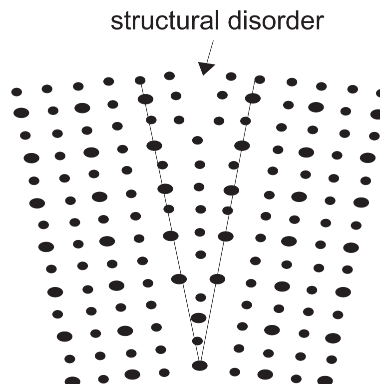

Figure 2.10: A grain boundary illustrating a region of disorder where the two lattices mismatch

Several models have been suggested to account for the properties of HTS grain boundaries. One popular model is to describe low-angle grain boundaries to be made up of an array of alternating superconductive and non-superconductive regions. These regions are introduced by periodic dislocations to accommodate for the lattice mismatch during thin film growth. These dislocations merge into a continuous interface as the angle of misfit increases [9].

It should be noted that the natural occurrence of grain boundaries in HTS polycrystalline thin films comes at a cost. Despite acting as flux pinning centers (increasing magnetic tolerance levels), these grain boundaries can severely limit the current carrying abilities of the thin films (a serious problem when optimal power transmission is needed).

Although grain boundaries are not understood completely, various technologies have been developed to make them useful for application purposes. At present, grain boundary junctions are the most studied HTS JJs providing attractive electrical properties such as $I_c R_n$ products of up to 400 μV at 77 K [10]. The basic idea of artificially creating grain boundaries acting as weak links has led to the founding of a number of popular junction topologies (see Fig. 2.11).

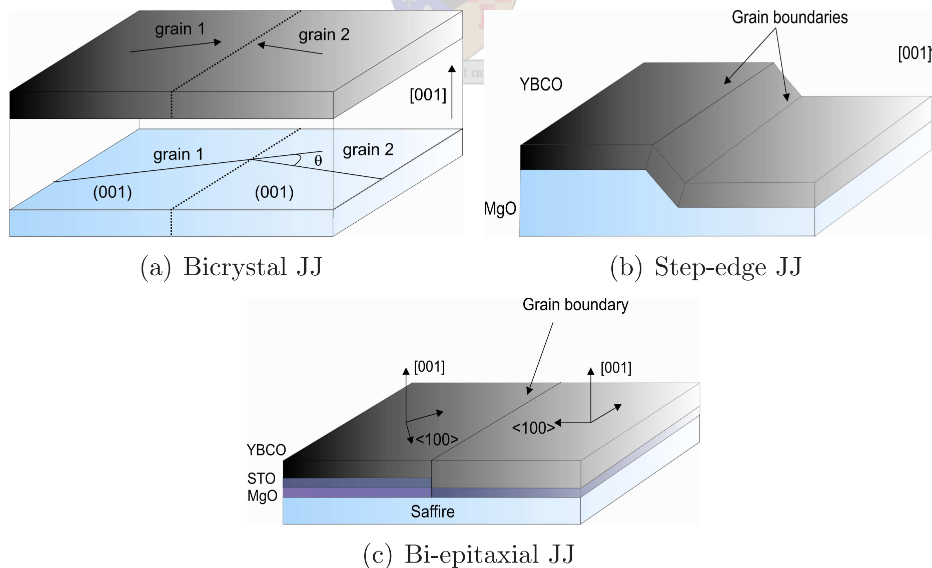

(a) Bicrystal JJ

(b) Step-edge JJ

(c) Bi-epitaxial JJ

Figure 2.11: Three popular types of grain boundary junctions

2.7.1 Bicrystal Junctions

The development of a high-T_c Josephson junction technology was pioneered by the work on bicrystal grain boundary junctions (GBJs) at IBM [2]. In this technique, a grain boundary is introduced in the substrate material by fusing two crystals at some arbitrary angle. This grain boundary is replicated in a thin film which is grown epitaxially on top of the substrate. Bicrystal technology results in well-defined grain boundaries. It has the added advantage that the grain boundary angle can be controlled, enabling a systematic study of transport properties across high-T_c grain boundaries. The inherent limitation is that the position of the junctions is bound to the position of the bi-crystalline in the substrate. For these reasons Bicrystal GBJs is ideal for research purposes or in devices requiring only a few junctions (featured in many commercial SQUID products).

Bicrystal junctions represent HTS technology in its infancy [11] and provides no extendibility as required in complex electronic devices.

2.7.2 Step-edge Junctions

The idea to introduce grain boundaries at steep substrate steps was first proposed by Daly et al [12]. In this junction geometry, a step-edge are patterned into a substrate during an etching process before the thin film is epitaxially deposited over the step. The angle of the step-edge as well as the choice of substrate determine the misorientation of the crystal grains. The reason for this being that on non-perovskite substrates such as MgO, HTS thin films will grow with the [001] axis parallel to to the substrate normal. This growth mechanism gives rise to [100]-tilt grain boundaries. On the other hand, perovskite-like substrates such as STO favour the formation of 90° grain boundaries [13]. In contrast to bicrystals, this technology offer topological freedom necessary for the design and the integration on small and large scale. An example of such design freedom was demonstrated by Reuter et al by fabricating up to 600 step-edge junctions on one chip [14].

2.7.3 Bi-epitaxial Junctions

In 1991 Char et al developed a technique that allows for the fabrication of asymmetric 45° bi-epitaxial GBJs [15]. The fabrication process depends on structured template layers controlling the in-plane orientation of HTS film. Firstly, an epitaxial seed layer such as CeO_2 (on STO) or MgO (on Saffire) is deposition to provide a 45° in-plane rotation with

the respect to the a-b axes of the substrate. The seed layer is then patterned, followed by an in-situ deposition of a buffer layer and HTS film. The HTS film orientation corresponds to the template structure of the underlying layers, giving rise to rotational grain-boundaries. As in the case of step-edge junctions, bi-epitaxial junctions provide topological freedom of design.

2.8 Extrinsic Barrier Junctions

In order to develop HTS microelectronics, a complete epitaxial multilayer circuit technology is required. Extrinsic Barrier Junctions meet this requirement and is seen as the most promising HTS junction technology to date. This class of junctions is based on the deposition of a thin interlayer between two superconducting electrodes. The extrinsic interfaces that result from this geometry does, however, introduce several fabrication challenges in order to control junction properties.

2.8.1 Ramp Junctions

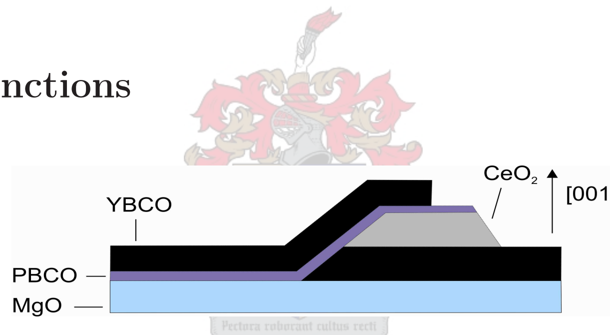

Figure 2.12: A Ramp-edge junction

Ramp junctions with YBCO electrodes were pioneered by Gao et al [10]. This junction geometry is characterised by an unique epitaxial trilayer structure (see Fig. 2.12). Fabrication starts by creating an initial ramp structure by etching a shallow step-edge into an epitaxially deposited YBCO/insulator bi-layer. The ramp is then covered with the barrier material, (typically doped YBCO or PBCO) before the top electrode is deposited in-situ. This geometry allows current transport in the a-b plane of the c-axis grown electrodes, taking advantage of the longer coherence length along these planes. Since the properties of these junctions depend on the quality and thickness of the barrier layer, a smooth ramp-edge of excellent crystalline quality is critical. Ramp junctions allow for flexibility in device design and substrate choice, which makes it possible to fabricate more complicated circuitry.

2.9 General Properties of HTS Josephson Junctions

Despite their different geometries, HTS JJs demonstrate quite similar electrical behaviour. It is because of these similarities that many believe the underlying mechanisms behind junction operation is in fact the same. Some general properties include:

- The IV characteristics of these junctions can be modeled by the resistively and capacitively shunted junction (RCSJ) model.

- The temperature dependence of the critical current $I_c(T)$, is quasilinear over a wide temperature range:
$$I_c(T) = I_{c0}\left(1 - \frac{T}{T_c}\right). \tag{2.9.1}$$
This behaviour is in strong contrast to other low-T_c JJs and inconsistent with conventional proximity effect theory (exceptions does exist such as ramp junctions with Ca-doped YBCO barriers) [16].

- The junctions possess a large amount of low frequency $\frac{1}{f}$ voltage noise due to fluctuations in the critical current, I_c, and normal resistance, R_n.

- These junctions are generally overdamped, ($\beta_c < 1$), with non-hysteretic IV characteristics. Some junction types may, however, become slightly hysteretic at low temperatures.

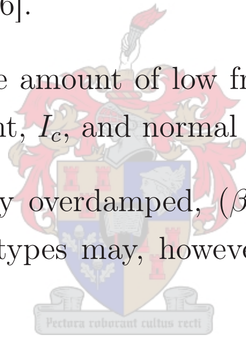
Pectora roborant cultus recti

- A defining feature of HTS junctions is their scaling behaviour $I_cR_n \propto (J_c)^p$ with $p \approx 0.5$. This is in strong contrast to classical tunnel junctions where I_cR_n is independent on J_c and equal to about Δ/e [10].

2.10 Chapter Overview

This chapter provided a basic framework for the analysis of Josephson junctions. The RSCJ model was introduced and used to obtain insight into the electrical operation of a generalised Josephson junction. Next, popular HTS JJ geometries (all being researched at Stellenbosch) were discussed and their general properties listed.

Chapter 3

Photolithography

The lithography process that existed prior to the commencement of this research was characterised by poor photoresist mask resolution. One of the main objectives of this thesis was the fabrication of good quality step-edge Josephson junctions. Such a process requires resist sidewall angles as close to 90° as possible. The optimal process before 2005, however, only produced resist sidewall angles less than 30° which were clearly inadequate to realise a step-edge fabrication process. At the University of Stellenbosch, contact lithography is the only available method to expose photoresist. Typical angles obtainable using this method of exposure are between 45° and 75° [17].

This chapter briefly introduces the photolithography process before elaborating on the optimisation route followed to obtain resist angles as close to 75° as possible.

3.1 Process Description

To understand how to best optimise the lithography process, the influence of all the process parameters should be clear. For this reason, a short description of each stage in the process is given. Six main stages are identified:

1. Sample Preparation
2. Photoresist Spinning
3. Soft Baking
4. Exposure

5. Development

6. Hard baking

3.1.1 Sample Preparation

The importance of sample preparation for lithography should not be underestimated. By inspecting a "clean" sample under an optical microscope the presence of micron-sized particles is frequently observed. To remove these particles from the sample surface, samples were immersed in an ultrasonically excited acetone bath for 5 minutes. The sample was blown dry with N_2 (if available) or else mechanically polished. The sample was then inspected under microscope to ensure the removal of all particles (and the absence of any solvent stains). Resist adhesion problems are mainly associated with water molecules that reside on the surface of the sample. Accordingly, a dehydration bake is performed for 10 minutes at 150° on a hot plate to evaporate any excess water.

3.1.2 Photoresist Spinning

Spinning of the photoresist to produce a uniformly coated substrate is an essential step in the photolithography process. The spin-speed profile should be optimised to give a resist coating of correct thickness and good substrate coverage. Before spinning, the sample should be aligned to the center of the vacuum chuck to ensure vibration free spinning. A particle stuck on a sample surface will be revealed after resist spinning by radial oriented coloured traces. Sample preparation (as mentioned above) will eliminate this problem unless a particle is introduced from the photoresist bottle itself.

After spinning, it will be clear that the sample edges are characterised by thickened regions of resist, called edge beads. These excess resist can be removed by using a seperate exposure procedure or by carefully removing these edges with a scalpel. By removing these excess resist, better contact will be possible during exposure of the resist.

3.1.3 Soft Baking

To prepare the photoresist for UV exposure, a pre-exposure bake, or soft bake, is performed to drive the solvent from the resist and to remove build-in stresses. This is a critical step in that failure to sufficiently remove the solvent will affect the ability to resolve smaller mask

Pectora roborant cultus recti

features. On the other hand, excessive baking can destroy the photoactive compound of the resist and reduces its sensitivity. Exposure time is closely related to soft bake time and therefore, consistency is important once exposure time has been characterised for a particular baking time.

3.1.4 Exposure

As mentioned, a contact exposure procedure was used to expose the sample with ultra-violet light. As the exposure of a resist volume is chemical in nature, reactions during the exposure event are very temperature dependent. For this reason it is necessary to wait a few minutes after performing a prebake to allow the resist to cool down to room temperature. Another problem that might arise is the occurence of standing waves due to UV light getting reflected from the sample surface to re-enter the resist. These reflections cause interferences inside the resist generating standing wave patterns in the vertical direction of the resist volume.
A post-exposure bake, or PEB, can be used to reduce standing waves in positive resist. When this procedure was attempted, however, it was found to deteriorate the sidewall angle of the resist.

3.1.5 Development

After UV exposure, the exposed regions of the resist are weakened by rupture or scission of the main polymer chains resulting in increased solubility in development solutions [17]. It was observed that a suitable time period should elapse to allow for these photochemical reactions to complete. In this thesis, immersion development with mild agitation was used. After immersion, the sample was rinsed in deionised water before spin-dryed. It should be noted that the temperature of the developer will influence development times and the container should always be stored in a temperature controlled environment.

3.1.6 Hard Baking

A post development bake, or hard bake, is sometimes used to improve a resist's wet and dry etch resistance by hardening it and improving its adhesion properties (weakened during development). Although this makes the resist more difficult to remove after etching, it can improve the selectivity of the etch process. Typically, a hard bake should be performed below 130°C to prevent the resist from reflowing and compromising edge resolution.

3.2 Process Optimisation

Several improvements were made to the photolithography process:

1. The exposure unit was serviced (of special note is the cleaning of the UV reflective mirror).

2. The base of the exposure unit was coated with a photo-absorbent material. This significant improved the resist resolution obtained with MgO substrates limiting light reflections and the occurrence of standing waves.

3. Shadowing of the resist profiles occurred frequently. This problem was addressed by removing excess resist (edge beads) from the corner regions to make a gap free contact possible.

4. The gap between mask and resist was accordingly minimised to ensure sufficient contact pressure to avoid diffraction.

5. New resist and developer were purchased and process times optimised.

The resist used in this research was SPR 700 and an MF 24A developer. This resist was used for its better dry etching properties and its ability to withstand higher temperatures without compromising resolution. An optimised parameter set for MgO, YBCO and PBCO were accordingly attained and are given in Table 3.1.

Pectora roborant cultus recti

Resist spinning	4500 rpm for 50 s
Soft bake	90 s at 115°C
Post-bake wait	5 min
UV exposure	MgO: 21 s, YBCO/PBCO: 25 s
Post-exposure wait	10 min
Development	MgO: 54 s, YBCO/PBCO: 25 s
DI-immersion	30 s rinse
Hard bake	5 min at 95°C

Table 3.1: Optimal parameter set for MgO, YBCO and PBCO materials

Some of the typical process problems encountered during optimisation are illustrated in Figs. 3.1-3.4.

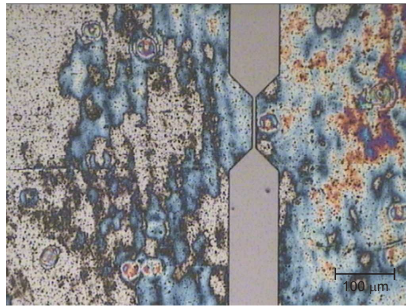

Figure 3.1: An example of an under-exposed mask pattern on YBCO

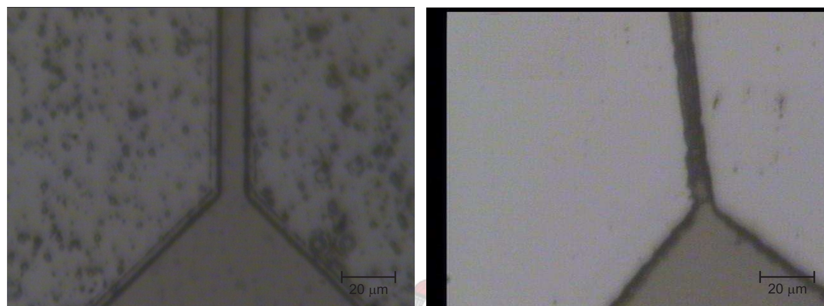

Figure 3.2: The effect of under-development (left) and over-development (right)

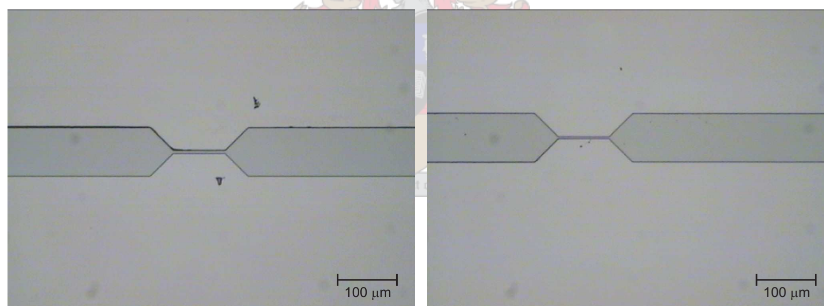

Figure 3.3: Shadowing of the resist profiles caused by excess resist (left) and after edge bead removal with gap free contact (right)

Figure 3.4: Ineffective resist removal after exposure to excessive heat

3.2.1 Results

After the lithography process was optimised, a significant improvement in mask pattern transfer could be observed. Fig. 3.5 shows an AFM image of a resist sidewall profile. The resist angle shows a sharp edge without any indication of resist reflowing indicating good bake times. This angle was measure to be 71°, which is a 40° increase compared to the old process. No residual (under-exposed) resist was visible. The resist thickness was measured as 1.96 μm which is well-suited for the dry-etching process to follow (to be discussed in the next chapter).

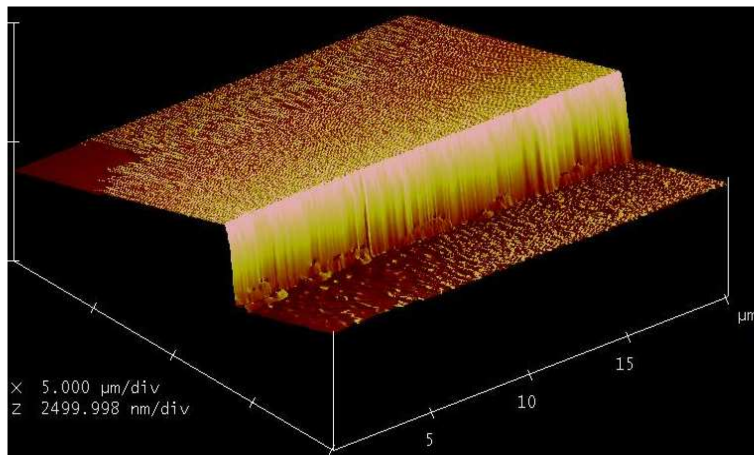

Figure 3.5: Optimal resist sidewall profile

Pectora roborant cultus recti

3.3 Chapter Overview

This chapter highlighted some of the important concepts in the photolithography process. The in-house process was optimised to yield a significant improvement in resolution as compared to the old process. Resist sidewall angles of 70° were realised which lay the foundation for step-edge junction fabrication.

Chapter 4

Argon Ion Milling

Etching can be described as the process of transferring a mask-defined pattern onto a substrate by chemical or physical removal of material [17]. Dry etching (as opposed to wet etching) has become the preferred method of etching mainly due to the promise of good process control and high resolution pattern transfer characteristics. One type of dry etching is so-called ion-beam milling, also known as ion-beam sputtering, where atoms are physically removed from a target surface by bombardment with energetic inert ions.

The fabrication of superconducting circuits demand such a reliable, high resolution etching technique. Distortion to critical dimensions and edge profiles will play a crucial role in determining characteristic circuit parameters such as J_c and R_n. Accordingly, this chapter aims at successfully optimising the design and operation of an in-house argon ion milling process.

4.1 The Argon Mill System

In 2002, P.A. Rottier introduced an Argon mill system at the University of Stellenbosch [18]. The operation of the mill was, however, never completely optimised. This severely limited the application value of the system and encouraged students to resort to wet etching as a means to transfer circuit patterns. In 2004, L. Snetler attempted to optimise the system for step-edge fabrication, but could only succeed in identifying operation problems inherent to the system [1].

The operation of the mill can be divided into three categories: Plasma generation, plasma extraction and finally substrate bombardment.

4.1.1 Plasma Generation

The discharge chamber of the argon mill was designed as a rf multicusp ion source. An rf antenna, fed by a 400 W rf source operating at a frequency of 13.56 MHz, initiates and sustains ionisation of the milling gas, argon. To ensure maximum rf power transfer, an impedance matching network is used to match the nominal 50 Ω output impedance of the rf source to the plasma-antenna load. Dynamic matching is necessary due to the impedance change resulting after plasma ignition. The matching network consists of two adjustable capacitors: a series capacitor to achieve initial matching and a parallel capacitor used for fine tuning (see Fig. 4.1).

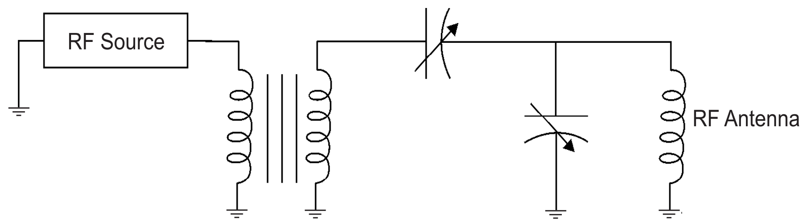

Figure 4.1: Matching Network of the Argon Mill

Pectora roborant cultus recti

Plasma confinement is accomplished by sixteen Samarian-Cobalt (Sm-Co_5) magnets housed inside the walls of the stainless steel discharge chamber. Additional magnets are positioned above the antenna flange to form a longitudinal line cusp configuration (see Fig. 4.11). The resulting magnetic flux confines the plasma to the center of the discharge chamber. This design aids in increasing plasma density and reduces the necessary operating pressure. The nearly field-free region in the center of the chamber determines the maximum extraction area, where the plasma density is most homogeneous. The presence of plasma and rf power necessitates water cooling of the discharge chamber and the rf antenna. Cooling had to be done with deionised water to prevent the flow of a leakage current between the discharge chamber and ground.

This component of the design is very stable and plasma generation could be obtained without any problem.

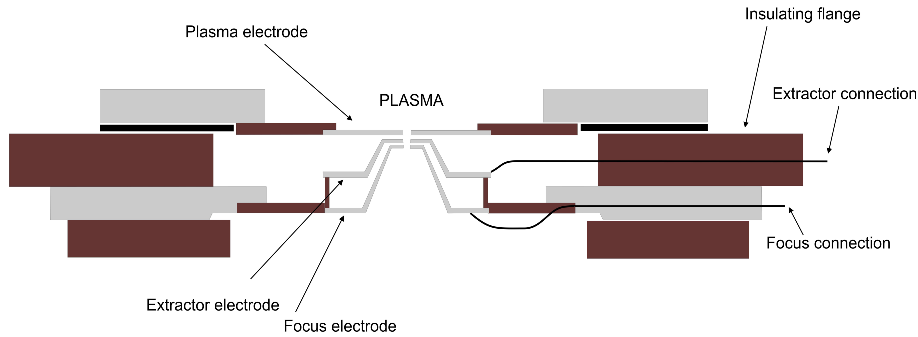

Figure 4.2: Old Extraction System used for Argon Ion Milling

4.1.2 Plasma Extraction

After plasma ignition, the ionised argon needs to be accelerated from the discharge chamber to the bottom chamber containing the sample to be etched. Separating the two chambers is the extraction system. The extraction system of the mill is critical in providing a desired ion beam profile for etching. It controls the plasma sheath characteristics[1], the beam current and beam divergence. A brief description of the initial extraction system (pre-2005) as illustrated in Fig. 4.2 follows:
The system consisted of a plasma electrode, an extractor electrode and a focus electrode. Plasma was extracted through a 2 mm hole in the center of the plasma electrode which was left floating. This was done to realise higher extraction voltages without spark-over between the electrodes. The extractor electrode was connected to a negative voltage to accelerate ions from the plasma toward the bottom chamber. The negative voltage inevitably causes the ion beam to diverge and necessitates refocusing. Inefficient focusing can cause ions to bombard (and erode) the focus electrode. A positive voltage applied to the focus electrode could converge the beam to avoid excessive divergence. (This design was obtained from C. Boonyawan at the Chiang Mai University, Thailand [20]).

4.1.3 Substrate Bombardment

After passing through the extraction system, the ions impinge on the surface to be milled. The sample is mounted on a water-cooled, copper sample holder. This holder allows for three degrees of freedom to orientate and position the sample: sample tilting, sample rotation (with reference to the incident beam normal) and changing the height of the sample. During a milling process, the entire sample holder can be rotated by a stepper motor in-

[1]For a detailed description of plasma sheaths, see [19]

Pectora roborant cultus recti

stalled in the chamber. The extracted ion current can be monitored with a measuring plate connected through a resistor to earth. Alternatively, a Faraday cup can be installed but not while the sample holder is in place. The bottom chamber and the sample holder are grounded.

4.2 Initial Optimisation

The optimisation as done by L. Snetler in 2005, yielded a beam profile that was extremely focused [1]. The spot size of the region of concentrated ion density was reconfirmed to be 0.25 cm^2. If compared to the size of a typical substrate, 1 cm^2, it is clear that an inhomogeneous etch profile will result. This insufficient beam divergence was observed even if no focusing potential was applied to the extraction system. Accordingly, the effect of substrate height on beam divergence was investigated. As the bottom chamber is grounded, and the ion beam is positively charged, beam divergence is expected after the ions is ejected from the extraction system. After varying the substrate height, minimal difference in spot size could, however, be detected (see Fig. 4.3). These tests also revealed that extended mill times was not a viable option to expand the etched areas as resist would start to burn. Despite the small spot sizes, reasonable ion current (in excess of 0.8 mA/cm^2) was measured.

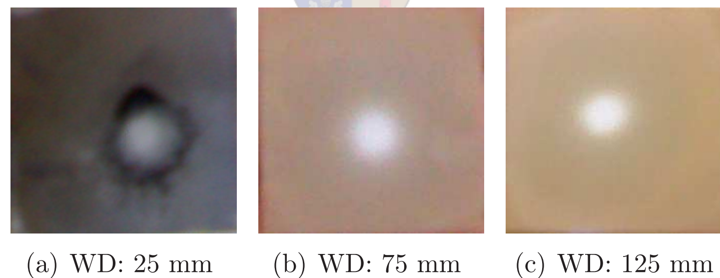

(a) WD: 25 mm (b) WD: 75 mm (c) WD: 125 mm

Figure 4.3: Resist on 2 x 2 cm^2 Alumina substrates milled for 45 minutes at various working distances (WDs) below the extraction plates

It was thought that the accelerated ions possessed too much kinetic energy to divert from their trajectories as determined by the electric fields induced by the extraction plates. Accordingly, it was decided to decrease the extraction potentials. This resulted in a significant (almost exponential) decrease in beam current reaching the substrate. Accordingly, the possibility of operating at a reduced extraction voltage was rendered not practical. The

suspicion that the extraction aperture from the discharge chamber was in fact designed to yield focused ion beam (FIB) behaviour, seemed very probable. The effect of the aperture geometry on the beam profile was thus investigated:

Initially, the aperture size was increased to 2 cm in diameter after which apertures was fitted into this “aperture slot”. Without any aperture inserted, it was difficult to extract sufficient plasma. After trying varies shapes of apertures, it was seen that, from a geometrical perspective, it is desirable to shield the center of the beam sufficiently to suppress the focusing effect. Although this approach yielded reasonably uniform spot sizes larger than 1 cm^2, the ion current extracted was insufficient to render practical etch rates. Fig. 4.4 shows four different apertures used, where the aperture on the right produced the best beam profile.

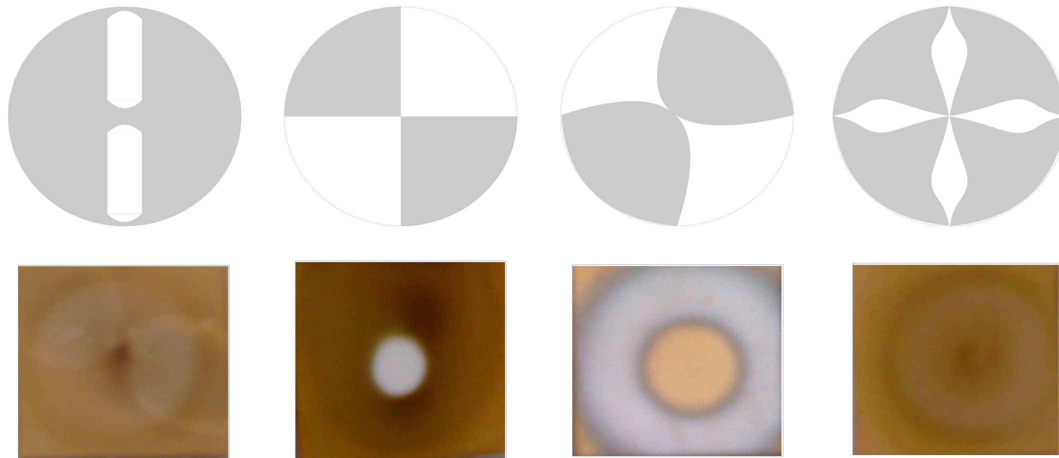

Figure 4.4: An illustration of apertures used with their corresponding etch profile below. These etch runs were done on 2 x 2 cm^2 Alumina substrates covered with resist or gold

It was decided that a more drastic approach needed to be taken.

4.3 Gridded Accelerator System

To obtain an improved ion beam profile, a different extraction system was required. Ion beam extraction can be realised by using either gridless or gridded extraction systems. Inspired by the gridded Kaufman ion source design [21], it was decided to introduce a gridded ion source to the system. The basic extraction system design consists of a two-grid geometry: a positive screen grid placed adjacent to the discharge plasma followed by a

negative accelerator grid positioned further downstream. Optical alignment of the grids is necessary to ensure ion extraction with minimal grid-bombardment. The grids are biased at relatively high potentials necessitating sufficient grid separation to avoid flash-over.
The screen grid is biased at a positive potential equal to that of the discharge chamber (anode), "screening" the discharge plasma from the accelerating electric fields. After plasma ignition, stable plasma sheaths are formed around each screen hole. These sheaths are space-charge limited emissive surfaces of positive ions from the discharge plasma. Ions will reach a sheath with Bohm velocity [19] before being accelerated by the strong electric field between the positive sheath and negative accelerator grid hole. Ions tend to follow the electric field lines introduced by the grid configuration especially near the plasma sheath where the ion velocity is still reasonably low [21]. The amount of beam focusing/divergence is strongly affected by the respective grid hole diameters and the grid separation distance determining the profile of the E-field lines and thus the ion-pathways. The diameter of screen grid holes are typically larger than those of the accelerator grid, causing the electric fields to focus the argon ions into narrow beamlets. A typical operating scenario is shown in Fig. 4.5.

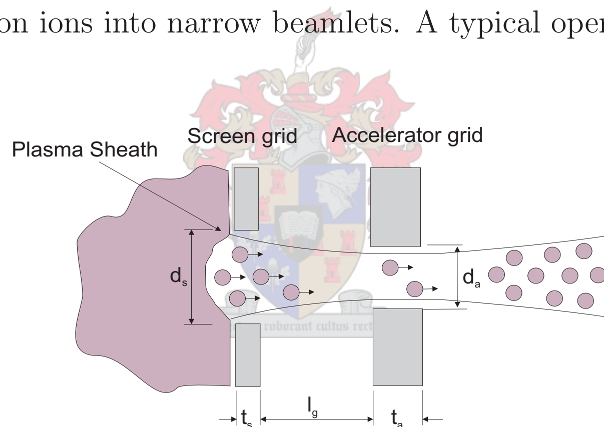

Figure 4.5: Illustration of beam extraction under typical operating conditions

Another critical factor is the position and shape of the plasma sheath as this contributes to the local E-field distribution. As the plasma density is increased (either by increased pressure (higher ionisation probability) or higher rf input power) the plasma sheath moves further into the screen hole to satisfy the space charge limited ion-emission condition (see Fig 4.6) [21]. The desired concave shape of the sheath now becomes flat leading to ions impinging on (and consequently eroding) the acceleration grid. The degradation in ion focusing corresponds to a decrease in the ion current extracted to the bottom chamber. Sufficient focusing is thus critical to ensure higher etch rates as well as to extend the operation lifespan of the extraction system.

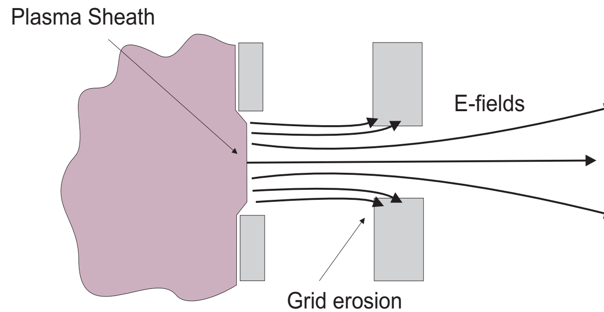

Figure 4.6: Electric field distribution for increased plasma density

After the ion beam (Ar^+-ions) leaves the acceleration grid, the beam is predominantly positively charged. If such a beam should impinge on an insulative surface (typically an oxide substrate), charging effects could result in unwanted etch profiles. Accordingly it is necessary to neutralise the ion beam by adding thermal electrons from a hot filament, hollow cathode or plasma bridge [22]. These neutralisation electrons will rapidly spread through the ion beam. The electrons are "isolated" from the extraction grids systems by the electrostatic forces produced by the negative potential of the accelerator grid. Accordingly, an equipotential surface (approximately ground potential) is created further downstream from the grids. Between the acceleration grid and this ground potential, the ions are decelerated owing to the retarding electric fields. This deceleration region can defocus the ion trajectories significantly. One possibility to minimise this downstream beam divergence is to decrease the acceleration voltage. This, however, introduces the problem of neutralisation electrons backstreaming to the discharge chamber.

Pectora roborant cultus recti

Accordingly, a third decelerator grid was introduced to the system to reduce this downstream ion beam divergence. This grid is kept at ground potential and positioned downstream of the accelerator grid. This grid now serves as the neutralisation plane resulting in flatter equipotential surfaces below the accelerator grid holes. Ions emerging from the acceleration grid now experience less off-axis deflection (divergence) [23]. Fig. 4.7 illustrates the additional grid and the potential profile through the extraction system [24]. Once the ions passes the neutralisation plane, their trajectories will remain mostly unchanged.

4.3.1 Grid Design

The physical dimensions of the grid-holes and grid-spacing were based on values identified in literature to yield optimal beam characteristics [23]. The optimal parameters were:

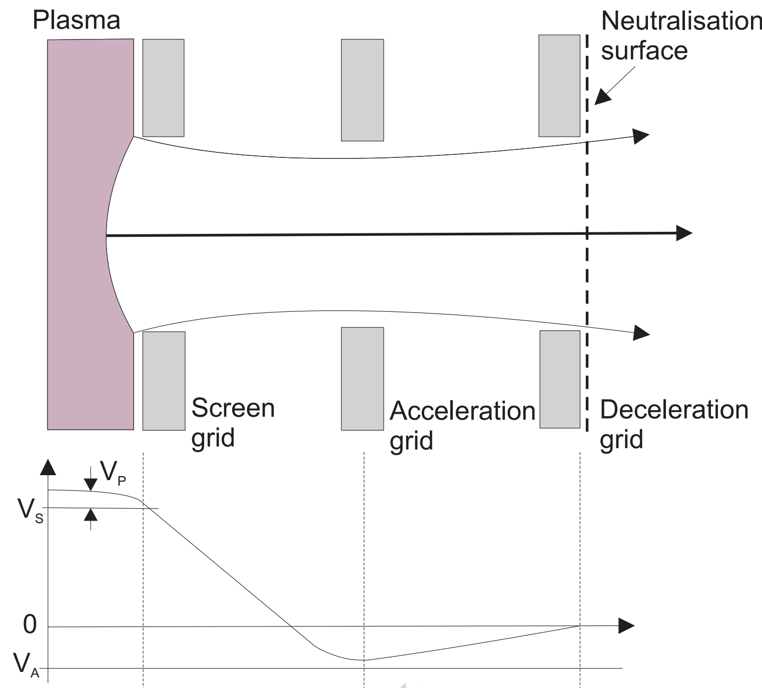

Figure 4.7: Potential distribution through grids (V_P denotes the plasma potential)

screen hole diameter $d_s = 2.06$ mm, screen grid thickness ration $t_s/d_s = 0.985$, accelerator grid thickness ration $t_a/d_s = 0.37$, decelerator grid thickness ratio $t_d/d_s = 0.37$, accelerator hole diameter ratio $d_a/d_s = 0.64$, decelerator hole diameter ratio $d_d/d_s = 0.83$. Due to drilling-dimension limitations, restrictions existed on obtainable grid-hole dimensions and the suggested values could only be approximated. In future, laser patterning of the grids should be considered as an alternative. The grids were all made from stainless steel and holes were accordingly drilled in a hexagonal array with 0.25 mm center-to-center hole spacing. The approximate area of the grid-hole-array was 4 cm^2 to ensure a broad ion beam. Grid separation was accomplished by inserting insulative mica washers between the grids while maintaining grid-hole-alignment.

4.3.2 Testing of Extraction System

After the extraction system was built, the operating conditions needed to be determined. The first consideration was the milling pressure to be used. Pressure will not only determine the mean free path of the ions (and thus their directionality), but also the conductivity of the vacuum. In conjunction with the rf power, these parameters determine the ionisation rate of the plasma. The increased ion density resulting from increased pressure will

contribute toward providing an upper limit on the acceleration and screen grid potentials before flashover occurs. From literature, the typical pressure range for ion-beam milling falls between 10^{-4} and 10^{-3} mbar [25]. As initial testing excluded any neutralisation which would increase pressure, the working pressure was chosen to be $2x10^{-4}$ mbar. At this pressure[2], the screen grid could be operated at 1.5 kV (for 0 V acceleration) and the accelerator grid reached 2.6 kV (for 0 V screening) before arching was observed. These values were, however, significantly decreased if both grids were biased simultaneously and finding a "dynamic balance" proved quite difficult. Finally, the maximum stable operating voltages were identified as $V_S = 800$ V and $V_A = -250$ V.

These values correspond quite well with quoted values from literature where extraction potentials of $V_S = 500$ V and $V_A = -200$ V are standard. Having fixed the pressure and operating range of the extraction potentials, attention could be given to attain a sufficient ion current with a reasonable spot size. From initial testing it was clear that the spot size is almost equal to the grid diameter of the extraction system. This was established by milling resist or gold plated Alumina substrates (see Fig. 4.8). The spot size were extremely homogeneous and approximately 4 cm^2 in size. As a consequence, up to four substrates could be milled evenly with the new extraction system.

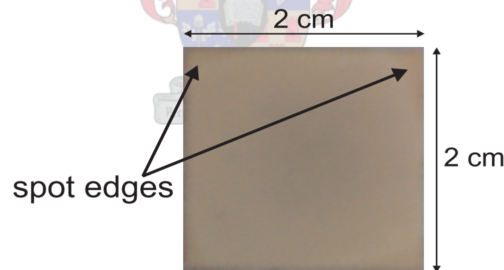

Figure 4.8: Milled resist on an Alumina substrate illustrating the spot size obtained with the 3-gridded extraction system

It was further noticed that the spot size was not significantly affected by variation to grid potentials within the ranges mentioned above, implying limited downstream divergence and adequate ion mobility. This also allowed for the substrate height to be placed suitably below the extraction system to limit excess heating, which can cause the resist to burn. Finally the substrate height was fixed 60 mm below the decelerator grid. The only matter remaining was to determine the ion current that could be extracted as this will ultimately

[2]where not mentioned, rf power was kept at 100 W

control (along with ion energy) the etch rate of the milled material. Two parameters were seen as variable to achieve this aim: the rf power and the extraction potentials. By increasing the rf power, ionisation probability should increase and more ions should be extracted. This was confirmed by varying the rf power between 50 W and 150 W while keeping the grid potentials constant at $V_S = 500$ V and $V_A = -200$ V (see Table 4.1).

RF Power [W]	Ion Current [μA/cm^2]
50	130
75	210
100	270
125	330
150	360

Table 4.1: Ion current as a function of RF power

From these values it can be seen that reasonable ion current reaches the substrate (compared to values in excess of 1 mA/cm^2 reported in literature). As was mentioned, finding a dynamic balance for the grid potential above a certain threshold became very complicated. Although increased ion currents (up to 540 μA/cm^2) could be obtained by increasing the acceleration potential, the stability of the system became questionable.

Pectora roborant cultus recti

Accordingly it was decided to operate the system differently when higher etch rates were required. This was accomplished by inverting the acceleration and deceleration grid potentials. This alteration implied that larger potentials could be applied to the screen and acceleration grids (now separated by a grounded grid) respectively. Both grids could now be operated simultaneously with $V_S = 1.5$ kV and $V_A = 2.5$ kV. This ultimately provided a larger total extraction potential ($\approx V_S + V_A$) and better ion currents (up to 0.9 mA/cm^2 was measured for only 50 W rf power). This setup better approximates the operation of the two gridded extraction system discussed before without a neutralisation plane at the last grid controlling downstream beam divergence.
Accordingly two sets of optimal operating conditions were obtained depending on the etch rate requirement. The parameters are summarised in Table 4.2.

4.3.3 Neutralisation

As mentioned, it is necessary to neutralise the ion beam to prevent charging of electrically isolated substrates. Such charging lead to skewing of ion directionality and adverse etching

Parameter	Value (Slow ER operation)	Value (High ER operation)
P_{Ar}	2x10^{-4} mbar	2x10^{-4} mbar
RF Power	100 W	50 W
V_S	600 V	1 kV
V_A	150 V	2 kV
Working Distance	60 mm	60 mm
Ion current	285 μA/cm^2	0.8 mA/cm^2

Table 4.2: Optimal mill parameters for 2 modes of operation

effects [17], [26]. If the target is electrically conducting and grounded, the neutralization requirement is moderate. Electrons are only needed to compensate for the loss of the more energetic electrons that are absorbed by nearby conducting surfaces. Substrate neutralisation is, however, not the only reason why neutralisation is desired. Experimentally, the potential in an ion beam rises significantly when there is a deficiency of electrons [27]. As soon as this potential exceeds a certain threshold voltage relative to surrounding hardware, small arcs will start to occur. These arcs supply enough secondary electrons to keep the beam potential from rising further, but at the cost of erosion to the hardware components inside the chamber.

Pectora roborant cultus recti

To obtain a suitable flow of electrons, several techniques were attempted. Initially, a tungsten wire was arranged below the extraction grid system and heated with an ac supply. The amount of electron current was monitored by utilising the ion measuring plate installed in the bottom chamber (from which the percentage neutralisaton could be calculated). Current of 5-6 A was required to see any significant changes in the reading. Applying such a high filament current resulted in higher electron emission, but the trade-off is an exponentially decreasing lifetime due to thermal evaporation of the filament material. After the chamber was opened, tungsten contamination was clear. Other examples of filaments are Lanthanum Hexaboride (LaB_6), which provide around an order of magnitude higher brightness than tungsten filaments. These filaments thus have a longer lifespan but unfortunately they need to operate at higher vacuum (10^{-6} to 10^{-7} Torr) compared to that of tungsten (10^{-5} Torr) [28]. At these pressures, argon milling could not be realised.

Accordingly, to reduce the contamination factor, it was decided to house the filament inside a cylinder with a small orifice and accelerate the electrons toward the ion beam. The filament (tungsten wire) was bent into an "inverted V" shape, centered close to the

orifice. Electrons will be preferentially emitted from the bent tip and produce a coherent source of electrons in this area. The cylinder (also called a Wehnelt cap) was accordingly biased at a negative potential (-1 kV) to serve as a convergent electrostatic lens, focusing the cloud of electrons. By introducing an anode (at ground potential) positioned in front of the orifice, the electrons will be accelerated toward the ion beam. Such a configuration closely resembles the electron guns used in Scanning Electron Microscopes (SEMs) as shown in Fig. 4.9.

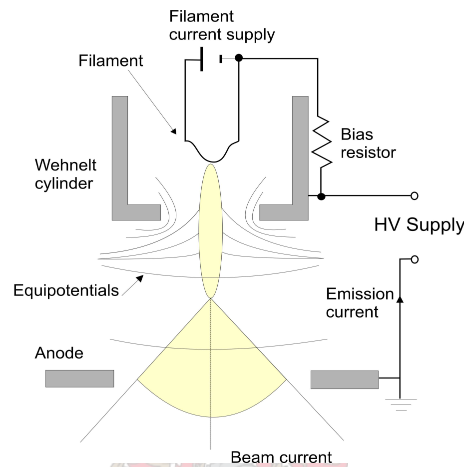

Figure 4.9: Illustration of an electron source

Pectora roborant cultus recti

This electron source provided improved neutralisation results . Again quite high filament currents were required (5 A), but no contamination could be detected in the chamber containing the substrate. The degree of neutralisation was about 50 % of the beam current and the filament could be operated for 6 hours. The introduction of a cathode (1 kV) in the bottom chamber, inevitably diverged the ion beam to some degree. This fact (and the need for 100 % neutralisation) necessitated another solution.

Finally, it was decided to build a plasma bridge neutraliser (PBN). The PBN consists of a small discharge chamber with a small orifice and a biased filament emitter (very similar to the Wehnelt cap). By heating the filament to emission temperature, a working gas (argon) is discharged to form a plasma inside the discharge chamber. The internal discharge is maintained by the “discharge regulator”, regulating the filament to body current. An emission power supply, connected to the center tap of the transformer supplying current to the filament, biases the filament negatively. This aids in electron extraction through the orifice toward the positive ion beam. As electrons are accelerated out of the orifice,

they ionise some of the argon gas also leaving the chamber. Accordingly, a plasma plume acting as a conductive path (called a plasma bridge) forms between the filament and the ion beam. The entire configuration is illustrated in Fig. 4.10.

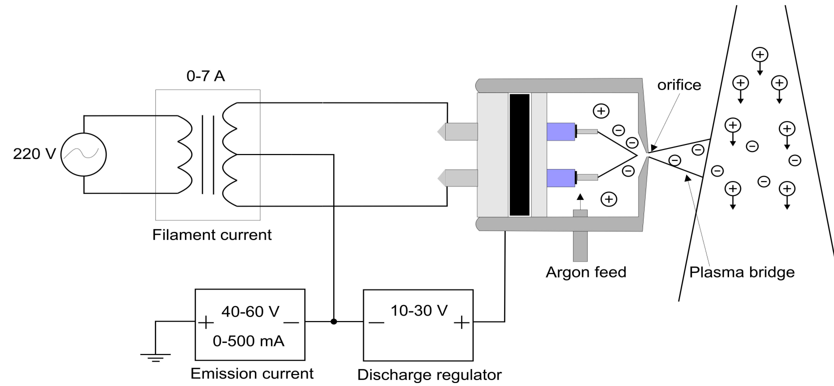

Figure 4.10: Plasma Bridge Neutraliser

Implementation of the PBN, displayed complete space charge neutralisation. The addition of argon gas in the bottom chamber does, however, increase the operating pressure slightly, which can affect the beam profile due to a shorter mean free path. After implementation of the PNB, operating pressures were still maintained around (2-3.5)x10^{-4} mbar with no visible change to spot size. The final Argon mill design is thus completed (see Fig. 4.11).

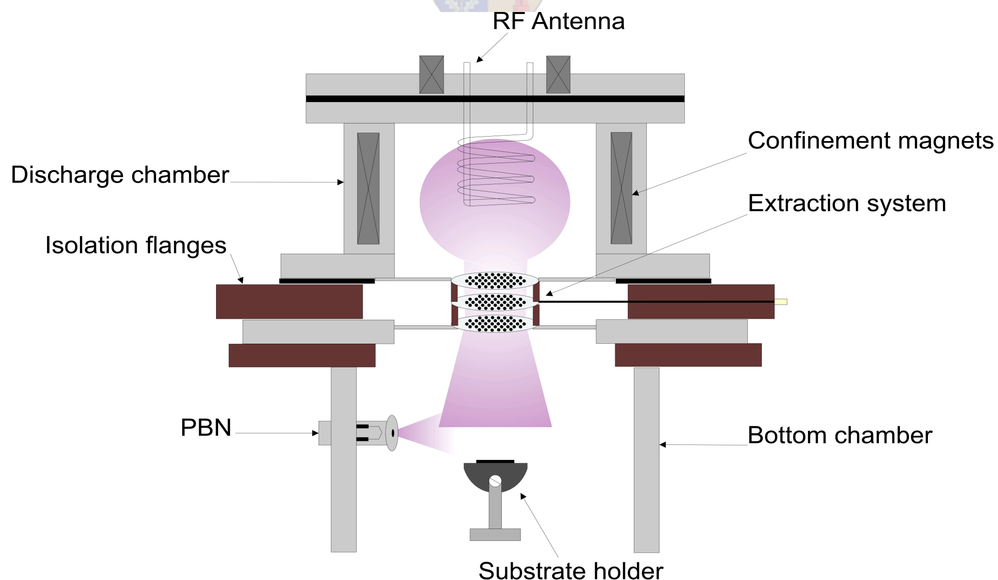

Figure 4.11: Complete Three-gridded Ion Beam System

4.4 Etch Profiles

Having implemented the final design of the Argon mill, this section aims to provide the tools to understand/interpret etch profiles that can be expected in an ion milling process. It should be noted that ion milling is a physical process only, where argon ions impinge on a surface and momentum transfer causes bond breakage and material ejection.

Ideally, we want the mask pattern to be transferred to the substrate or film material without any distortion to critical dimensions (CDs). In the case of ion milling several factors contribute to the loss in precision. As a first consideration, a highly collimated ion beam with minimum off-axis ion velocity components is preferred to ensure anistropic etching (see Fig. 4.12) [17]. This etching condition is related to the mean free path of the ions where lower pressures minimises loss of directionality and resulting isotropic features.

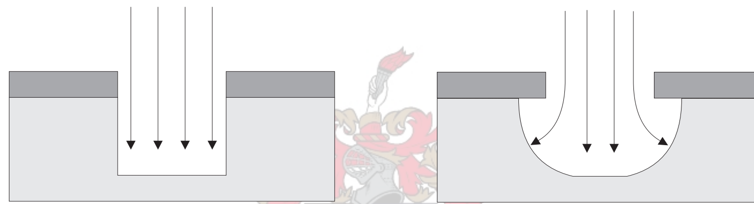

Figure 4.12: Isotropic and anisotropic etch profiles

Secondly, when performing dry etching, facets tend to develop on the mask edge (see Fig. 4.13(a)). This phenomenon occurs due to the inevitable rounded profiles of mask edges which have a faster etch rate. The etch rate of a specific material is a function of the incident beam angle relative to the material normal. For photoresist, the etch rate will be optimal for an incident beam angle of 60°[3] corresponding to pronounced faceting phenomena. These facets can be transferred from the mask to the substrate yielding rounded step-edges which is not suitable for grain boundary formation. Faceting should accordingly be minimised by using masks with near-90° angles and by preventing resist to reflow during baking.

The next etching phenomenon is trenching. This etch feature is largely dependent on the protective mask angle. The sloped edge of a mask can lead to some ions colliding with the mask sidewall at a glancing angle before reaching the substrate. Accordingly, a local

[3]see Chapter on Buffered Step-Edges for etch-rate-profile

increase in ion density results, causing trenches to form near the mask sidewall. In our in-house scenario where resist angles of 70° is optimal, trenching can become an important factor (especially for longer mill times). When milling metal masks, the bending of E-field lines due to altered surface topologies also promotes the occurrence of trenching due to the enhanced ion flux at feature edges.

Another important matter in determining the etch profile is the concept of selectivity (the difference in etch rates between the protective mask and the substrate/film etched). This concept will be studied in detail in the chapter on step-edge fabrication where the angle of the etched feature becomes crucial.

Finally, the occurrence of redeposition should be taken into account. Redeposition refers to the settling of sputtered particles on the sidewalls of the mask and the etched substrate. As was the case with trenching, the sloped sidewalls of the mask are the main contributing factors. Steeper sidewalls angles will limit the amount of redeposition. However, if sloped mask angles are an inherent process limitation, redeposition (and trenching) can be minimised by "shading" the mask sidewall sufficiently. This was accomplished by tilting and rotating the sample holder. The chapter on buffered step-edge fabrication will cover this concept in detail.

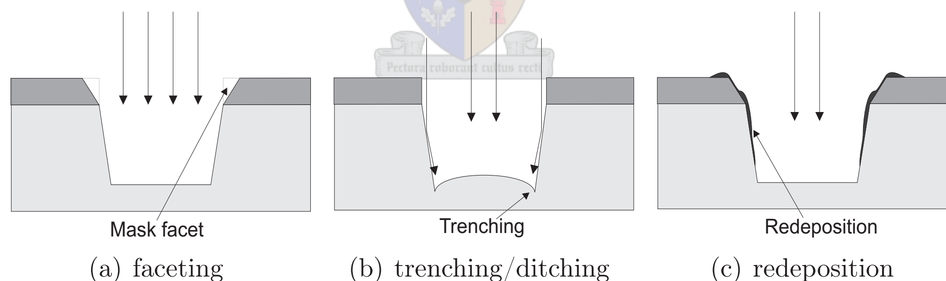

(a) faceting (b) trenching/ditching (c) redeposition

Figure 4.13: Features characteristic to ion milling

4.4.1 Examples of Device Patterning

The argon mill at Stellenbosch is now actively used to etch step-edge features as well as for the patterning of YBCO circuits. The resolution that is currently obtained in pattern transfer is excellent. As an example, Fig 4.14 illustrates a MgO step-edge covered with a patterned YBCO circuit with minimum dimensions of 4 μm.

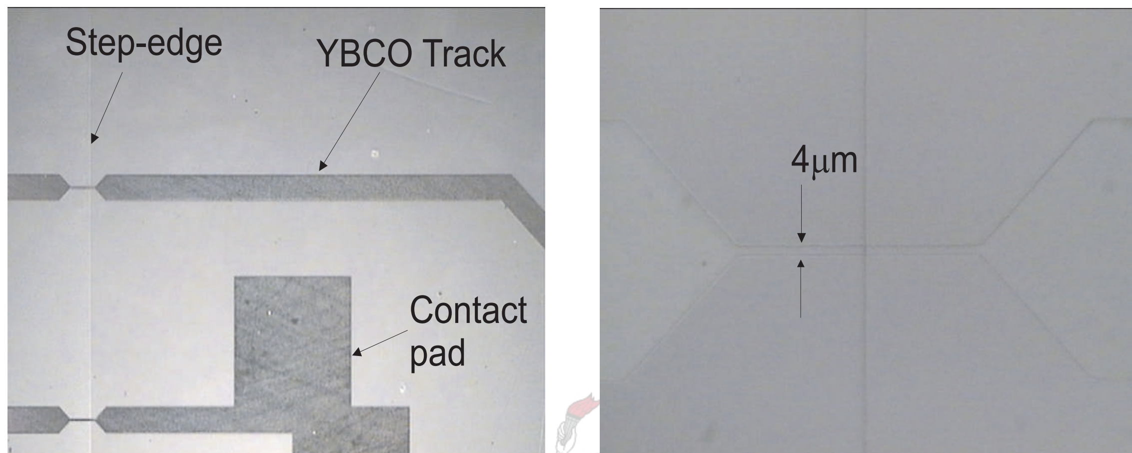

Figure 4.14: Typical etch resolution obtainable for circuit patterning

Fig. 4.15 illustrates an Atomic Force Microscopy (AFM) scan performed across the step-edge region. This sharp edge clearly demonstrates the resolution possible with dry etching. It should be noted that the YBCO track roughness was not introduced by the milling process, but is a result of the deposition process used.

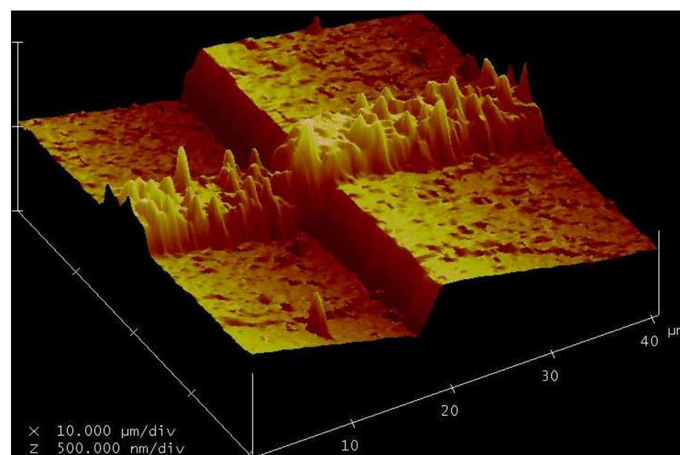

Figure 4.15: A three dimentional view of an edge profile

4.5 Chapter Overview

This chapter analysed the existing Argon mill system and identified critical limitations of the process. According to this analysis, a modification to the extraction system of the Argon ion mill was necessary to produce improved ion beam size and beam distribution. A three-gridded extraction system is discussed, implemented and tested successfully. This included space charge neutralisation by introducing a plasma bridge neutraliser to the system. Test results revealed good etch profiles at adequate etch rates. The reliable operation of the mill now eliminates the need to resort to wet etching techniques and was successfully integrated into the device fabrication process.

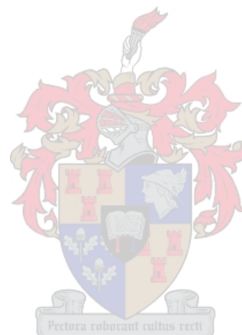

Chapter 5

Thin Film Deposition: Pulsed Laser and DC Magnetron Deposition

The future of HTS technology depends strongly on the development of reproducible thin film deposition technology. For this reason, the fabrication of high quality epitaxial thin films has been the subject of intense research over the past few years. Today, several deposition techniques exist to fabricate HTS thin films. Each technique has its advantages and drawbacks with Pulsed Laser Deposition (PLD) and sputtering being identified as the most popular processes to meet the stringent manufacturing requirements. It thus made sense to concentrate on these two processes to research YBCO deposition. Before 2005, there existed only a PLD deposition system at the University of Stellenbosch. The successes achieved in this respect were limited to films having a good critical temperature but poor surface roughness. Factors such as device miniaturisation, multilayer technology and reproducibility necessitate the fabrication of consistently smooth thin films.

This chapter addresses important theoretical aspects concerning thin film growth. This is followed by a brief description of the updated PLD system and the introduction of a new deposition system called an Inverted Cylindrical Magnetron.

5.1 Theory of Thin Films

In thin film formation, there exists two competing processes. The first process refers to the deposition of material (adatoms) on the substrate surface and the second is the removal of material from the surface through desorption or evaporation. The ratio between the

mass of material deposited to the mass of material impinging the surface is known as the sticking coefficient.

The most important kinetic process involved in thin film growth is the ability of an adatom to diffuse on a flat surface (terrace). Smooth surfaces cannot be grown if adatoms have insufficient surface mobility. The diffusion distance, λ, of an adatom is given by

$$\lambda \approx \sqrt{D_s \tau} \tag{5.1.1}$$

where D_s and τ represent the surface diffusion constant and mean residence time respectively [29].

The next mechanism in thin film formation is nucleation. This occurs when stable clusters of adatoms form and continue to grow rather than to dissolve back to smaller clusters of adatoms and single adatoms. Nucleation of a thin film initiates from energetically favourable places on the substrate surface. Substrates are not atomically flat, having steps, kinks and other kinds of defects which are preferred sites for nucleation. Lateral growth of the thin film will ultimately lead to clusters (also called islands) reaching a point of contact. When this happens, there exists an energetic driving force for the formation of a grain boundary which constitutes a lower energy state. This process is known as coalescence. Once a continuous film has formed through nucleation, growth and coalescence, thickening of the film is expected to occur via epitaxial growth on pre-existing grains [30],[31].

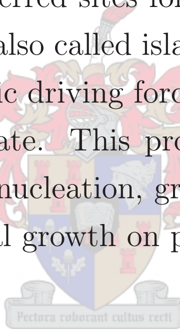
Pectora roborant cultus recti

5.1.1 Epitaxy

The specific crystallographic orientation between the thin film and substrate is governed by the crystal lattice parameters of the respective materials. Two basic types of epitaxy can be identified: homoepitaxy and heteroepitaxy. Homoepitaxy refers to the situation where the lattice parameters of the film and substrate match perfectly e.g. when the substrate and film are the same material. In this case, no strain is introduced at the film-substrate interface. In heteroepitaxy, there exist a slight lattice mismatch between the film and substrate. As a result, the interface can be strained or relaxed (see Fig. 5.1) [32].

Film growth will always try to minimise the interface energy, γ_I. This energy consists of interface energy due to the formation of a new interface, and the strain introduced due to lattice mismatching.

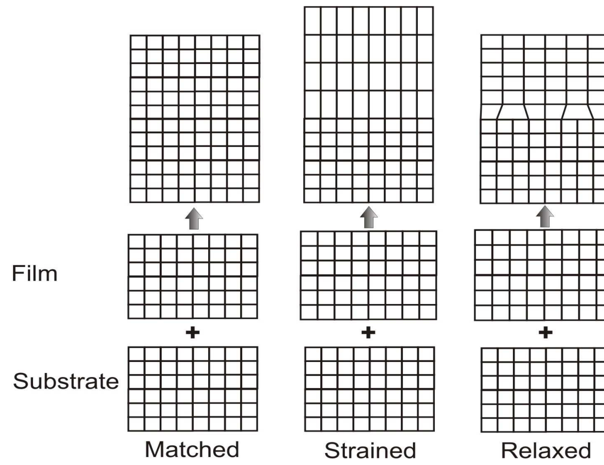

Figure 5.1: Illustration of heteroepitaxial growth for lattice-matched, strained and relaxed structures

5.1.2 Growth Modes

As epitaxial growth of thin films proceed, certain growth modes can be identified. Factors such as lattice matching, substrate morphology and adatom diffusivity play a critical role in the growth mode that will take place. Three growth modes have been identified experimentally: Layer-by-layer (Frank van der Merwe) growth, Island growth (Volmer-Weber) and Mixed growth (Stranski-Krastanov) [29].

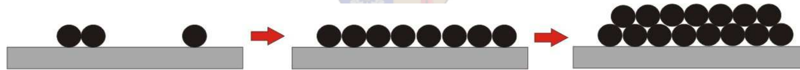

Figure 5.2: Layer-by-layer growth

When considering lattice-matched layers, a Layer-by-layer (Frank van der Merwe) growth mechanism is frequently observed (see Fig. 5.2). In this growth mode, film atoms are more strongly bound to the substrate than to each other. This growth mode is governed by the energy condition

$$\gamma_I + \gamma_F \leq \gamma_S \tag{5.1.2}$$

where γ_I, γ_F and γ_S is the interface, film and substrate surface energies respectively. The highest crystalline quality thin films are obtained in this mode.

Substrate step-edge spacing, l, and the adatom surface migration length play a critical role in characterising Layer-by-layer growth. In the case where $\lambda < l$, the majority of

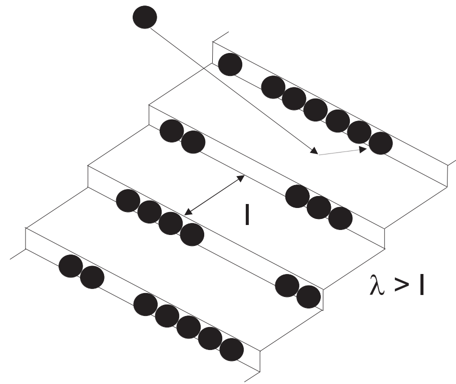

Figure 5.3: Stepflow growth

adatoms does not possess the mobility to reach surface features. As a result, the film will grow by nucleation of 2D islands. For the case where $\lambda > l$, the adatoms possess the mobility to migrate across the surface terraces and reach substrate features. Film growth is accordingly dominated by the attachment of adatoms to the step edges of the substrate terraces as shown in see Fig. 5.3 (known as step flow growth).

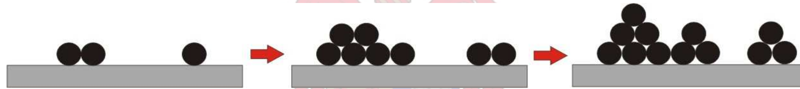

Figure 5.4: Island growth

Island growth (Volmer-Weber) is characterised by the formation of three dimensional islands (see Fig. 5.4). The formation arises when atoms are more strongly bound to each other than to the substrate. Three dimensional island growth can occur due to strain introduced by lattice mismatched substrates (large γ_I) which makes this growth formation energetically more favourable. Another possible cause is the slow diffusivity of the adatoms on the substrate. An increased deposition rate and decreased substrate temperature enhances this type of growth. The governing energy condition is now given by

$$\gamma_I + \gamma_F > \gamma_S. \tag{5.1.3}$$

In Mixed growth (Stranski-Krastanov), the thin film initially grows layer by layer with three dimensional growth following later on (see Fig. 5.5). The reason for the change in growth is due to changing surface energies (more strain introduced as film becomes thicker)

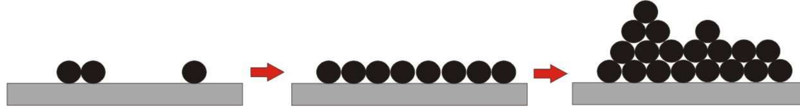

Figure 5.5: Mixed growth

and changing diffusion energies.

5.2 Substrate Considerations

To ensure the growth of high quality thin films, the choice of substrate is crucial. From a film growth perspective, film-substrate lattice match, thermal expansion match and chemical compatibility are the most relevant factors when deciding on an appropriate substrate.

To address the lattice matching requirement, the crystal structure of the HTS cuprate should be examined. HTS cuprates are nearly tetragonal in their crystal structure which thus make oxides with a square-planar surface orientation, such as the (001) face of cubic oxide crystal, most suited for c-axis-oriented HTS films. Thermal expansion matching becomes an important consideration owing to the extreme deposition temperatures associated with HTS films. A significant difference in the thermal expansion coefficient between substrate and film will be the source of stress in the film which, in the worst case, may lead to severe adhesion problems or even lead to cracking of the film [29]. Finally, chemical compatibility ensures that no interdiffusion occurs at the interface of the thin film and substrate material which can inhibit good epitaxy and may prevent the formation of the HTS phase.

Other considerations justifying a particular choice of substrate may involve cost, availability, surface morphology (roughness) and intended application field. A typical example relates to HTS microwave devices, where the substrate should not only support growth of good quality epitaxial films, but also have desirable high frequency properties.

Since YBCO was the film under study in this thesis, substrates compatible with this HTS material will be the point of focus. These substrates can be categorised into perovskites such as $SrTiO_3$, $LaAlO_3$ and $NdGaO_3$ or non-perovskite including MgO and Al_2O_3 (see

Table 5.1). Perovskite substrates provide good lattice matching due to the similarity in crystal structure, but possess unfavourable microwave properties. Some non-perovskite oxides are of interest as HTS substrates since they possess advantageous physical properties for specific applications. MgO, despite possessing a significant lattice mismatch with most HTS compounds, has become a popular substrate due to its availability as an inexpensive substrate with a temperature-independent dielectric constant, ϵ_r, and a low dielectric tangent loss [13].

Substrate	Dielectric Constant (ϵ_r)	tan δ (at 77 K,10 GHz)	Lattice Mismatch (%)
$SrTiO_3$	277	2 x 10^{-2}	2
$LaGaO_3$	25	6 x 10^{-3}	1.5
$LaAlO_3$	24	7.6 x 10^{-6}	2.2
$NdGaO_3$	23	3.2 x 10^{-5}	0.3
MgO	9.6-10	6.2 x 10^{-6}	9
Al_2O_3	9.4-11.6	1.5 x 10^{-8}	9.4

Table 5.1: Properties of popular HTS substrates [1]

Pectora roborant cultus recti

One of the aims in fabricating high quality thin films at Stellenbosch, was to lay the foundation for producing superconducting microwave devices. Accordingly, the substrate used throughout this thesis was MgO (see Table 5.1 for a listing of popular HTS substrates). Several fabrication challenges are introduced by this choice. The epitaxial growth of YBCO (a non-cubic material), onto cubic substrates such as MgO with a 9% in-plane lattice mismatch, introduces significant strain in the thin film. The lattice parameter of the film will tend to expand to match the substrate lattice constant. The strain energy in such a lattice mismatched system increases with film thickness until at some critical thickness, this strain needs to be relieved by the formation of misfit dislocations near the substrate-film interface [29]. Accordingly, precise control of film thickness will be a critical process parameter. MgO is also renowned to be moisture sensitive, which will necessitate minimum atmospheric exposure before deposition.

5.3 Growth Mechanisms in PVD

As mentioned, two methods of thin film deposition were researched in this thesis: PLD and sputtering. These deposition methods can be classified as physical vapour deposition (PVD) techniques. PVD techniques involve the production of a vapour flux of film species

which travel to a substrate where film growth commences [33]. This flux can contain atomic, ionic, molecular and even clusters species. In PVD there exists a need to balance the arrival rate of the film species with surface mobility allowing adatoms sufficient time to reach equilibrium sites [31]. This implies a complex optimisation process involving, amongst others, substrate temperature, chamber pressure, target substrate distance and deposition rates.

5.3.1 HTS Thin Film Growth

Growth of cuprate films such as YBCO are a complicated process owing to the complex multicomponent crystal structure of these materials. HTS film growth has demonstrated to be prone to a variety of defects and growth morphologies necessitating extreme deposition conditions to achieve good film quality. When growing HTS thin films, a few desired properties exist to serve as guidelines when optimising film quality. These properties include: epitaxial growth, avoidance of large angle grain boundaries, no secondary phases or outgrowths and low surface roughnesses.

The growth mechanisms in HTS films are still under much discussion, allowing only for generalised observations. Firstly, the layered crystal structure of YBCO results in anisotropy in the crystal growth rate. As a result, YBCO grows faster along the a-b plane than along the c-axis [13]. This growth mechanism favours epitaxial growth with the c-axis perpendicular to the substrate surface. Secondly, these films will grow with a granular morphology. The intergranular properties will dominate the superconducting behaviour such as critical current density, J_c, and microwave surface resistance R_s. Accordingly, it is necessary to limit in-plane disorder of grains and maximise grain size. Typically, Stranski-Krastanov growth of the film is observed on lattice-matched substrates while on (100) MgO, the film tend to nucleate by a Volmer-Weber island mechanism due to the lattice mismatch. Several reports of YBCO growth, manifested as growth spirals consisting of atomically flat terraces with growth steps one unit cell high exist [29]. These growth spirals presumably originate from screw dislocations in the film. Finally the occurence of secondary phases can manifest as outgrowths on the film surface. Typical outgrowths that can appear are Y_2O_3, $CuYO_2$ and CuO impurities. These outgrowths severely influence the surface morphology necessitating strict control of target stoichiometry and oxygenation levels during deposition.

Having discussed the basic theory behind HTS thin deposition, the focus can be directed to the deposition techniques used at the University of Stellenbosch.

5.4 Conventional Pulsed Laser Deposition

PLD is a versatile technique for preparing a wide range of thin films and multilayer structures. The basic operation is based on focusing a high energy laser beam onto a target material. The laser energy is accordingly absorbed by the target material and converted into thermal, chemical and mechanical energy to cause evaporation of energetic target species. This resulting cloud of species containing atoms, molecules, electrons, ions, clusters, micron-sized solid particulates and molten globules is known as the ablation plume [34]. The collisional mean free path inside the plume is very short, resulting in the plume rapidly expanding into the vacuum away from the target surface. The plume condense onto a substrate aligned with the plume direction where film growth commences (see Fig. 5.6).

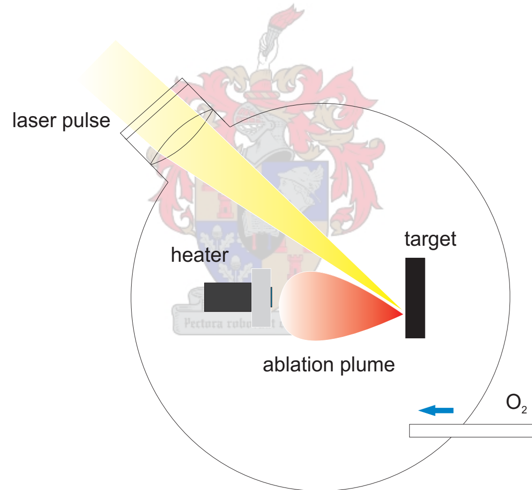

Figure 5.6: A conventional Pulsed Laser Deposition system

The disadvantages of PLD are the presence of micron-sized particulates contributing to poor surface roughnesses and the narrow forward angular distribution of the plume making large-area deposition very difficult.

5.4.1 The PLD System

The PLD system at the University of Stellenbosch was designed and manufactured at iThemba Labs (then known as the National Accelerator Centre) by Maritz et al in 1995.

The laser used is a Lambda Physic EMG 203 MSC XeCL excimer laser with a 30 ns pulse duration and a wavelength of 308 nm. The PLD chamber is fitted with a rotational multi-target holder configuration allowing for the in situ deposition of up to 6 materials. The current heater configuration is able to reach temperatures of 800°C. The two turbo molecular pumps in conjunction with a roughing pump allow a base pressure of $\pm$8x10^{-6} to be reached. These attributes make the system very suited for the deposition of oxide-superconductors such as YBCO.
The system was optimised in 2001 by P.A. Rottier [18] producing YBCO films with good superconducting properties but poor surface roughnesses. In 2004, F. W. Graser attempted to improve the surface quality by introducing a shadow mask. This significantly improved the surface roughness from 200 nm to around 30 nm. Unfortunately, the films lost their superconducting properties in the process. Thus, at the commencement of this research no viable deposition method existed to study Josephson junction devices (not to speak of multilayer applications).

5.4.2 Pulsed Reactive Crossed-Beam Laser Ablation

Recently, a modification was made to the PLD system by introducing a pulsed oxygen source to the system. This concept was first introduced by Gupta et al in 1991 [35] to test the effect of a lower background pressure on the superconducting properties of YBCO thin films. The conventional PLD system (pre-2006) was accordingly fitted with a pulsed valve in close proximimity of the ablation target. The gas jet was directed at the substrate with an incident angle of approximately 25°. This setup enables the release of temporally and spatially localised gas "packets" synchronised with the laser beam pulses. Ideal synchronisation occurs when the densest region of the gas pulse passes in front of the substrate just as the ablation plume is about to reach the substrate vicinity.

The University of Zürich extended this idea and proposed a so-called Pulsed Reactive Crossed-Beam Laser Ablation method (see Fig. 5.7) [36]. This setup closely resembles the system introduced by Gupta et al, but in this case the gas jet is directed just in front of the target material. Synchronisation is now obtained when the densest region of the gas pulse passes in front of the target just as the ablation plume is formed. This will allow the plasma to expand and propagate through the gas pulse. Energy from the plasma species is transferred to the gas particles through collisions which enhance the chemical reactivity of the gas particles. The effect of this added reactivity is evident when observing the ab-

lation plume which becomes larger and brighter. As the ablation plasma leaves the gas pulse, it rapidly expands into the vacuum. As the mean free path in vacuum significantly reduces the probability of further particle collisions, the reactivity of the plasma species are now retained on their way to the substrate. If a constant background gas pressure was employed, rethermalisation of these species would occur.

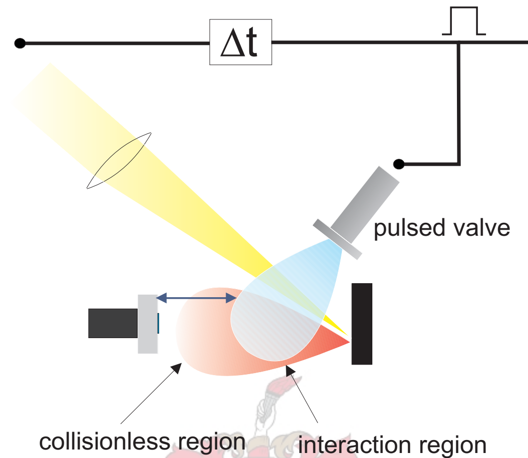

Figure 5.7: Pulsed Reactive Crossed-Beam Laser Ablation

The PLD configuration used in this thesis is the method as proposed by Gupta et al. The optimisation of the pulsed oxygen system was conducted in a group context and will not be described in this thesis. Results included YBCO films with critical temperatures approaching 90 K and surface roughnesses in the order of 20 nm. Instead, focus will fall on the design and optimisation of a new in-house sputter deposition system called an Inverted Cylindrical Magnetron.

Pectora roborant cultus recti

5.5 Inverted Cylindrical Magnetron Sputtering

Due to fluctuations in laser energy making it difficult to standardise the PLD process, as well as the need for better surface roughnesses, different deposition methods were investigated. Sputter deposition is a member of the PVD family, which utilises physical sputtering to create a source of particles (vapour flux) which subsequently condense onto the substrate and nucleate into a film. Generally, sputter deposition offers the following advantages as compared to related deposition techniques:

- Excellent film uniformity, particularly over large areas.
- Good film adhesion.
- Deposited films demonstrate bulk-like properties, which are predictable and stable.
- Surface smoothness and thickness control.

There exists several varieties of this deposition method. In this thesis, the Inverted Cylindrical Magnetron Sputtering (ICM) system was chosen.

5.5.1 Design Considerations and Basic Operation

Figure 5.8 illustrates the basic layout of the ICM system.

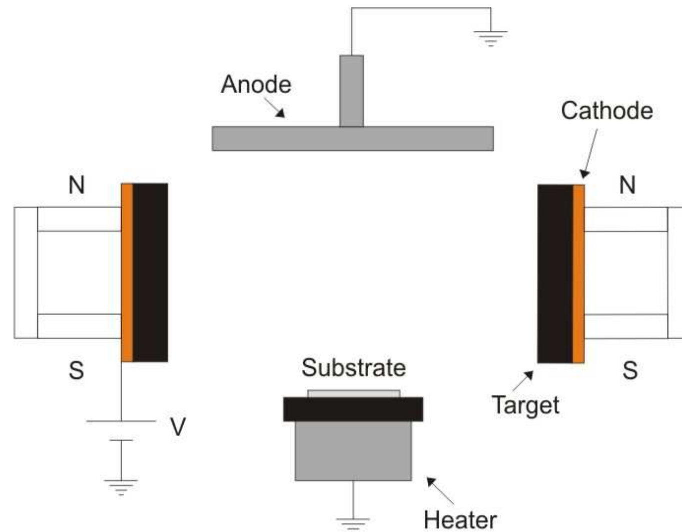

Figure 5.8: Schematic view of Magnetron Sputtering System

The operation of a magnetron is based on creating a plasma discharge in the vicinity of a target and accelerating ions from the plasma to the target to sputter its surface. To ignite the plasma, an inert gas such as argon is fed into the deposition chamber. By natural cosmic radiation there will exist some ionized Ar^+-ions. By applying a negative potential of a few hundred volt to the conductive target, these argon ions will accelerate toward the target and set material free. These collisions also lead to the emission of secondary electrons. These electrons play a crucial role in the subsequent ionization of the gas from which a self sustaining glow discharge starts.

To design an effective magnetron sputtering system a high ionisation probability is essential. One way to accomplish this is to increase gas pressure, which in turn will increase the probability of secondary electrons colliding with argon atoms.
The alternative is to minimise the electron loss rate and ensuring the electron density is highest in the vicinity of the target material. By introducing a H-field (provided by a rare earth magnet configuration) parallel to the cathode surface (orthogonal to applied E-field) an E x B drift of electrons results (Hall effect). These drift paths form closed loops parallel to the cathode face. As a result the secondary electrons, which are emitted from the cathode because of ion bombardment, are confined to the near vicinity of the cathode. The many energetic collisions with the argon gas ensure a sustainable ionization rate [37].

Utilising this approach to sputtering, plasma ignition can occur at pressures much lower compared to conventional sputtering. Another benefit of using magnetron sputtering is the higher deposition rates which can be realised at these lower pressures. Having the basic plasma requirements sorted out, we have to shift our focus to the target material, YBCO.

5.5.2 Sputtering of YBCO

One disadvantage of DC magnetron sputtering is the requirement that the target material has to be conducting, otherwise the target surface would eventually charge up to the applied voltage and the plasma will be extinguished. An YBCO-target in its orthorhombic phase meets this criterion, but it is well known that oxygen diffusion occurs commonly in YCBO[1]. When this happens, the target will become tetragonal and insulative.

To overcome this problem, oxygen (reactive gas) must be added to the gas mixture to ensure the target maintains its oxygen levels. Introducing a reactive gas, however, introduces new problems. Negatively charged oxygen ions will be accelerated away from the negatively charged target, bombarding the growing film and typically cause preferential resputtering of Ba and Cu [38]. Fortunately, this effect can be taken care of by converting the magnetron to an off-axis magnetron configuration [33]. Such a configuration, known as an Inverted Cylindrical Magnetron, utilises a cylindrical target, orientated off-axis with respect to the substrate. This setup is advantageous, because it significantly lowers the probability of energetic ions bombarding the growing film. For details on the design schematics, see [39].

[1] Oxygen atoms are highly mobile when the material is heated resulting in oxygen depletion

5.5.3 Final Design

Having established the basic operation of the ICM, attention has to be given to some practical problems. Firstly, the plasma chamber will reach very high temperatures which may cause damage to the rare earth magnets. Water cooling was accordingly installed to serve as protection. The next consideration was the heater element. For this purpose, a chrome-nickel based cartridge was used and mounted in a stainless steel sheath to limit corrosion. This heater was able to reach temperatures of 770°C which is well suited for depositing YBCO. A practical issue that arose during initial deposition runs, was the fact that the substrate temperature tend to rise considerably as the deposition time is lengthened. This could be due to a fall in the internal resistance of the heater element or due to the steady rise in chamber temperature. Accordingly the heater was monitored in 20 minute intervals. In any deposition process, vacuum requirements are essential to minimise impurities levels in the growing film. Initially, a diffusion pump was used to meet high vacuum requirements allowing a base pressure of 1x10^{-6} mbar to be obtained. ICM sputtering, however, takes place at high pressure which could not be sustained by the diffusion pump for long periods of time. As a result, sputtering was done with a roughing pump only which provided good pressure control but a base pressure of only 8x10^{-2} mbar. This is a definite process limitation and results should improve when a turbo molecular pump can be added to the system.

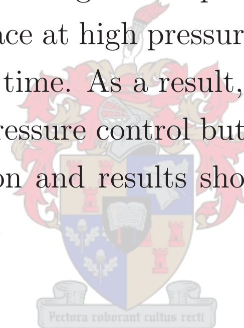

5.6 Chapter Overview

This chapter presented an introduction to the basic principles of thin film growth. The major contributing factors determining the mechanisms behind film formation such as lattice matching, substrate defects and adatom diffusivity were discussed. Next, the thin film deposition techniques at Stellenbosch were presented. This included the PLD system as well as a new in-house deposition technique called Inverted Cylindrical Magnetron Sputter Deposition.

Chapter 6

Characterisation of YBCO Films Deposited by ICM

A major part of this thesis was dedicated to the fabrication of YBCO thin films. To realise this aim, it was necessary to evaluate critically the thin film quality by taking into account both film growth and electrical properties. In this thesis, four analysis techniques were used to characterterise film quality: X-ray diffraction, Rutherford Backscattering Spectroscopy, Atomic Force Microscopy and susceptibility testing. This chapter will provide a brief discussion of each characterisation technique, followed by an in-depth study of the optimisation of YBCO films using the Inverted Cylindrical Magnetron deposition system.

6.1 X-Ray Diffraction

X-ray diffraction (XRD) is a very powerful analytical technique used to extract information about materials having some degree of crystallinity [40]. One of the standard analysis techniques, is the so-called θ-2θ diffraction scan, which can give information on the phase, orientation and lattice parameters of the thin films under test. During such an analysis, the thin film is radiated with a beam of monochromatic x-rays of wavelength λ. As x-rays penetrate the film crystal structure, they get reflected from different atomic planes. If the path length between successive atomic planes are an integer multiple of the x-ray wavelength, constructive interference of the reflected rays will occur. This condition is known as the Bragg law, formulated as

$$2dsin\theta = n\lambda \quad for\ n = 1, 2, 3... \tag{6.1.1}$$

where d is the distance between the lattice planes (see Fig. 6.1).

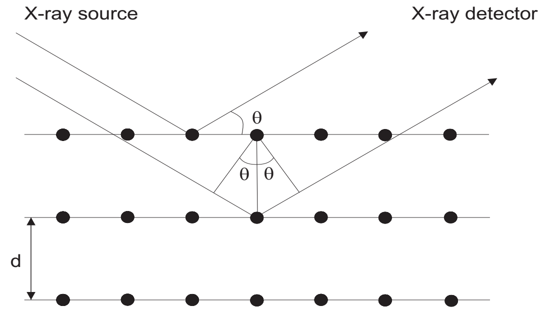

Figure 6.1: The scattering of X-rays from atomic planes

Each crystalline material has a characteristic atomic structure and it will diffract x-rays in an unique pattern (a "fingerprint" of the material). It is thus easy to compare experimentally obtained XRD patterns with this standardised "fingerprints" whereby a qualitative analysis is possible. A typical θ-2θ scan for an YBCO thin film deposited on an MgO substrate should illustrate the presence of (00l) peaks corresponding to a well-crystallised single orthorhombic phase with the c-axis oriented perpendicular to the surface of the film. By utilising Bragg's law, we can further determine the the c-axis lattice parameter which gives a good indication of the oxygen content of the film (a typical value should be around 1.168 nm [41]).

Pectora roborant cultus recti

6.2 Rutherford Backscattering Spectroscopy

Rutherford Backscattering Spectroscopy (RBS) is an analysis technique which can be used to investigate the elemental stoichiometry, thickness, diffusion profiles between interfaces and crystal imperfection of thin films [42].

In a RBS system, a mono-energetic ion beam (1-4 MeV), typically Helium, bombards the sample to be analysed. The incident alpha particles (He^+) will interact with the target atom in a way similar to the elastic collision of two spheres. This elastic collision can be described by conservation of energy and momentum considerations (see Fig. 6.2). The ratio of the energy of the backscattered ions, E_1, to the energy of the incident ions, E_0, is called scattering kinematic factor,

$$K = \frac{E_1}{E_0} = \left\{ \frac{[1-(\frac{M_1}{M_2})^2 sin^2\theta]^{\frac{1}{2}} + (\frac{M_1}{M_2})^2 cos\theta}{1+(\frac{M_1}{M_2})} \right\}^2 \tag{6.2.1}$$

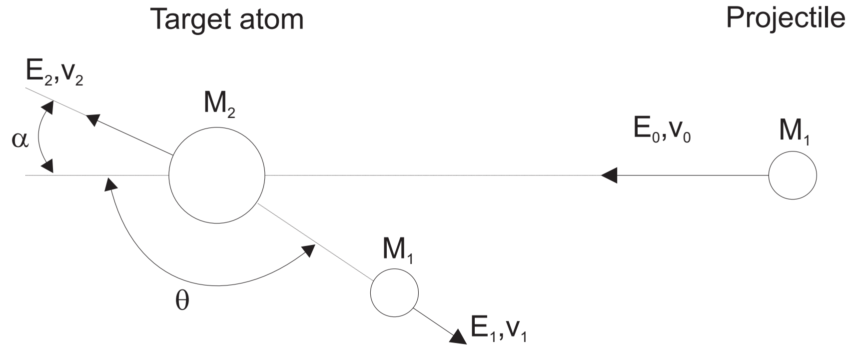

Figure 6.2: Backscattering of incident alpha particles by a stationary target atom

where M_1 is the mass of the incident ions, M_2 is the mass of the sample atom, and θ is the angle between the incident ion velocity vector and the backscattered ion velocity vector. By thus analysing the energy of the backscattered ions, given the analytical geometry, it is straightforward to determine the atomic mass of the target atoms constituting the thin film. Using a RBS simulation programme such as RUMP [43], the experimental data can be interpreted to display energy channeling profiles and to determine film thickness and composition. Typical phenomena of note in a channeling profile include[1]:

- The effect of relatively large lattice mismatches will be evident from the presence of a large density of defects resulting in dechannelling at the film-substrate interface.
- Any interfacial reaction between the substrate and the film will manifest as tailing in the elemental distribution of the film with a corresponding sharp slope at the front of substrate elemental distribution.
- A slow increase in the slope of counts from the film surface can indicate a decrease in the number of film defects (less dechannelling). It should, however, be noted that the density of defects for a strain-relieved (heteroepitaxial) layer is generally highest near the interface and decreases with distance from the interface.

RBS can thus provide a wealth of information about the thin film. The analysis is however slightly destructive since energetic ions may cause defect formation and ion implantation. For the analysis of YBCO thin films, the presence of a light element such as oxygen complicates analysis owing to the fact that RBS is less sensitive to light elements compared to heavy elements.

[1]Examples of channeling profiles will follow later in the chapter

6.3 Atomic Force Microscopy

Atomic force microscopy (AFM) is widely used to characterise the surface morphology of thin films. AFM maps the surface of a sample by measuring the inter-atomic forces between a tiny tip on a cantilever and the surface atoms of the sample. AFM can be operated under two operation modes: contact mode (suitable for hard surfaces) and tapping mode (used for softer surfaces). In this thesis, the contact mode of the AFM was used used whereby the AFM tip and the film surface are in contact and the repulsive forces are measured. The measurement is, however, non-destructive due to the nanonewton-sized force being applied on the tip.

The output of the AFM is processed by software allowing the user to view two-dimensional or three-dimensional images of the surfaces measured. The resolution obtainable with AFM enables one to see nano-particles on surfaces. Surface data such as rms-roughness and hill-valley profiles can also be extracted which provide insight into film growth mechanisms. AFM can provide invaluable information regarding grain orientation, the presence of outgrowths and growth features such as pitting (a measure of film density).

6.4 Susceptibility Tests

Pectora roborant cultus recti

To characterise the superconducting properties of the thin films, an ac susceptibility test setup was used. Such a test will yield the critical temperature, T_c, and illustrate the transition into superconductivity (ΔT) of the thin film. This test is commonly replaced with 4-point probe measurements in literature. The 4-point probe measurement gives the dc resistance of the thin film but requires the deposition of gold pads and wire bonding. The susceptibility test setup does not require prior sample preparation and yields results that are more representative of the entire film.

The test setup consist of a cold finger, a liquid helium cryo-cooler and a temperature controller. The sample is mounted between two planar coils situated inside the cold finger. The primary coil is driven by a 1 MHz sinusoidal waveform, which induces a magnetic field perpendicular to film surface. The secondary pickup coil, return a signal to the controller indicating the percentage signal that is sensed. Below the critical temperature of the sample, it will expel any magnetic fields according to the Meissner theory. During the process of cooling down the cold finger, the temperature and corresponding percentage

susceptibility measurements are sampled and sent serially to a computer where the results are displayed.

6.5 Characterisation of ICM

After the ICM design was completed, it was necessary to characterise the deposition system (for an YBCO target material). As with most deposition techniques, it is difficult to isolate the effect of certain system parameters. The most important parameters were identified as: input power (arc voltage and arc current), total pressure, oxygen partial pressure, and substrate temperature. From initial testing and theoretical considerations, the following could be concluded:

6.5.1 Input Power

Since the arc voltage is a function of the conductivity of the sputter gas, input power was controlled by varying the arc current. After performing several deposition runs on Alumina substrates at a constant pressure (150 μmHg), it was confirmed that the arc current has a dominant influence on the deposition rate of the thin film. Accordingly, the arc current will play a significant role in determining the time available to arriving flux particles for surface diffusion and nucleation with other adatoms/growth centers [31]. The applied voltage determines the maximum energy with which sputtered particles can escape from the target, thus being an important factor in the negative ion effect.

Pectora roborant cultus recti

6.5.2 Substrate Temperature

The substrate temperature will significantly contribute to the energy available at the substrate surface. This will influence the diffusivity of adatoms and as a result affect the growth mode that will take place. The kinetics of epitaxial film growth, along with the thermodynamic requirements for proper $YBa_2Cu_3O_{7-\delta}$ phase formation, typically require deposition at substrate temperatures of 650-800°C in an oxidising ambient.

6.5.3 Argon/Oxygen Pressure

Sputtered atoms experience collisions determined by the mean free path which is inversely proportional to the gas pressure. Collisions with gas particles cause a reduction in the

flux particle energy and randomise their path directions in a process called thermalisation (the reduction of high energy species towards thermal energies). The energy of sputtered particles reaching the substrate (affecting their ability to diffuse on the surface) decreases with increased gas pressure and increased target-substrate distance. Thermalisation can, however, oppress the negative ion effect whereby the presence of negatively charged particles such as O^-, O_2^- and BaO^- are accelerated away from the cathode, bombarding the substrate surface [44]. This bombardment can result in etching or preferential resputtering of the thin film causing surface damage and affecting stoichiometry.

By increasing the total gas pressure, the ionization probability is increased. This increases the conductivity of the gas and also decreases the break-through voltage. Very little ion bombardment is thus expected due to thermalisation and lower energy at the cathode. Longer deposition times can make this operating region not too favourable.

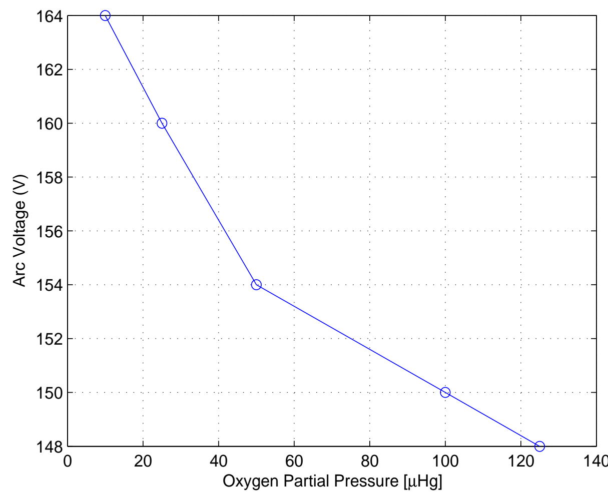

Figure 6.3: The effect on arc voltage for varying O_2 partial pressure

The introduction of oxygen into the plasma not only aids in retaining target conductivity. The sputter flux is also enriched with oxygen content reaching the substrate with high reactivity and an increased probability to be incorporated in the thin film. The dependence of the arc voltage on the oxygen partial pressure is illustrated in Fig. 6.3 for a constant pressure of 150 μmHg. This reduction in the break-through voltage for higher oxygen/argon ratios could thus further limit ion energies.

6.6 Experiments

Optimisation was done by keeping in mind the most prevalent problems that can hamper the quality of the resulting film. The first and most significant problem is the influence of energetic ions (or neutrals) that can cause resputtering and reduced surface quality. Secondly, the effect of substrate temperature is critical to improve the diffusivity of the adatoms for improved growth conditions. Lastly, the total pressure was studied to control the effect of thermalisation on the deposition process. Too much thermalisation can, for example, inhibit adatom mobility requiring higher substrate temperatures which is not desirable. It is clear that most of these parameters are interdependent, leading to the conclusion that there exist more than one route to optimisation. During optimisation, practical considerations such as reasonably low substrate temperatures and a realistic deposition rate (determined by total pressure) were taken into account. These two parameters place boundary conditions on two of our critical parameters, which assisted in choosing suitable parameter variation.

To study the effect of pressure (total and partial oxygen) and temperature, it was necessary to find suitable parameter values for the other variables in our deposition process. This included the input power, target-substrate distance, and annealing process. It was determined experimentally that an input power of 60 W produces a sufficient deposition rate without causing micron-sized particles to dislodge from the target. The target-substrate was fixed at 15 mm (inherent design limitation) while the optimal annealing profile was obtained by conducting several experiments during which only the annealing procedure was varied. The annealing profile that was finally used consisted of two stages: a high temperature anneal at 680°C for 10 minutes, followed by a 45 minute low temperature anneal at 480°C. It should also be noted that before any experiments were conducted, the YBCO target was pre-sputtered to remove any contamination and large particles from the target surface. All runs were performed on the same quality MgO substrate mounted onto the heater by silver paste to ensure good thermal contact.

Finally, only ten experiments were included in this thesis to convey the effect of the critical parameters: oxygen partial pressure, total chamber pressure and substrate temperature. The influence of each of these parameters are qualitatively investigated with respect to growth and electrical characterisation. Each sample was accordingly characterised by XRD, RBS/channeling analysis, AFM and susceptibility tests.

6.6.1 Oxygen Partial Pressure Variation

Initially, it was decided to investigate the influence of the partial oxygen pressure on the film quality. The experiments were conducted at a constant temperature of 740 ^{o}C, and a constant total pressure of 150 μmHg for 90 minutes each. Reported values for argon/oxygen ratios varies quite considerably, which justifies the wide range of values chosen.

6.6.1.1 Growth Characterisation (Figs. 6.4 - 6.8)

The θ-2θ scans illustrate the presence of the sharp and well-defined (00l) peaks corresponding to a crystallised orthorhombic phase. The films are thus preferentially oriented with the c-axis perpendicular to the surface of the film. The presence of a (103) peak in Fig. 6.5(a) corresponding to a 1:1 argon/oxygen gas ratio is visible indicating some deviation from pure c-axis growth orientation. The introduction of small peaks at 21.5-21.8^{o} in Figs. 6.6(a) and 6.7(a) for higher oxygen levels are probably due to secondary phase oxides manifested as outgrowths. These peak are, however, negligible when compared to the counts of the dominant (00l) peaks. When considering the c-axis lattice parameters, it coincides fairly well with the accepted crystal constant reported in literature of 1.1680 nm for $YBa_2Cu_3O_7$ [13]. The reduction in the c-axis lattice constants is clearly related to the increase in oxygen in the sputter gas indicating better oxygenation in the film.

From the RBS analysis, it is firstly clear that there exists no interfacial reaction between substrate and film (indicated by the absence of a tailing profile in the elemental distribution of the film). Furthermore, all profiles exhibit a change in slope in the film spectrum for both Ba and Cu, which can be attributed to loss of these elements from the surface of the film. The compositional ratio of Y:Ba:Cu as determined by RBS analysis is illustrated in Fig. 6.8(a). The composition was determined with a least squares fit between the simulated spectrum and the experimentally obtained data. It is evident that the best stoichiometry is achieved when the $O_2 : Ar$ ratio is 2:1. At low oxygen pressure, there exists a deficiency of Ba and Cu atoms which is most likely due to the resputtering effect of negative ions. This makes sense considering the higher arc voltages in this operating region (see Fig. 6.3) which lead to more energetic ion bombardment and preferential resputtering of the Ba and Cu atoms. The Cu deficiency at high oxygen partial pressure could not be explained. RBS analysis was also used to obtain the thicknesses of the deposited films. This results is summarised in Table 6.1.

Pectora roborant cultus recti

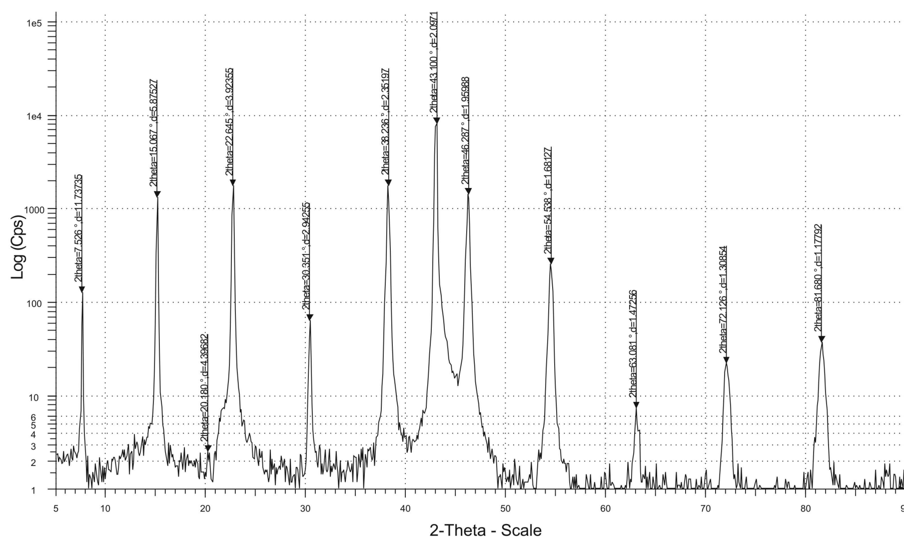

(a) X-Ray Diffraction Pattern

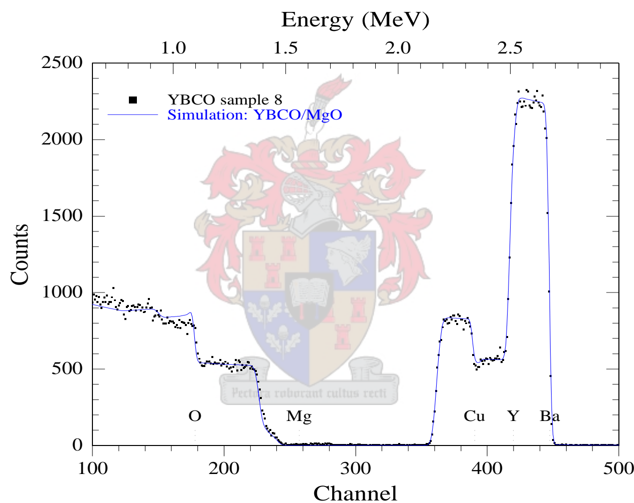

(b) RBS Channeling analysis

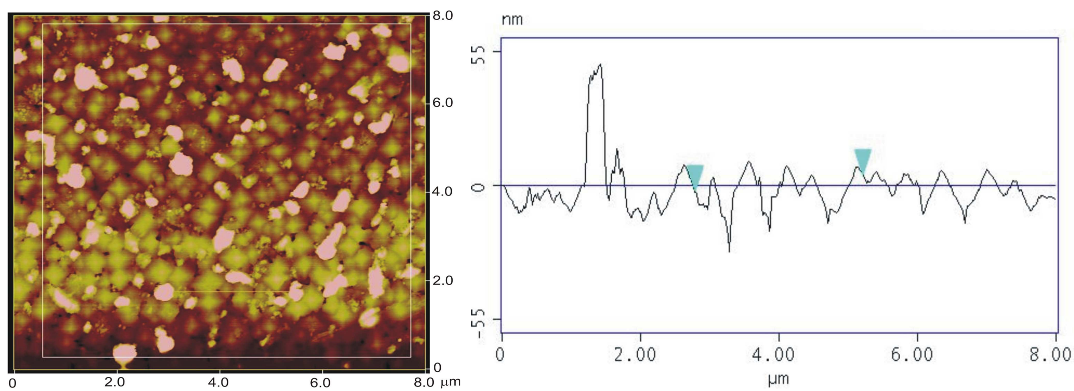

(c) AFM Surface Morphology profile

Figure 6.4: Growth Characterisation Measurements for an O_2:Ar ratio of 1:2

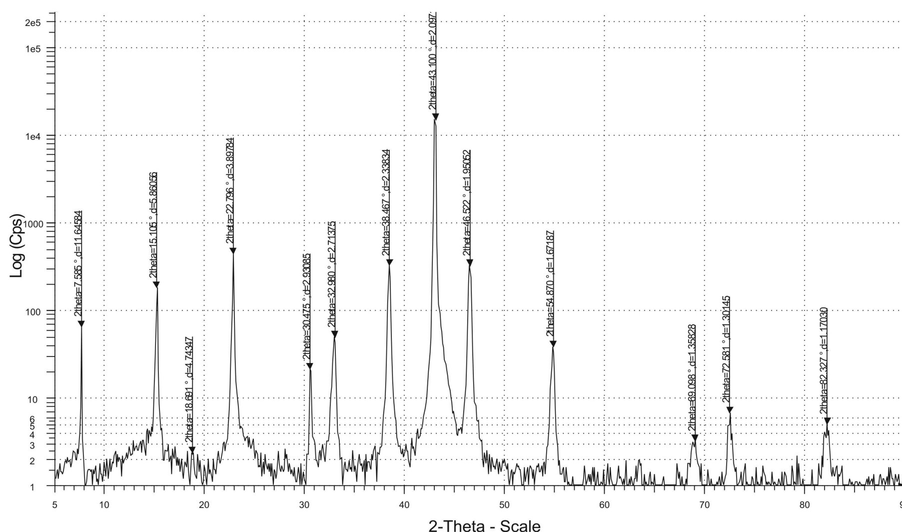

(a) X-Ray Diffraction Pattern

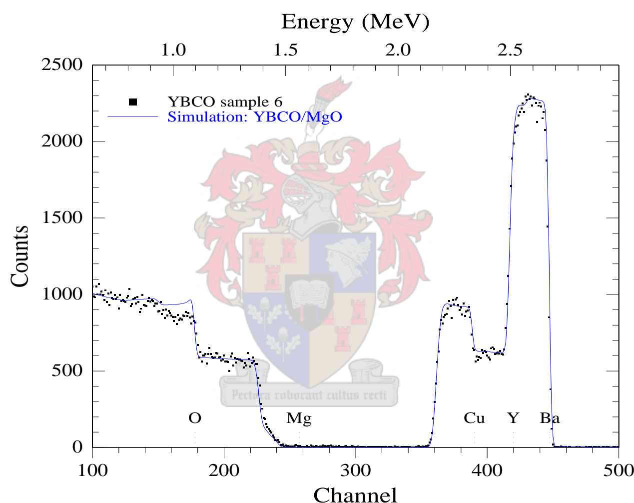

(b) RBS Channeling analysis

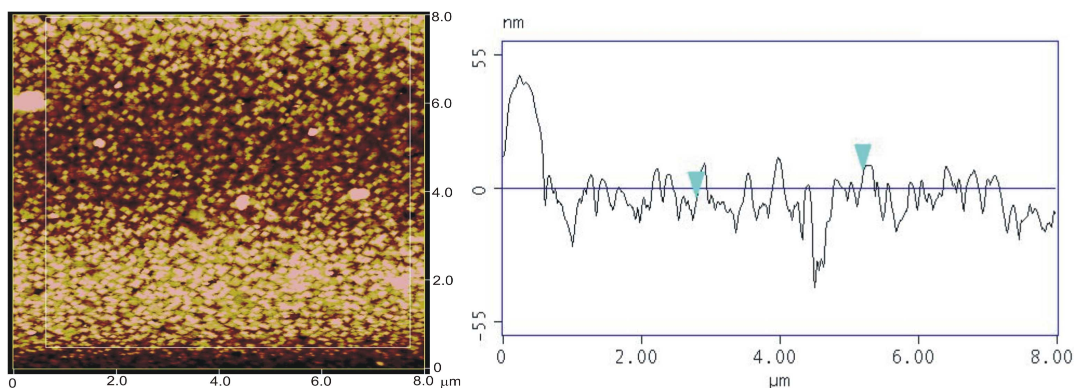

(c) AFM Surface Morphology profile

Figure 6.5: Growth Characterisation Measurements for an O_2:Ar ratio of 1:1

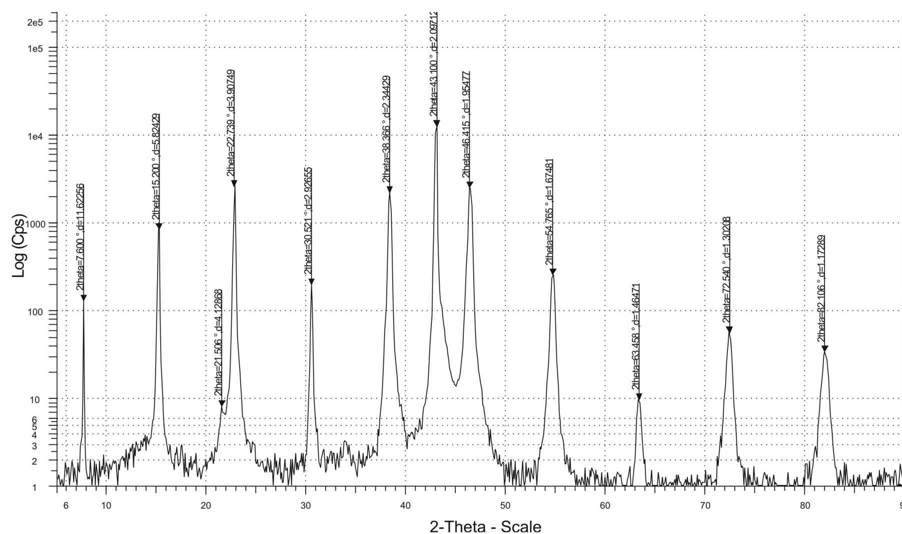

(a) X-Ray Diffraction Pattern

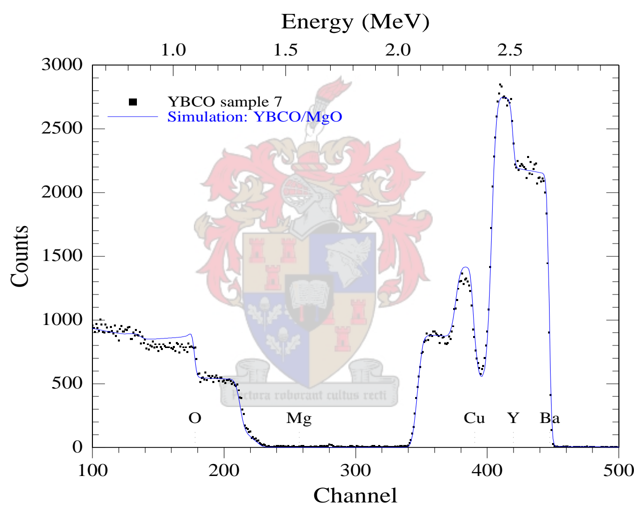

(b) RBS Channeling analysis

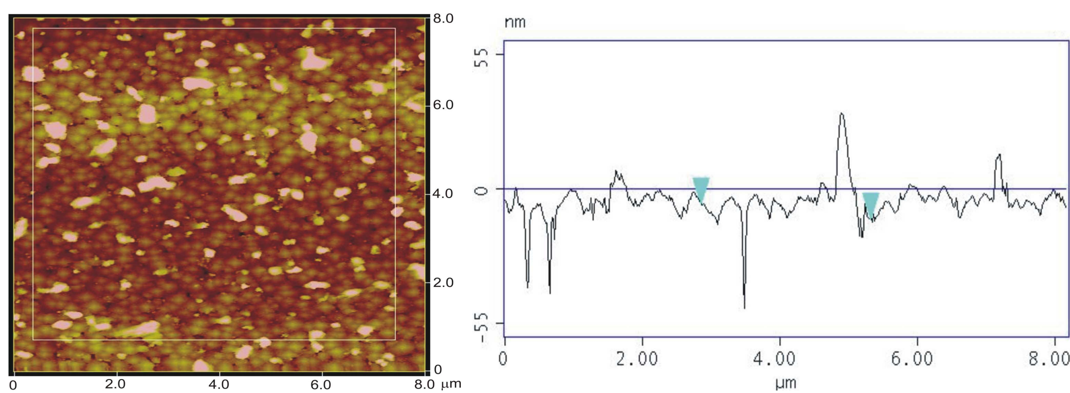

(c) AFM Surface Morphology profile

Figure 6.6: Growth Characterisation Measurements for an O_2:Ar ratio of 2:1

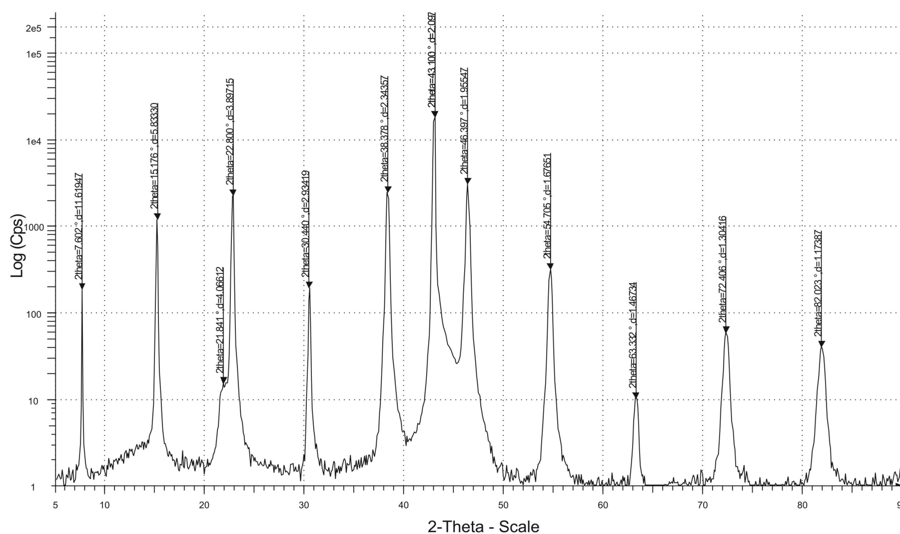

(a) X-Ray Diffraction Pattern

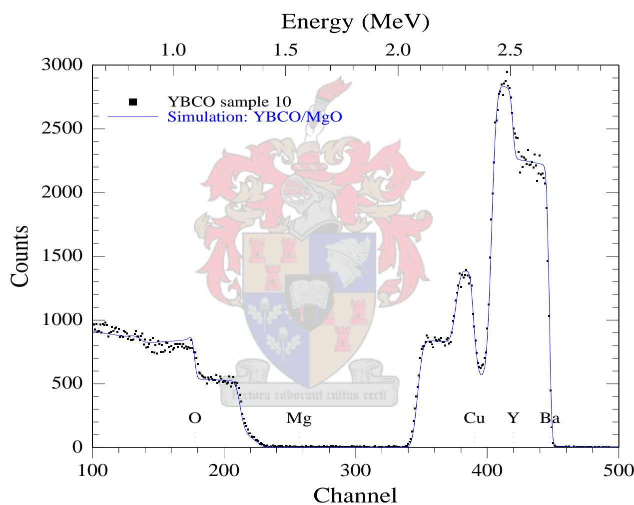

(b) RBS Channeling analysis

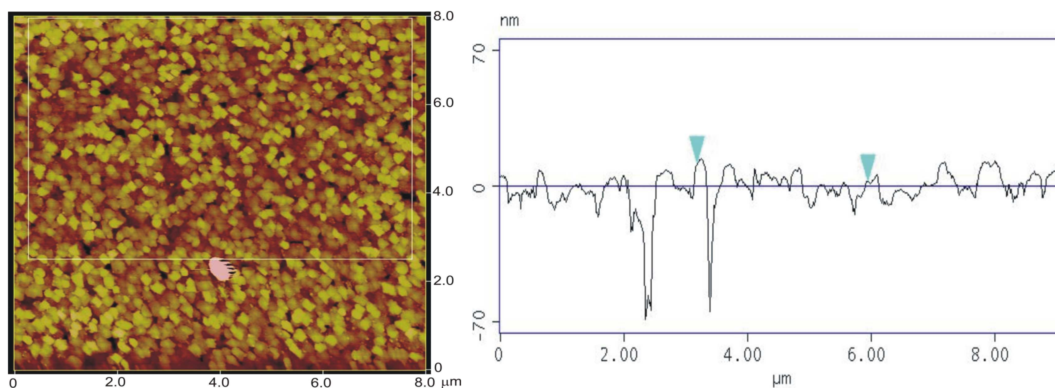

(c) AFM Surface Morphology profile

Figure 6.7: Growth Characterisation Measurements for an O_2:Ar ratio of 4:1

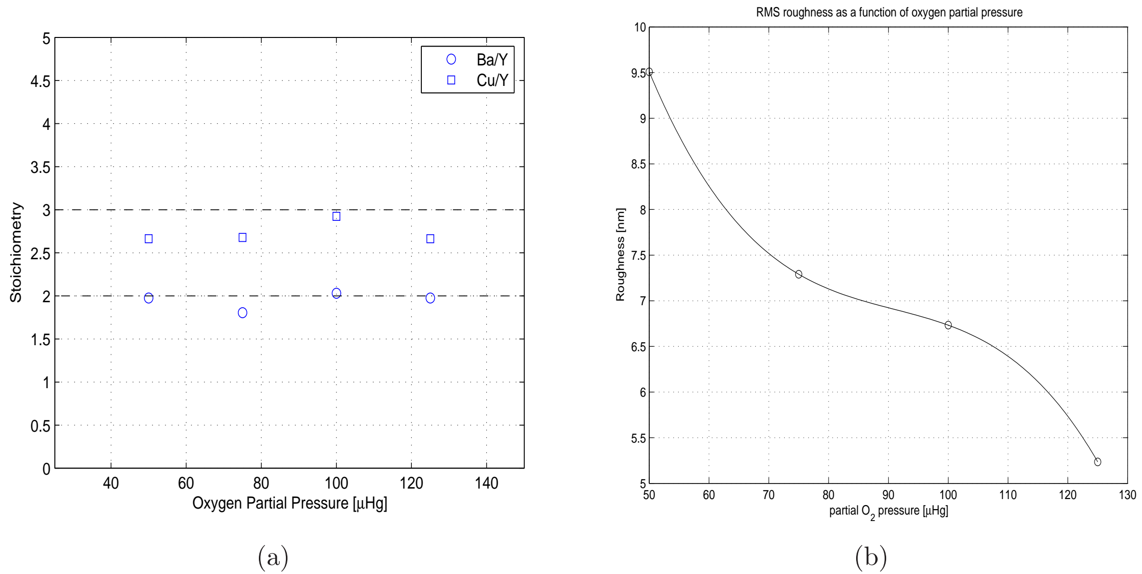

(a) (b)

Figure 6.8: (a) Stoichiometry and (b) RMS Roughness as a function of oxygen partial pressure

O_2:Ar	Deposition Rate [nm/min]
2:1	3.04
1:1	3.12
1:2	4.64
1:4	4.56

Table 6.1: Deposition rates for varying O_2:Ar ratios

Pectora roborant cultus recti

AFM analysis illustrate very smooth surfaces approaching 5 nm rms roughness. An improvement in surface roughness is observed as oxygen partial pressure is increased. This can again in part be explained by the lower arc voltages corresponding to this operating region suppressing the negative ion effect. The presence of outgrowths (possibly Cu-rich particles) is also very prominent at lower oxygen partial pressures. The grain sizes vary quite randomly for the different conditions, but in all cases, 3D island growth is prevalent.

6.6.1.2 Electrical Characterisation

To characterise the superconducting properties of the films, susceptibility measurements were performed (see Fig. 6.9). These measurements reinforced the results of the RBS analysis. The optimal oxygen/argon ratio is achieved at $P_{O_2} = 100\ \mu mHg$. This coincides with a critical temperature of 87.2 K and a ΔT of only 0.6 K (compare to reported values for T_c using DC sputtering of between 87-89 K). In Fig. 6.9(a), for low oxygen partial

pressure, the critical temperature drops below 45 K with a ΔT of 10 K.

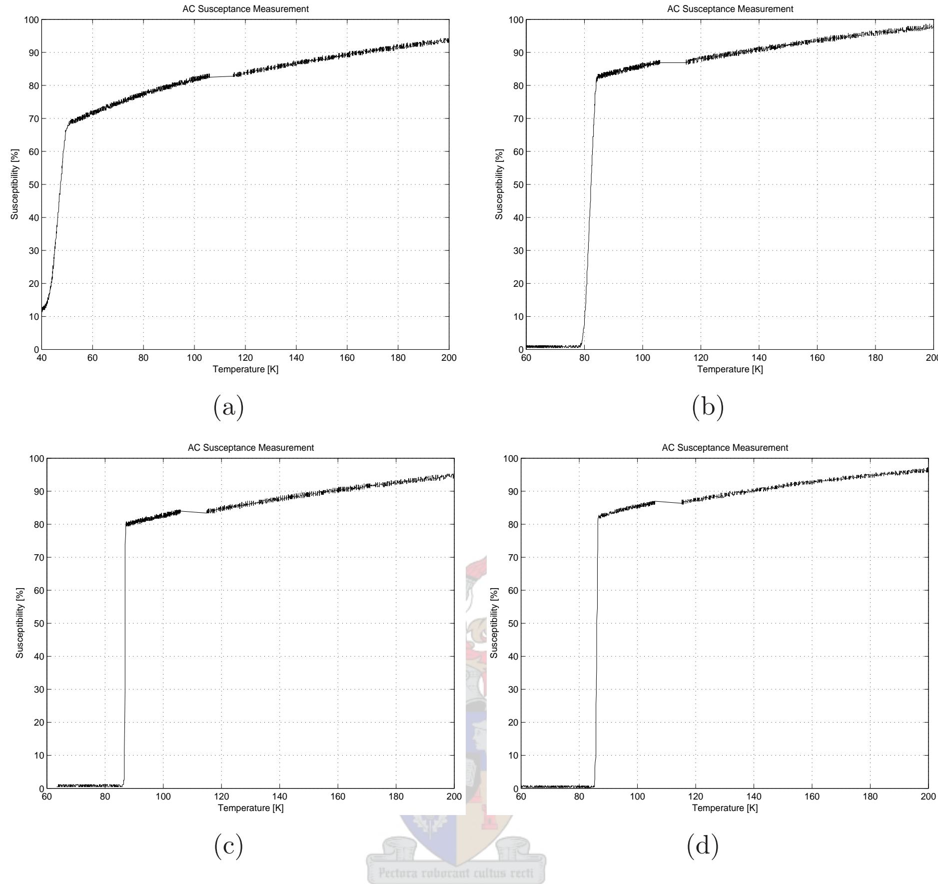

Figure 6.9: Susceptibility Tests for Oxygen/Argon ratios of (a) 1:2 (b) 1:1 (c) 2:1 and (d) 4:1 at a constant total pressure of 150 μmHg

O_2:Ar Ratio	T_c [K]	ΔT [K]
1:2	43.5	10
1:1	82.8	5
2:1	87.2	0.6
4:1	86.7	1.2

Table 6.2: Superconducting properties for varying O_2:Ar ratios

From the analysis shown above, the optimal oxygen/argon ratio was found to be 2:1, and was kept fixed for following experiments.

6.6.2 Total Pressure Variation

Having established a suitable argon/oxygen gas ratio, the next step was to vary the total pressure while keeping the partial pressure ratio and substrate temperature constant. Two additional experiments were conducted at higher total pressures of 225 μmHg and 300 μmHg. with a 2:1 oxygen/argon ratio at 740°C. Due to arcing problems and failure to obtain a sustainable plasma at pressures lower than 150 μmHg, no datapoints in the very low pressure range could be gathered. By increasing the total pressure, the deposition time is expected to increase and thermalisation is expected to play a more dominating role.

6.6.2.1 Growth Characterisation (Figs. 6.10 - 6.12)

The XRD scans depict the presence of the sharp (00l) peaks without any significant secondary phase peaks (from Fig. 6.11(a) a very small impurity peak is visible at 21.5^o but negligible). The measured c-axis lattice constants also correspond to good oxygenation. From RBS analysis the loss of Ba from the film surface is again present except for the sample deposited at 225 μmHg (see Fig. 6.10(b)). The compositional ratio of Y:Ba:Cu, as shown in Fig. 6.12(a), signify good stoichiometry at lower pressures. A noteworthy Ba deficiency is, however, present at high pressures. The deposition rates, as calculated from RBS analysis, showed the expected decrease in deposition rate with increasing pressure. The AFM study showed a decrease in average grain size as pressure was increased. The grain orientation also becomes more random corresponding to a decrease in film density. A possible explanation is that the arrival angles of impinging species are greater at the substrate surface for increased pressure due to the effect of thermalisation. This will result in a reduction of grain density and size due to geometric shadowing effects and low adatom mobility. From Fig 6.12(b), the best surface roughness is obtained at 225 μmHg.

Pectora roborant cultus recti

6.6.2.2 Electrical Characterisation

Susceptibility tests revealed that the critical temperature remained reasonably constant over the tested pressure range (Fig. 6.4). The only parameter that was affected, was the transition temperature width, ΔT, which became reasonably large at high pressure (5 K). An additional experiment was conducted only to confirm the deterioration of superconducting properties with increased pressure. The experiment, conducted at 375 μmHg, yielded a T_c of 78.5 K and ΔT of 14 K.

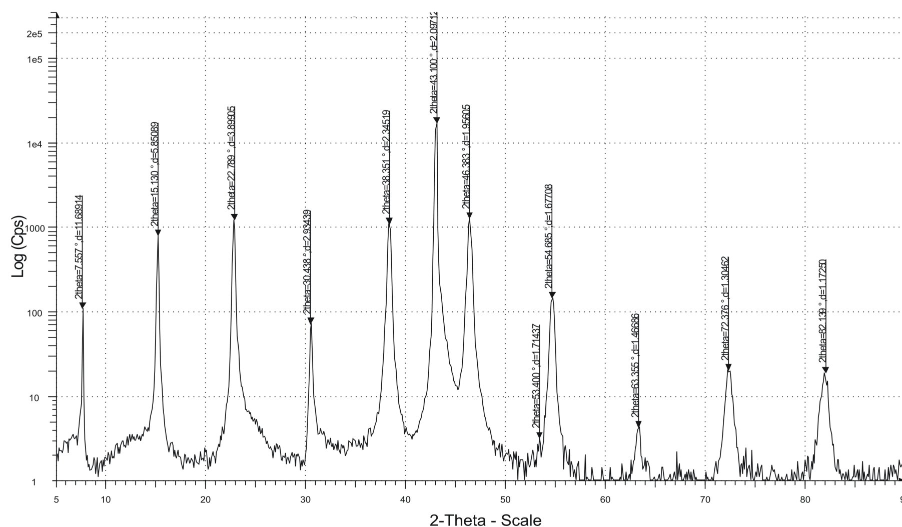

(a) X-Ray Diffraction Pattern

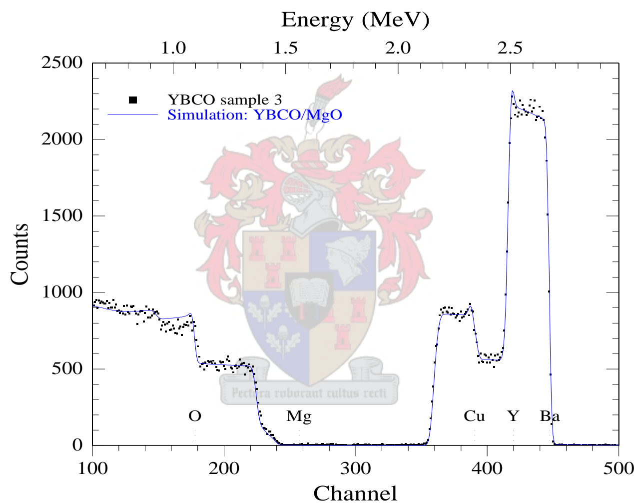

(b) RBS Channeling analysis

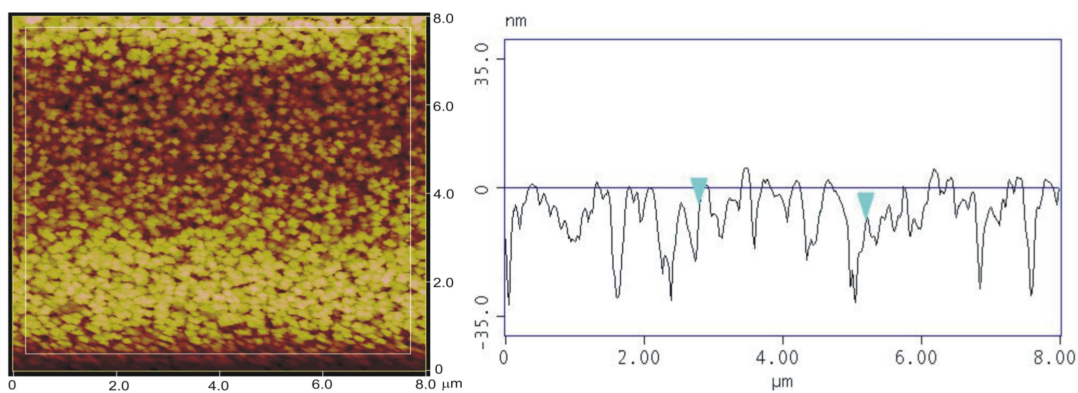

(c) AFM Surface Morphology profile

Figure 6.10: Growth Characterisation Measurements for a Total Pressure of 225 μmHg

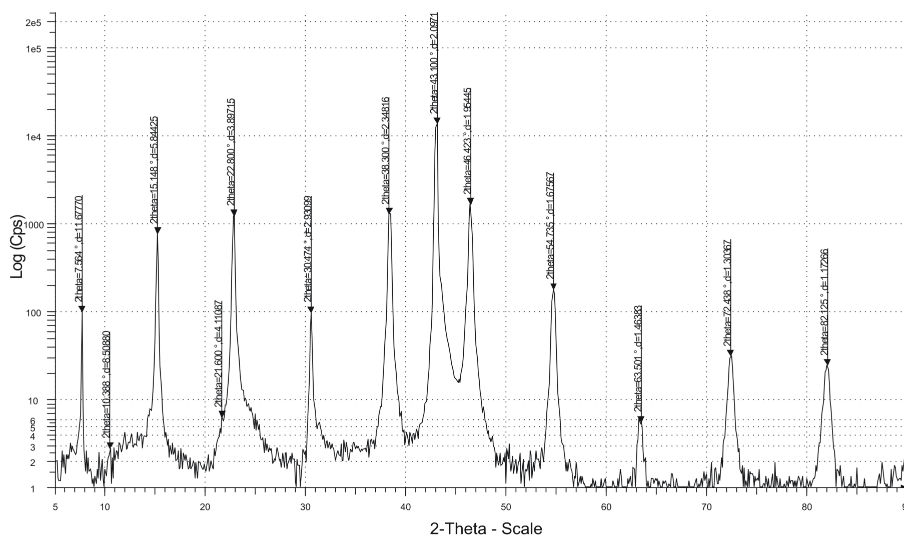

(a) X-Ray Diffraction Pattern

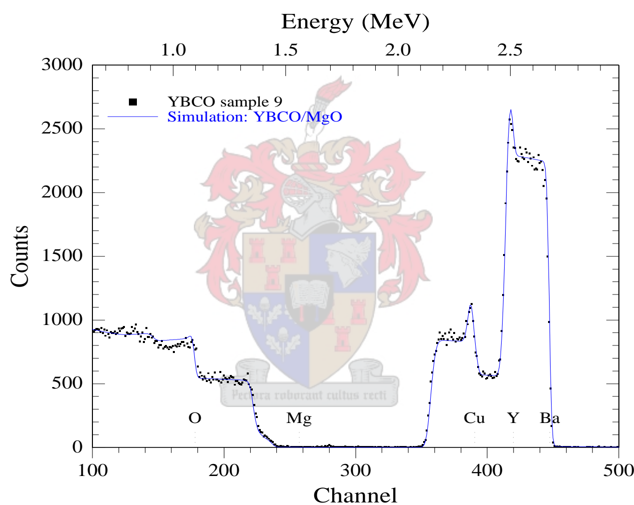

(b) RBS Channeling analysis

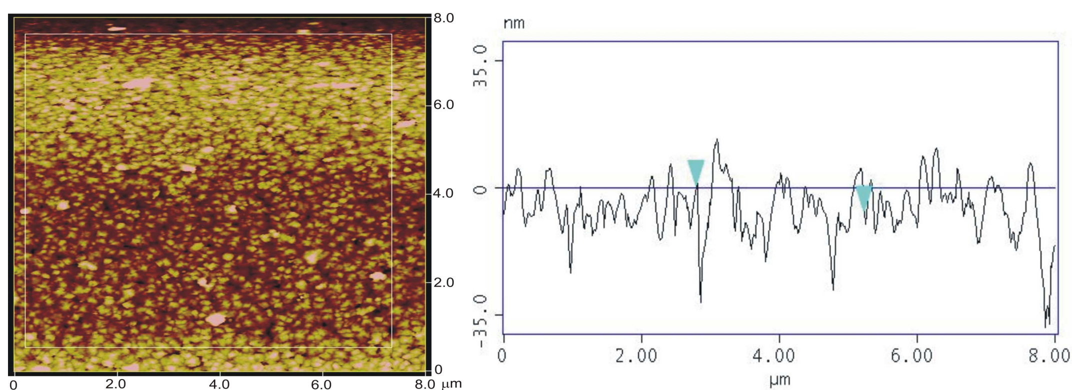

(c) AFM Surface Morphology profile

Figure 6.11: Growth Characterisation Measurements for a Total Pressure of 300 μmHg

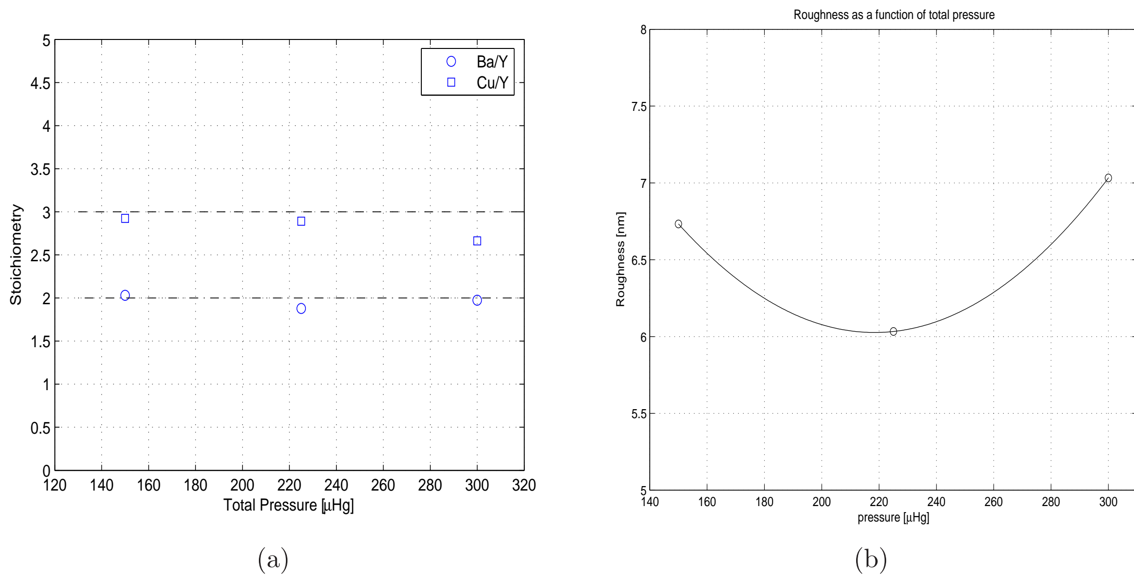

Figure 6.12: (a) Stoichiometry and (b) RMS Roughness as a function of total pressure

P_{TOT} [μmHg]	Deposition Rate [nm/min]
150	4.64
225	2.89
300	2.33

Pectora roborant cultus recti

Table 6.3: Deposition rates for varying total pressure

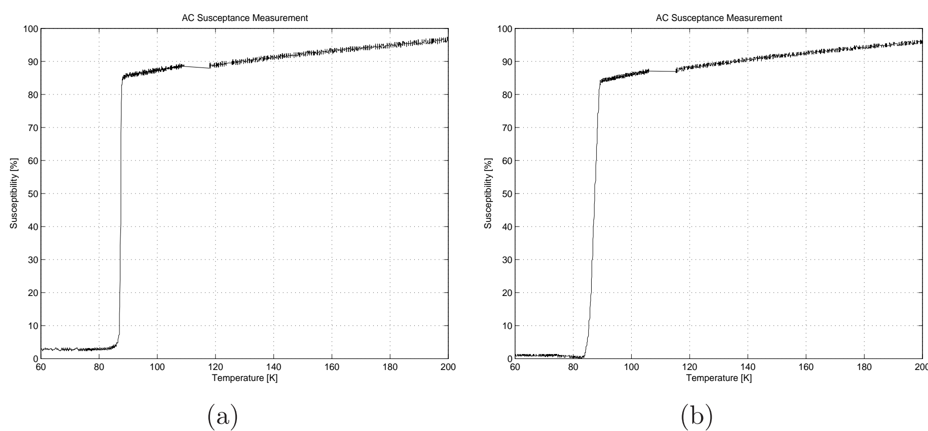

Figure 6.13: Susceptibility tests for varying total pressures of (a) 225 μmHg and (b) 300 μmHg

P_{TOT} [μmHg]	T_c [K]	ΔT [K]
150	87.2	0.6
225	87.6	0.7
300	87.4	5

Table 6.4: Superconducting properties for varying total pressure

From these results, it was decided to fix the total pressure to 225 μmHg for further experiments.

6.6.3 Substrate Temperature Variation

Finally, after having established a suitable argon/oxygen gas ratio at a desired total pressure, the influence of temperature variation on the film quality was investigated. In literature, typical substrate temperatures range between 650-800^oC to produce high quality superconducting films. Accordingly, five experiments were conducted with a minimum temperature of 680°C and a maximum of 760°C in 20°C steps (maximum obtainable heater temperature was around 770°C).

6.6.3.1 Growth Characterisation (Figs. 6.14 - 6.18)

The XRD scans again illustrate the presence of the sharp and well-defined (00l) peaks corresponding to orthorhombic YBCO. At low temperatures, as seen in Figs. 6.14(c) and 6.15(c), unwanted peaks are present corresponding to (103) growth orientation. This peak disappears for substrate temperatures above 720°C. It can thus be concluded that crystallinity is excellent for the higher range of substrate temperatures. The c-axis lattice parameters all correspond to values less than the accepted crystal constant of 1.1680 nm for $YBa_2Cu_3O_7$ indicating good oxygenation of the film.

The RBS analysis reveal that the stoichiometry remains reasonably constant over the temperature spectrum (see Fig. 6.18) except for the Cu and Ba deficiency at 680°C. The thicknesses of the deposited films were also determined from the analysis. These results are summarised in Table 6.5. From this data it is clear that the deposition rate decreases with increasing substrate temperature.

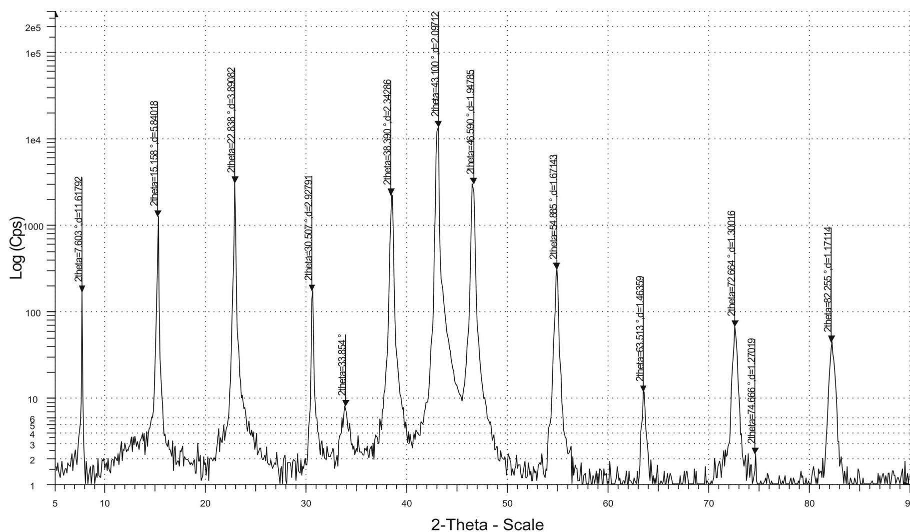

(a) X-Ray Diffraction Pattern

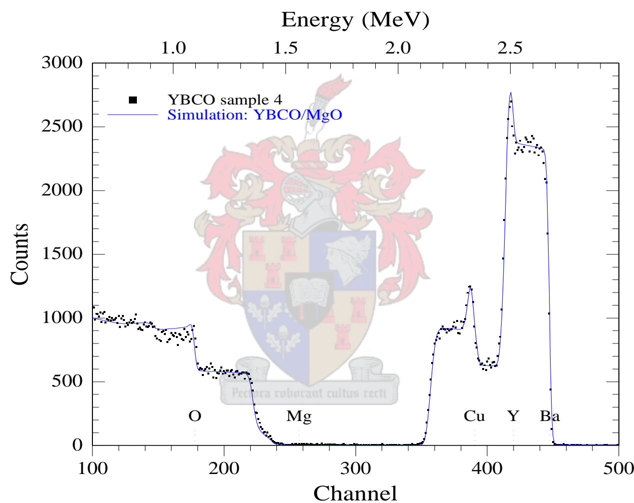

(b) RBS Channeling analysis

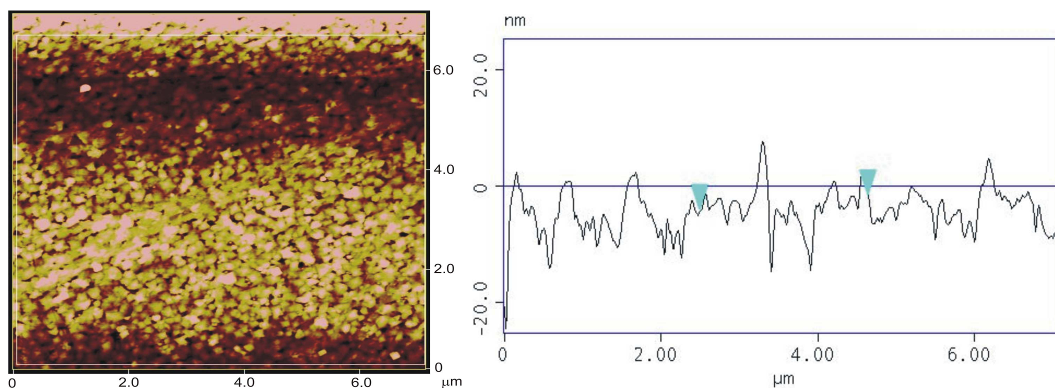

(c) AFM Surface Morphology profile

Figure 6.14: Growth Characterisation Measurements for a Substrate Temperature of 680°C

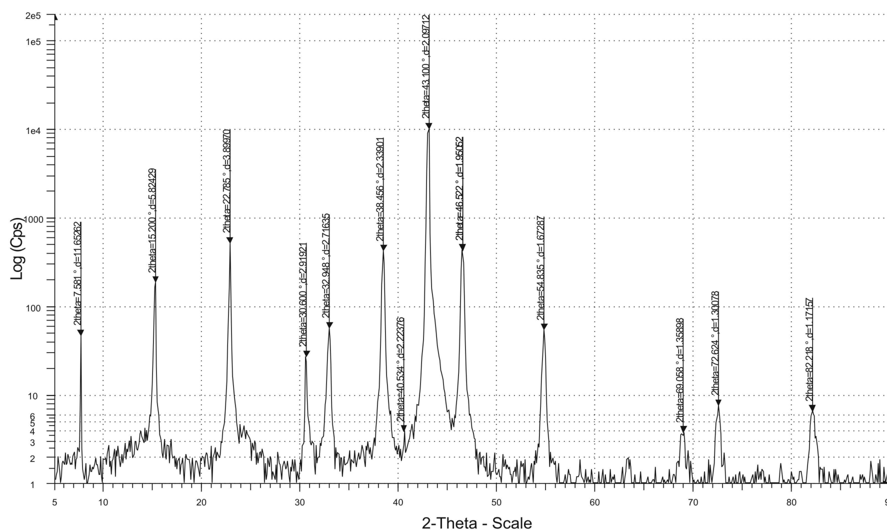

(a) X-Ray Diffraction Pattern

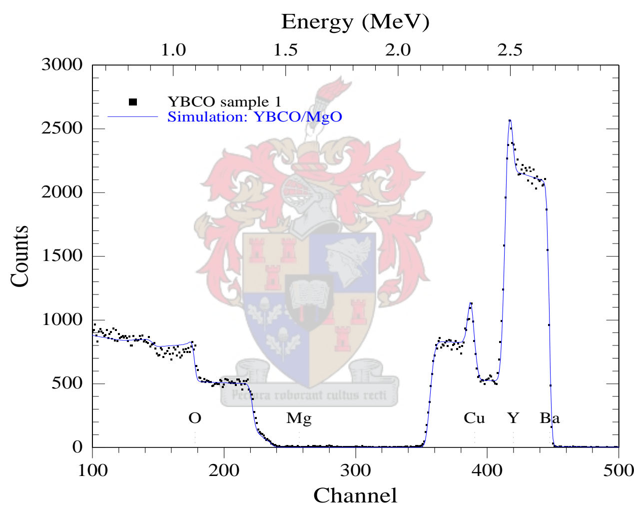

(b) RBS Channeling analysis

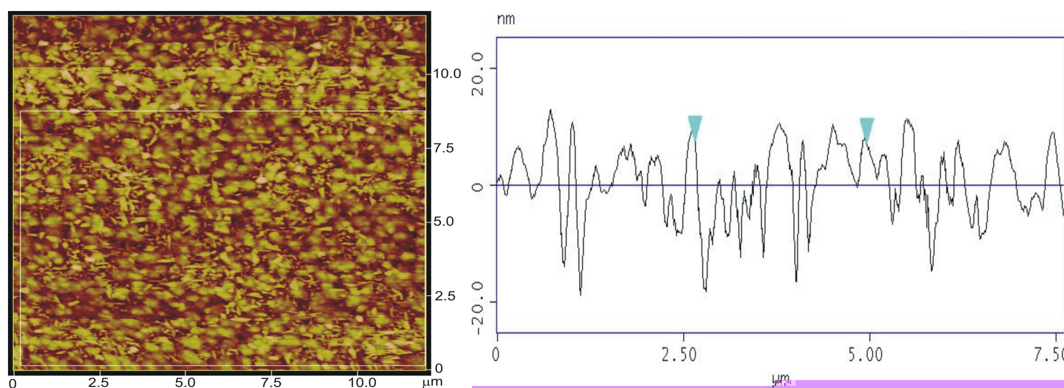

(c) AFM Surface Morphology profile

Figure 6.15: Growth Characterisation Measurements for a Substrate Temperature of 700°C

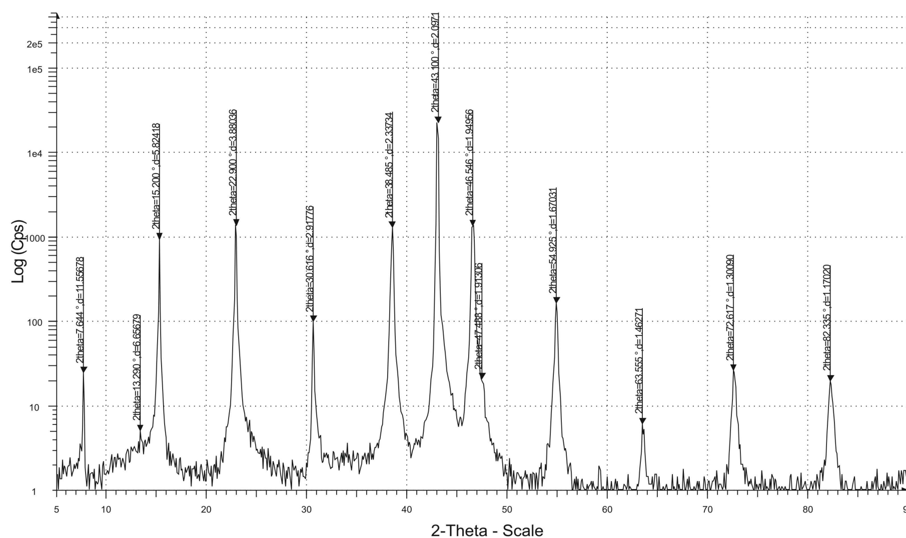

(a) X-Ray Diffraction Pattern

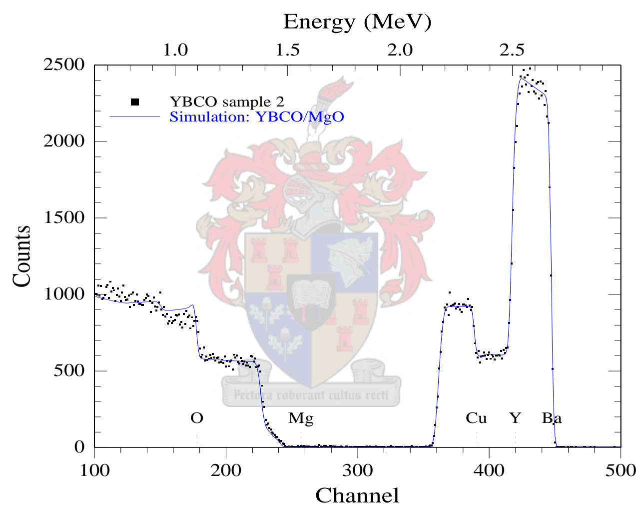

(b) RBS Channeling analysis

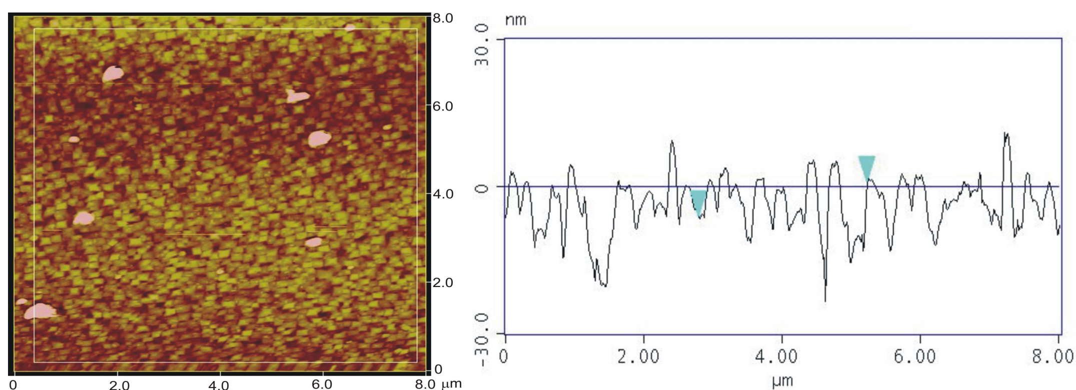

(c) AFM Surface Morphology profile

Figure 6.16: Growth Characterisation Measurements for a Substrate Temperature of 720°C

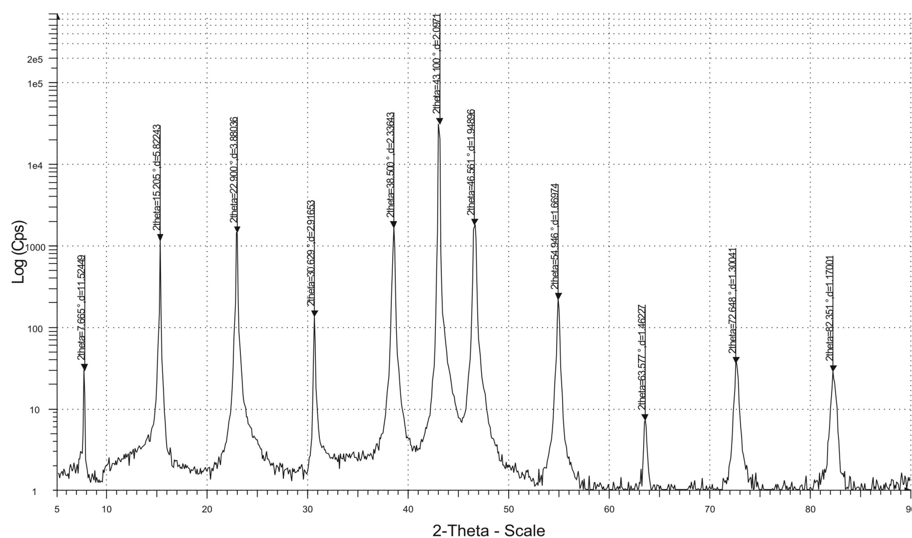

(a) X-Ray Diffraction Pattern

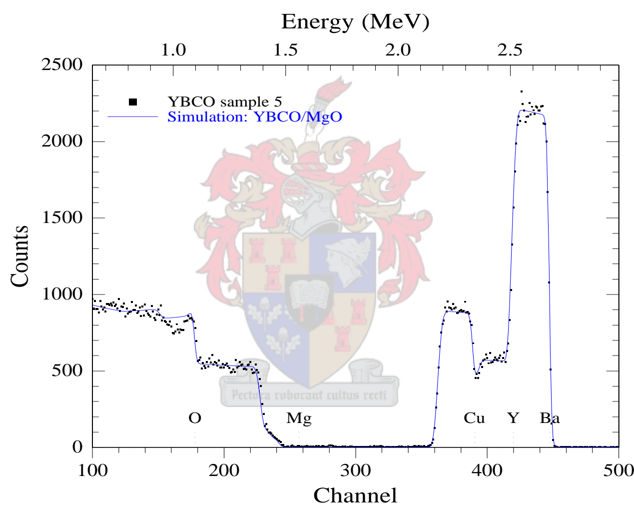

(b) RBS Channeling analysis

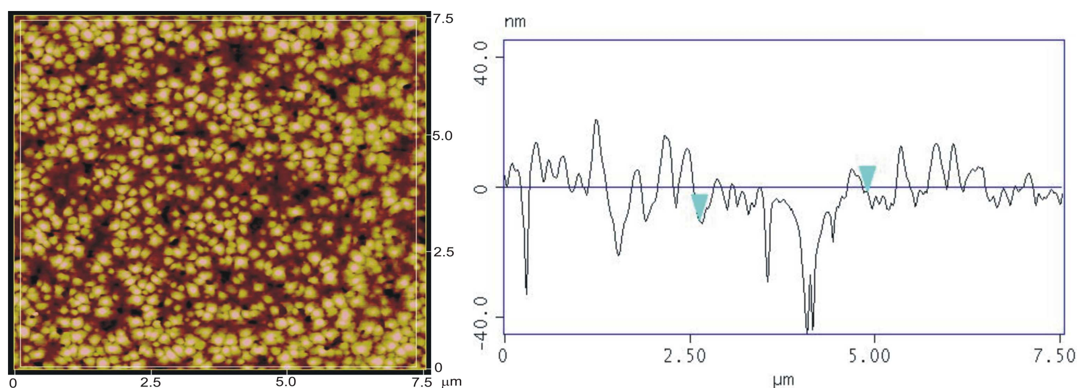

(c) AFM Surface Morphology profile

Figure 6.17: Growth Characterisation Measurements for a Substrate Temperature of 760°C

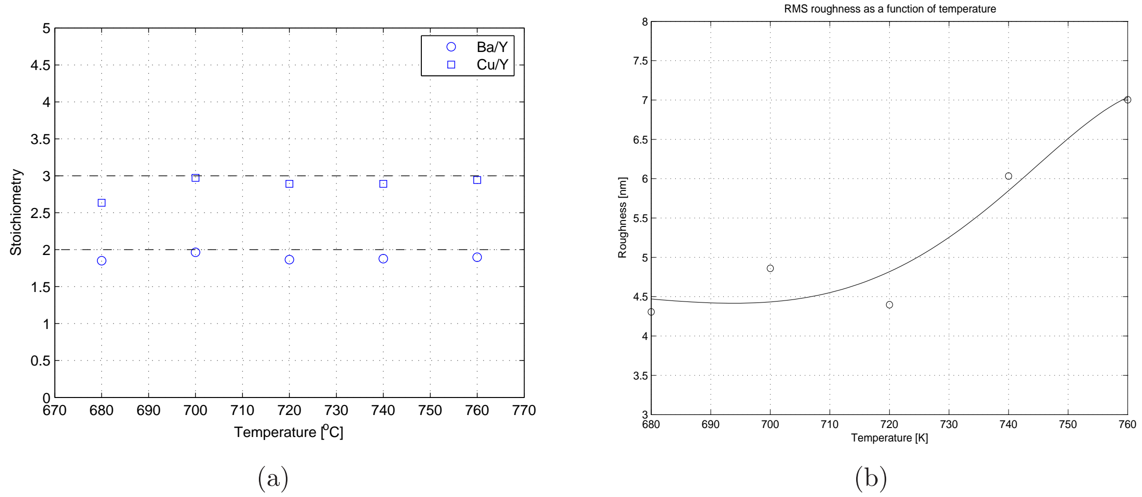

(a) (b)

Figure 6.18: (a) Stoichiometry and (b) RMS Roughness as a function of substrate temperature

T_{dep} $[^oC]$	Deposition Rate [nm/min]
680	3.15
700	3.15
720	2.70
740	2.89
760	2.63

Table 6.5: Deposition rates for varying substrate temperature

The AFM analysis (Fig. 6.18(b)) shows that the film surface demonstrates better roughness at lower substrate temperatures. Better in-plane alignment of grains at 720°C and 740°C reflects more textured and dense growth. It is also apparent that the surface are not characterised by numerous outgrowths as was the case for the lower total pressures. Higher temperatures (see Fig. 6.17(c)), on the other hand, started to reveal pitting coinciding with the rougher measured surface. This is slightly unexpected from pure kinetic considerations whereby higher surface energy should lead to denser films. The growth mode was identified as 3D island growth in all cases. The grain sizes of the film remained in the order of 150-200 nm over the temperature range. Thus, from a growth perspective, it can be concluded that temperature mostly influenced surface morphology.

6.6.3.2 Electrical Characterisation

Susceptibility tests showed the highest critical temperature (87.6 K) is reached for T = 740°C. This value drops sharply for higher substrate temperatures. ΔT follows this pattern,

being best at 740°C (0.7 K), and increasing as temperature increases. A summary of the susceptibility tests is presented in Table 6.6.

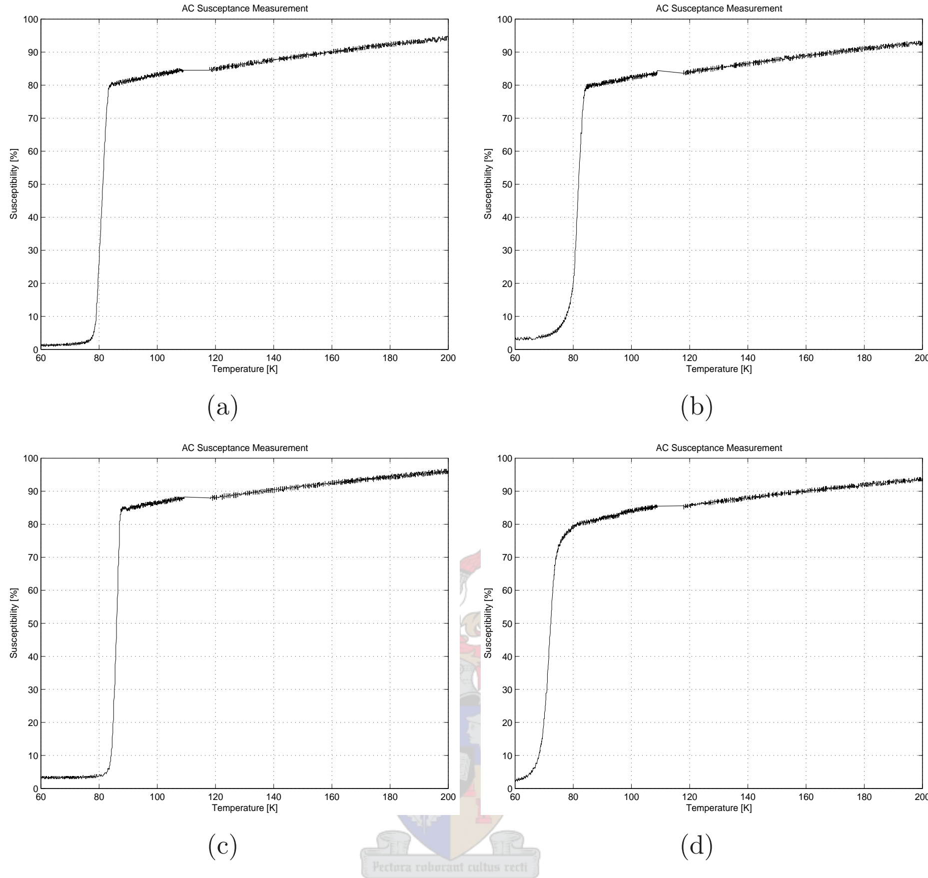

Figure 6.19: Susceptibility Tests for Temperature Variation with T_{dep} (a) 680°C, (b) 700°C, (c) 720°C and (d) 760°C

T_{dep} [^{o}C]	T_c [K]	ΔT [K]
680	81.75	5
700	82	7
720	86	4
740	87.6	0.7
760	72.5	10

Table 6.6: Superconducting properties for varying substrate temperature

6.6.4 Conclusion

The final optimised parameter set is presented in Table 6.7. The process provides a reproducible method to deposit high quality YBCO thin films with excellent growth characteristics (surface roughnesses of 4 nm are comparable to commercial standards) and excellent superconducting properties ($T_c > 87$ K and $\Delta T = 0.7$ K). This makes the sputtered films suitable for application in multilayer circuits or in microwave applications. It also provides a significant improvement to the 200 nm roughness films previously (pre-2006) deposited with PLD with similar superconducting properties.

Parameter	Value
T_{dep}	740^oC
P_{Ar}:P_{O_2}	1:2
P_{TOT}	225 μmHg
Deposition Rate	2.89 nm/min

Table 6.7: Optimal parameter set for YBCO deposition with ICM

Pectora roborant cultus recti

6.7 Chapter Overview

This chapter discussed four characterisation techniques to analyse thin film growth and electrical properties. These techniques were then used to aid in the optimisation process of YBCO thin films deposited by the new Inverted Cylindrical Magnetron system. The optimised films demonstrated excellent quality comparable to commercial standards.

Chapter 7

Buffered Step-edge Josephson Junctions

There are several Josephson junction topologies available, each with inherent production difficulties and performance limitations. Step-edge junctions (SEJs) are an attractive option since it offers topological freedom that is desired in the design and integration of small and large scale electronic circuits. SEJs are physically manifested as the epitaxial growth of a high-T_c thin film on a step edge, etched into a substrate prior to film deposition. The most important requirement in the preparation of an SEJ is the realisation of a well-defined step profile. This in itself provides several fabrication challenges.

This chapter will briefly present the microstructural theory behind the step-edge junction. This will be followed by a systematic study into the production of these junctions.

7.1 Underlying Mechanisms in Step-Edge Junction Formation

To fabricate reproducible step-edge junctions (SEJs), it is necessary to understand the mechanisms which lead to the nucleation of grain boundaries on stepped substrates. A direct correlation exists between the YBCO growth characteristics and the microstructure of the step. The microstructure of the step-edge is dependant on the substrate material, the step angle and the step profile.

7.1.1 Step-Edge Junctions on Perovskite Substrates

The crystal structures of perovskite substrates such as $LaAlO_3$, $SrTiO_3$, and $NdGaO_3$ demonstrate a remarkable similarity to oxide-based HTS such as YBCO. The resulting low lattice mismatches allow for epitaxial growth of the thin film with excellent superconducting properties [45]. When a step-edge is now introduced in a (100) perovskite substrate, the YBCO nucleation is not necessarily [001]|||[001]. As soon as the step angle approaches 45°, (103) YBCO domains will form on the step-edge. For a step angle $\omega > 45^o$, a situation similar to that illustrated in Fig.7.1 is expected. In such a case, two 90° tilt symmetric grain boundaries (SGBs) nucleate at the defined edges of the step and a combination of 90° symmetric and basal-plane-faced (BPF) tilt GBs form on the step surface [46].

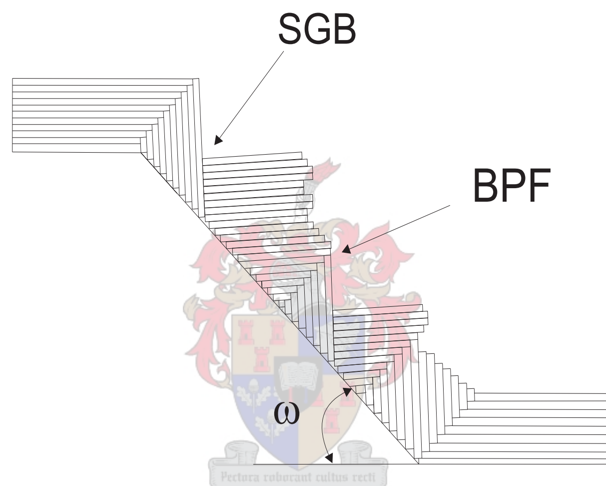

Figure 7.1: Grain boundary formation on a perovskite substrate with a 45° step-edge

7.1.2 Step-edge Junctions on Non-perovskite Substrates

On non-perovskite substrates such as MgO, the substrate lattice is not a template for YBCO growth. As a result the growth orientation which minimises the free energy at the interface with the substrate is dominant. Accordingly, an YBCO thin film will preferentially grow by aligning its c-axis with the normal of the macroscopic surface of the substrate [47]. In the presence of a step-edge, film nucleation would thus occur as illustrated in Fig. 7.2. If the step-edge is well defined and not rounded, even small step angles may introduce [100] and [010] tilt grain boundaries at the top and bottom of the step-edge [13]. The bottom grain boundary can, however, disappear as the step angle becomes too shallow (usually around 20°). Given the microstructural growth of the deposited film, it becomes possible

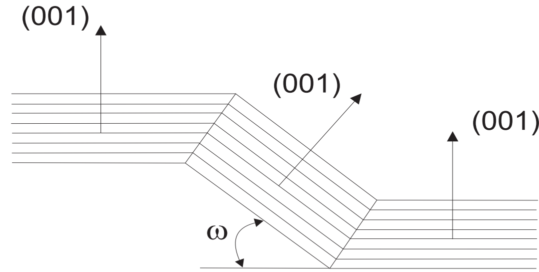

Figure 7.2: Typical grain boundary formation on a non-perovskite substrate step-edge

to alter the grain boundary structure by simply changing the step angle. The range of step angles used for MgO substrates typically varies from 10-45°. In analogy with bicrystal junctions, the critical current density, J_c, has a tendency to decrease as the step angle (and so the grain boundary angle) increases [48].

7.2 General Properties of Step-Edge Junctions

Despite the contrasting growth mechanisms on steps of different substrate materials, it is still possible to identify some general characteristics [13]:

- Electromagnetically small junctions ($\frac{w}{\lambda_J} < 4$, where w is the geometrical width and λ_J is the Josephson penetration depth) demonstrate IV-characteristics typical of a resistively and capacitively shunted junction model (RCSJ)).
- As the ratio $\frac{w}{\lambda_J}$ increases, the IV-characteristics exhibit an increasing amount of excess current which is consistent with a transition into the long junction operating region.
- Step-edge junctions are generally overdamped ($\beta_c < 1$).
- The characteristic voltage $V_c = I_c R_N$ lies in the range of 1 mV. Typically: $V_c(T = 4.2K) < 5$ mV and $V_c(T = 77K) < 0.5$ mV.
- V_c generally scales with J_c.

Pectora roborant cultus recti

7.3 History of Step-edge Fabrication at Stellenbosch

Due to the cost involved in buying Josephson junctions commercially, it was decided to explore the possibility of establishing an in-house process. Step-edge junction fabrication was first attempted at the University of Stellenbosch by L.H. Snetler in 2004 [1]. At that stage, the prospect of manufacturing a working Josephson junction seemed nearly impossible. Several problems were presented, but no immediate solutions could be offered. Amongst these problems, the profile of the protective mask was seen as the major cause for the failure to produce a working junction structure.

During the course of this research, several process improvements were made to lay the foundation for step-edge research. Major improvements to the dry etching process, as well as significant improvements to the profile of the protective mask, created the illusion that the rest of the fabrication process would be a mere formality. This was indeed only an illusion. An in-depth study of the fabrication process followed, revealing the true production problems and addressing them accordingly.

7.4 Step-edge Fabrication

Pectora roborant cultus recti

Step-edge fabrication is widely considered to be a very tricky process. Even very small variations in the fabrication procedure, which may look insignificant, may cause dramatic changes in the performances of the junctions. For this reason, the fabrication process was analysed systematically.

The fabrication process of SEJs was divided into five stages:

1. Step patterning: Photolithography and Ion Milling
2. Step Annealing
3. Thin film deposition
4. Circuit patterning: Photolithography and Ion Milling
5. Establishing electrical contact: Deposition of gold pads and wire bonding

7.5 Step Patterning

The properties of SEJs are strongly dependent on the microstructure of the etched step. For this reason, the study and characterisation of the step patterning process are critical to ensure the realisation of a reproducible fabrication process. Accordingly, significant effort was directed to this stage of the process.

Etching of the desired step profile was accomplished through a dry etching technique. A few reports of wet etching being successfully used to etch oxide substrates do exist, but were found to be non-reproducible. Ion milling promises more control of the etching process and can produce uniform step profiles provided that the etching conditions are optimised correctly. Several etching requirements must be met to attain the desired step profile.

The first requirement is a smooth and homogeneous step profile. The epitaxial template of the step must be of the same quality as the rest of the substrate to prevent the formation of additional grain boundaries or the growth of a-axis oriented YBCO [49]. Experiments done on the Ion Mill system (see Chapter 4) showed that the surface damage introduced by the etching process is minor (provided ion energies are kept at acceptable levels).
The occurrence of redeposition during the etch process is, however, a major concern and should be minimised as far as possible. Redeposition can inhibit the epitaxial growth of the superconducting thin film as it is amorphous. A means to eliminate this redeposited material, is to perform a second milling procedure. This procedure is done at a sharp incident beam angle and serves to polish the surface, removing the softer redeposited material. Finally, and most important, is the attainment of a suitable step angle that will ultimately result in the formation of a grain boundary. To address the requirement of attaining a suitable step profile, a theoretical model for the dry etching process was derived. Such a model will provide a better understanding of the major contributing factors in the step patterning process.

7.5.1 Model for Step Angle Determination

In our model (adapted from a model proposed by Wu et al [49]), we shall define two main variables describing the orientation of the substrate during the etch process (as shown in From Fig. 7.3(a),(b)).

- α: Incident ion-beam angle measured relative to the substrate normal.

- β: Substrate rotational angle.

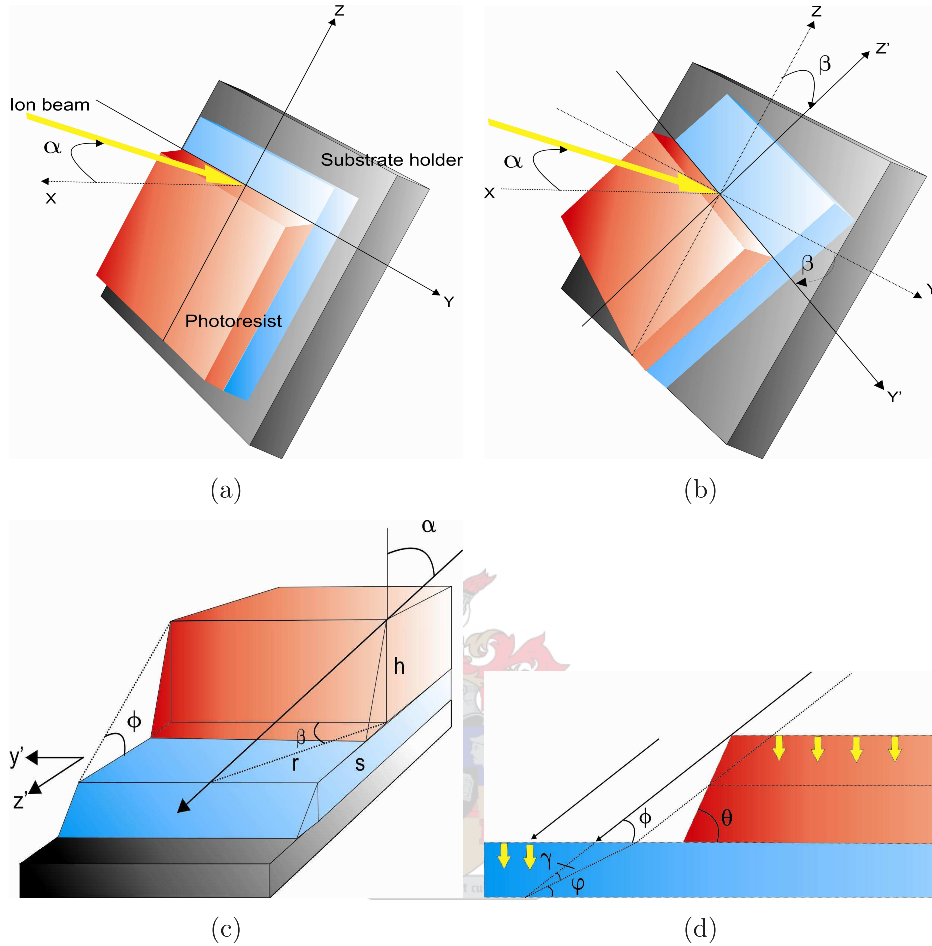

(a) (b) (c) (d)

Figure 7.3: Model of step-edge process

These two angles can now be used to define a so-called shading/shadow angle, ϕ, referring to the angle at which the ion beam impinges on the substrate. In our model, the shading angle should be less than the sidewall angle of the photoresist step, θ. If this condition is not met, significant redeposition and rounded step profiles could result. This is an acceptable requirement if we consider that photoresist angles of up to 70° are possible. To determine the shading angle we can draw a schematic such as shown in Fig: 7.3(c). By using simple geometric relations, we obtain that

$$tan(\phi) = \frac{h}{s} = \frac{h}{r}\frac{r}{s} = \frac{1}{tan(\alpha)sin(\beta)} \tag{7.5.1}$$

where h is the photoresist thickness, r is the projection of the ion-beam on the substrate surface and s is the projection of r on the y' axis.

To complete our model, we need to take into consideration the etch rates of the substrate and photoresist mask. The general scenario is illustrated in Fig: 7.3(d). It is clear that if the protective mask etch rate is too rapid, a larger region of substrate surface would be exposed to the ion beam (not shaded by the mask), resulting in poor step angles. It is for this reason that hard masks is critical for good step angles. By performing some geometric manipulations we obtain the governing equation:

$$\omega = arctan(\frac{1}{1+x} tan\phi) \tag{7.5.2}$$

where ω is the step angle and

$$x = \frac{mask\ etch\ rate}{substrate\ etch\ rate}. \tag{7.5.3}$$

7.5.2 Model Evaluation

Having derived a general model for our dry etching process, we can now determine the optimal operating region for our relevant materials. From the derived equations, it can be seen that the shading angle, ϕ, and the relative etch rate, x, play dominant roles in the resulting step angle. Intuitively, it makes sense that for our derived model a shading angle as close to the resist angle as possible would produce the best step-edge profile. Although this is true, it should be kept in mind that our model do not include the effect of redeposition. As will be shown, redeposition is most prominent for small values of β, corresponding to larger shading angles. We thus expect the practically obtained step-angles to deviate slightly from the model in this operating region.

Using (7.5.1), the shading angle, ϕ, dependence on the ion beam angle and substrate rotation can be illustrated graphically. This is shown in Fig. 7.4 where ϕ is plotted as a function of β for different ion beam angles.

It is well-known that oxide-based substrates possess slow etch rates. In this thesis MgO substrates and SPR700 photoresist were used for production. As mentioned, the relative etch rate between the substrate and protecting mask, plays a significant role in the re-

Pectora roborant cultus recti

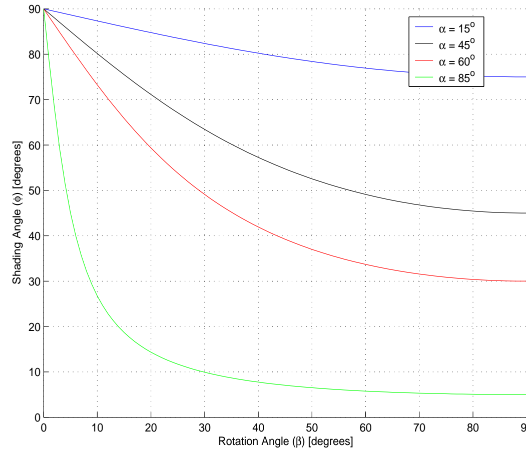

Figure 7.4: Shading angle as a function of β

sulting step angle. To characterise this component of the process, several step-edges were etched for different values of α while keeping the rotational angle, β, constant. This is done since the tilt angle of the substrate determines the angle at which the incident argon ions bombard the substrate and the protective mask (momentum transfer) corresponding to a specific etch rate.

After each etch run, an AFM step-height analysis was performed on the step-edge before and after removal of the protective mask. From this data the etch profiles for these two materials could be obtained as depicted in Fig 7.5. From these figures it can be seen that the etch rate of the resist is significantly higher compared to the MgO substrate over the entire etching domain. It is also clear that for both materials the etch rate is fastest at an ion-beam angle of around 60°. We are, however, more interested in the relative etch rates as required by our model. The relative etch rate profile (Fig. 7.6) reveals a minimum relative rate of $x = 9$ for a beam angle $\alpha = 30^o$.

Pectora roborant cultus recti

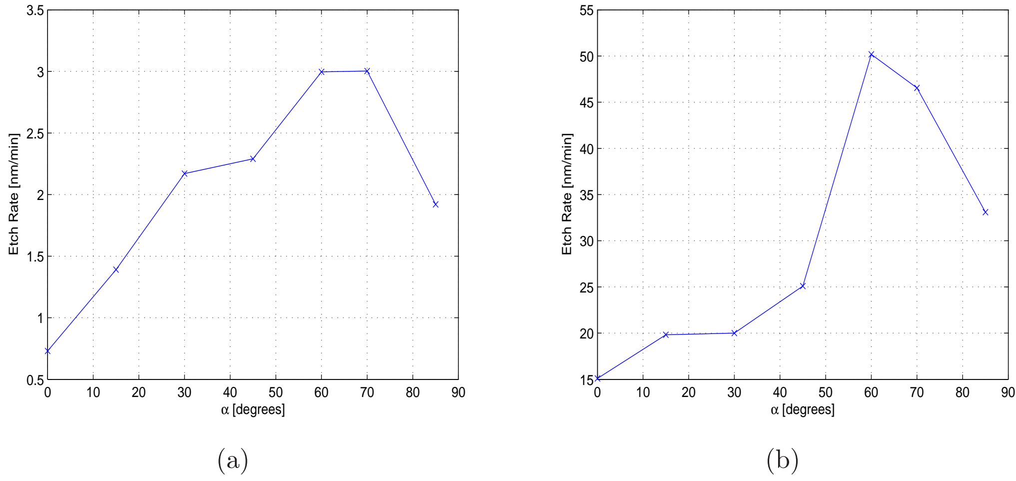

Figure 7.5: Etch rates of (a) MgO and (b) SPR700 photoresist as a function of beam angle

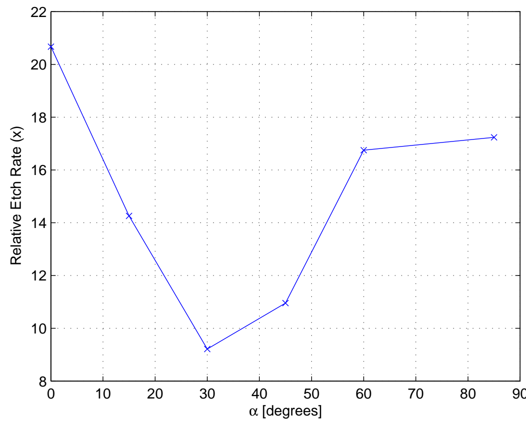

Figure 7.6: Relative etch rates as a function of ion-beam angle

Having calculated the etch rates, we can finally consider the theoretically realisable step angles. Fig 7.7 illustrates the predicted step angles as a function of the shading angle for a given α (and corresponding x). A critical problem is now evident. According to the model, all step angles corresponding to shading angles smaller than 70°, would be less than 15°. Shading angles exceeding this value lead to significant redeposition effects and rounded edge profiles. Considering the fact that a step angle of at least 10° without rounding effects is required to realise a JJ, it is clear that reproducibility would be questionable. Selectivity seems to be the deciding factor why reasonable step-edge angles could not be obtained in the past. Before taking any drastic steps, it was, however, necessary to validate

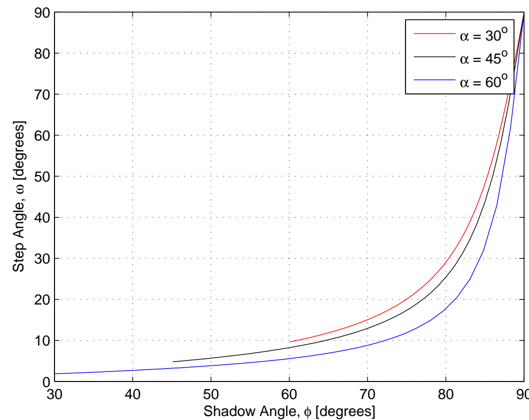

Figure 7.7: Step angle as a function of shading angle

the proposed model to confirm this problem.

7.5.3 Model Validation

To validate our proposed model, it was decided to conduct several etch runs at a constant ion beam incident angle, α and a variable rotational angle β. To produce reasonable step-edges, we want to minimise x, corresponding to $\alpha = 30^o$. For this tilt angle, the shading angle exceeds 70° for a wide range of substrate rotation angles. To compromise in this respect, it was decided to conduct the experiments at a tilt angle of $\alpha = 45^o$ providing a reasonable relative etch rate and a wider scope of allowable rotational angles for validation.

A 50 μm wide step test pattern was transferred onto 8 MgO substrates by photolithography before ion milling was performed[1]. Figs. 7.8-7.10 illustrate the AFM results of three of the obtained step-edges corresponding to values of $\beta = 0^o, 20^o, 45^o$. It can now clearly be seen how the step profile is characterised by redeposition if the shading angle exceeds the resist angle (Fig. 7.8). In Figs. 7.9 and 7.10, we can see the effect of increasing the rotational angle, decreasing the shading angle and redeposition effect. The shape of the step test pattern will inevitably cause a sharper edge on one side (shaded) and a rounded edge on the other (exposed).
From Fig. 7.11 it can be seen that the theoretically predicted step angles correspond reasonably well with the measured values. The deviation becomes considerable at high shading angles due to the resist angle and the occurrence of redeposition.

[1]The high etch mode of the Argon mill was used for all step-edge milling

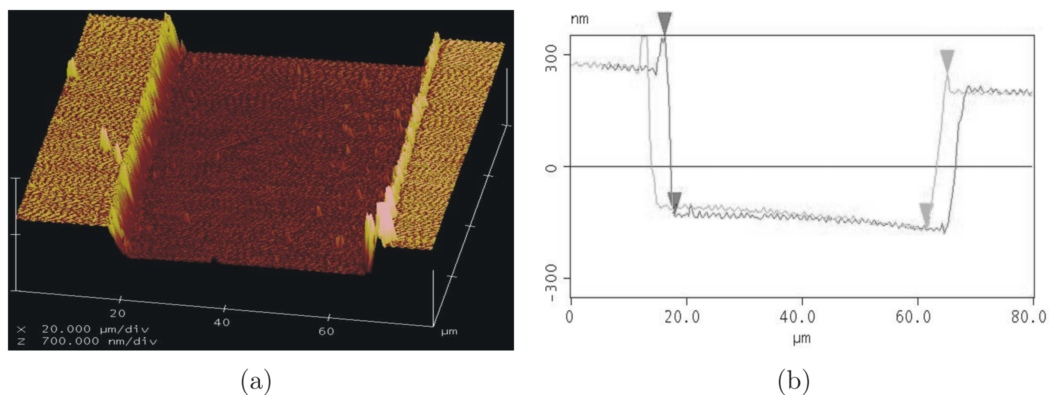

(a) (b)

Figure 7.8: Step profile in (a) 3D and (b) 1D for $\beta = 0^o$ and $\omega = 17^o$

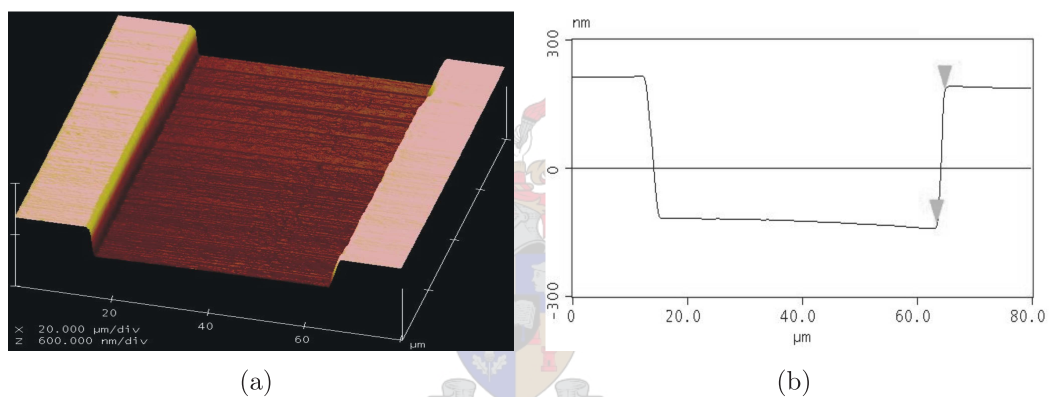

(a) (b)

Figure 7.9: Step profile in (a) 3D and (b) 1D for $\beta = 20^o$ and $\omega = 11^o$

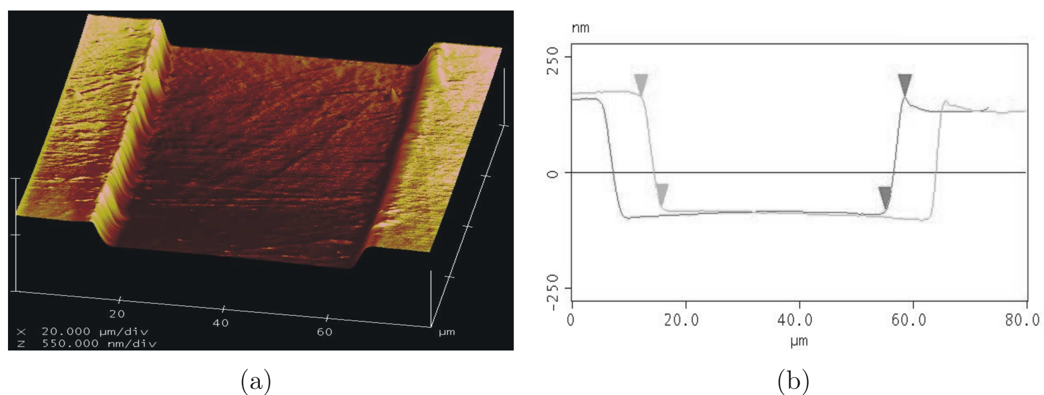

(a) (b)

Figure 7.10: Step profile in (a) 3D and (b) 1D for $\beta = 45^o$ and $\omega = 8^o$

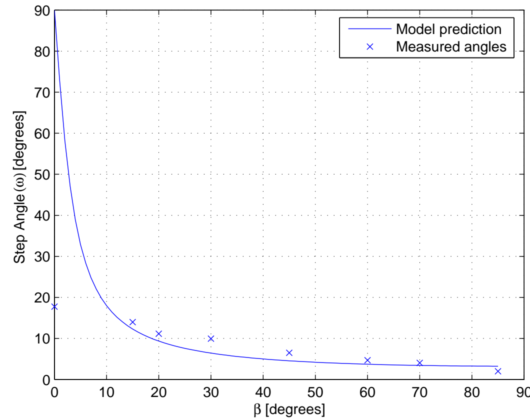

Figure 7.11: Predicted and measured MgO step angles

Despite the fact that it is possible to obtain step angle larger that 10°, the reproducibility of such a process would be extremely limited. This was seen by the frequent occurrence of rounded edges in the step profile after redeposited material was removed. The only feasible solution was to investigate possible reasons for the low relative etch rates.

7.5.4 Identification of Selectivity Problems

Although oxide substrates have very slow etch rates, the etch rates obtained with our Argon mill were particularly slow compared with typical etch rates reported in literature [13]. This fact prompted the suspicion that there could exist an inherent problem with the milling system.
Three possible reasons were identified for the poor selectivity:

- The presence of reactive ions in the plasma increases the photoresist etch rate significantly. The Argon ion mill could only reach a base pressure of 8.10^{-5} mbar. If it is considered that the typical milling pressure is around 3.10^{-4} mbar, this could be a major problem.
- The protective mask is simply too soft.
- The use of physical bombardment of argon ions is insufficient, necessitating a reactive ion etching process (with chlorine as reactive gas [26]) to improve the MgO etch rate.

7.5.5 Improvements to Fabrication Process

The first problem that was addressed, was the base pressure of the Argon Mill. By stepwise reassembling the mill, replacing o-rings and reapplication of vacuum grease, the base pressure was improved by a factor of 10 to 8.10^{-6} mbar. When this improvement was tested, no significant difference to selectivity could be observed.

The next matter that was investigated was the hardness of the photoresist mask. Attempts to harden the mask by longer bake times failed to deliver better results. As an alternative, the possibility of using a different mask was explored. Reports show that several masks other than photoresist have been used with reasonable success. Popular choices include niobium [50] and amorphous carbon masks [51]. As niobium was readily available, it was seen as a logical choice.

Firstly, a photoresist step pattern was transferred onto an MgO substrate through a standard photolithograpy process (as explained in Chapter 3). The next step was to cover the substrate with niobium. This was accomplished by a PLD deposition carried out at room temperature. To remove excess niobium, a lift-off process was performed by soaking the sample in acetone for approximately 30 seconds with the aid of ultrasonic excitation. The results that were obtained provided limited success. Despite achieving mask angles of 67°, the profile of the mask was very poor. This occurred because of the resist angles proving not steep enough for a high quality lift-off process. Fig. 7.12 illustrates the "breaking" of the niobium at the edges during lift-off resulting in an unusable step profile.

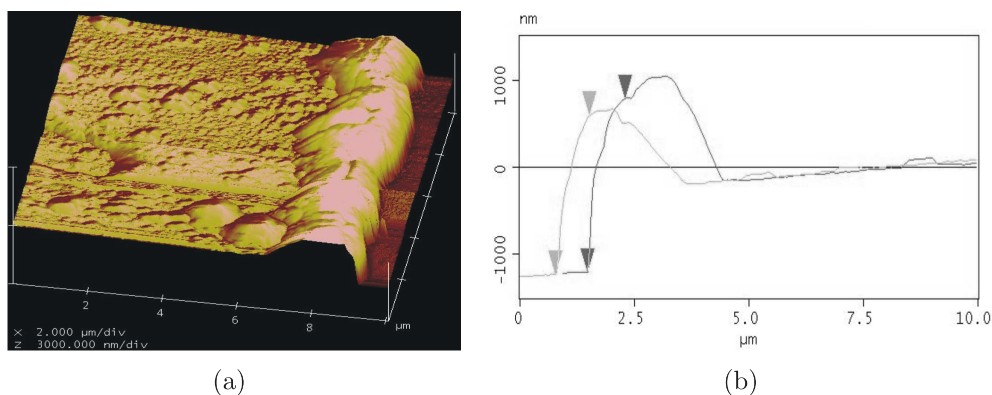

(a) (b)

Figure 7.12: Lift-off of a niobium metal mask

After ruling out a reactive etch process (due to cost considerations), two options remained: To improve resist angles even further (possibly using e-beam lithography) or to find a softer substrate material while maintaining good crystal matching with the YBCO film. E-beam lithography is currently being investigated at Stellenbosch but no immediate successes have been achieved. Accordingly, the use of different substrates was considered. The most popular substrates used as a template for YBCO deposition are $SrTiO_3$, $NdGAO_3$ and $LaAlO_3$. These substrates would, however, not solve the selectivity problem as they all exhibit etch rates similar to that of MgO.
Instead, the use of a buffer layer with a fast etch rate seemed to be a promising alternative.

7.5.6 Buffered Step-edge Junctions

The need for a material with a faster milling rate compared to conventional substrates prompted the idea to use a buffer layer as an epitaxial template for a step-edge junction. In literature, such buffer layers are restricted to oxides such as CeO_2 on YSZ and $SrTiO_3$ on MgO substrates (with slow etch rates) [52]. The motivation for using these buffer layers are usually limited to improve the lattice matching with YBCO. An ideal buffer layer was found in $PrBa_2Cu_3O_{7-\delta}$.

7.5.6.1 YBCO/PBCO Superlattices

$PrBa_2Cu_3O_{7-\delta}$ has a crystallographic structure almost identical to $YBa_2Cu_3O_{7-\delta}$ with comparable values of the lattice parameters. Furthermore, PBCO is not metallic, its resistivity is high at room temperature and increases at low temperature (semiconducting behaviour) without any trace of a transition to a superconducting state. These properties makes this material ideal for a buffer layer. The etch rates of PBCO should also be quite similar to YBCO which are much higher than that of oxide-substrates.

Possible problems that can occur is Pr/Y interdiffusion. It has been reported that a 45% atomic Pr interdiffusion into the first YBCO layer would result in a Tc of 30 K for the resulting alloy. Charge transfer from the YBCO to the PBCO layer would also result in a decrease of the transition temperature [53]. Fortunately, these effects should not have a significant effect when a reasonably thick YBCO layer is deposited over the PBCO.
The immediate challenge was thus to fabricate a target and then to epitaxially grow c-axis $PrBa_2Cu_3O_{7-\delta}$ on an MgO substrate.

Pectora roborant cultus recti

7.5.6.2 Fabrication Process

By introducing an extra layer into the fabrication process, several new considerations have to be taken into account. The thickness of the PBCO/YBCO superlattice could possibly approach critical values where microcracks can start becoming a factor. The added surface roughness introduced by using a buffer layer will possibly lead to structural defects in the superconducting YBCO layer, reducing its current-carrying abilities and critical temperature. For this reason, it was necessary to pay special attention to the epitaxy and surface quality of the deposited PBCO layer.

As PBCO is not a conductor, DC magnetron sputtering could not be used (due to target charging problems). As a result, Pulsed Laser Deposition was used to deposit the PBCO layers onto the MgO substrates. For this purpose, a planar $PrBa_2Cu_3O_{7-\delta}$ target was created (details of target fabrication can be found in Appendix A). A comprehensive study on the deposition conditions of PBCO on MgO substrates could not be found in literature. Consequently, it seemed reasonable to use the deposition parameters similar to those used in a standard YBCO deposition. Optimisation of the deposition parameters was restricted to temperature variation due to its dominating effect on surface quality. The temperature variation was done over the temperature range 700-800 ^{o}C. Each deposition was performed for 15 minutes, corresponding to a layer thickness of around 250 nm. Characterisation of six buffer layers were done through XRD and AFM analysis.

Pectora roborant cultus recti

7.5.6.3 Buffer Layer Analysis

XRD results confirmed that c-axis PBCO favours deposition at lower temperatures than YBCO. The layer deposited at 700°C showed excellent c-axis crystallinity. From Fig. 7.13 we can clearly see prominent (00l) peaks without any secondary phases or a-axis growth being present. As the deposition temperature was raised, the introduction of unwanted peaks were observed. This included a prominent (110) peak at 32.7^o (see Fig. 7.14).

AFM analysis confirmed the presence of droplets characteristic to the PLD process. A definite difference in growth modes was observed for higher temperatures. It would seem that the presence of edge-dislocations are more prominent at higher temperature, which coincides with the rougher surface obtained. This is clearly illustrated in Fig. 7.15. The results for the measured AFM roughnesses are summarised in Table 7.1. A surface roughness of only 7 nm was obtained for the film deposited at 700°C. Accordingly, this deposition

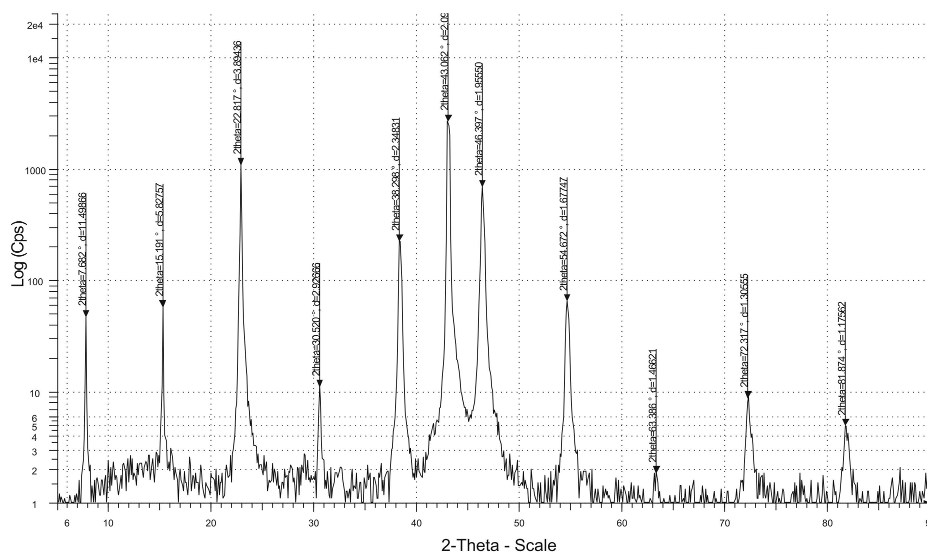

Figure 7.13: XRD analysis of a PBCO thin film deposited at 700°C

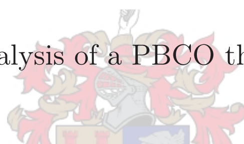

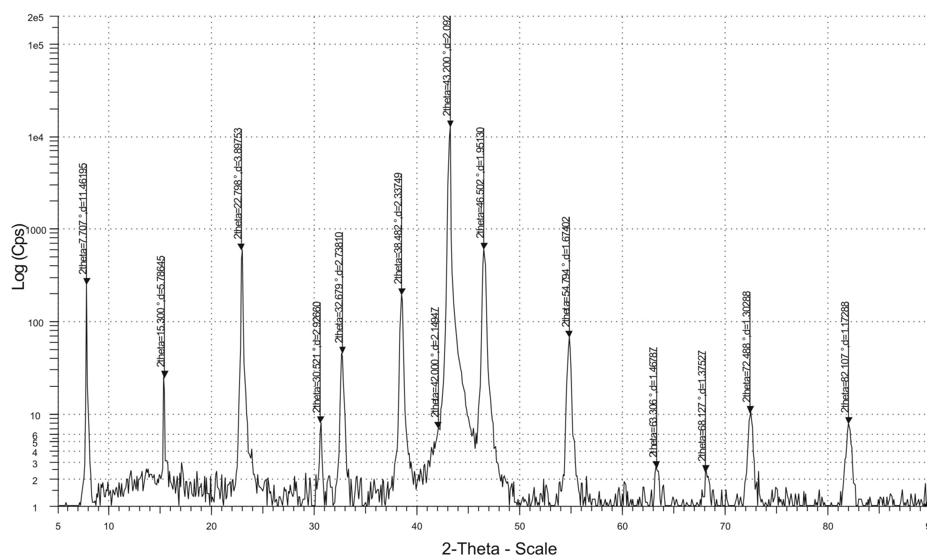

Figure 7.14: XRD analysis of a PBCO thin film deposited at 720°C

temperature was chosen as optimal from both a crystallinity and surface quality perspective (see Table 7.2 for optimal parameter set).

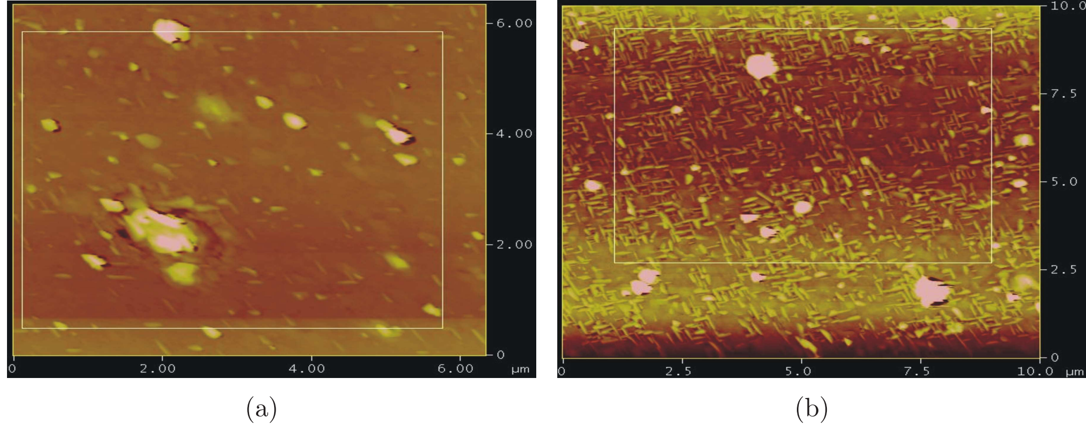

(a) (b)

Figure 7.15: AFM analysis of PBCO thin films deposited at (a) 700°C and (b) 720°C

T_{dep} [^oC	Surface Roughness [nm]
700	7.88
720	11.85
740	12.27
760	26.52
780	33.12
800	31.34

Pectora roborant cultus recti

Table 7.1: Measured surface roughnesses for 6 PBCO depositions

Parameter	Value
T_{dep}	700°C
Laser/Pulse frequency	16 Hz
P_{O_2}	5.10^{-2} mbar
Laser fluence	4.09 J/cm^2
Working Distance	60 mm
Focal Distance	15 mm
Deposition Time	15 min
T_{anneal}	30 min

Table 7.2: Optimal parameter set for PBCO deposition

7.5.6.4 Step-edge Model Revisited

After having optimised the deposition conditions of the "softer" PBCO buffer layer, it was necessary to characterise its etching behaviour to determine the relative etch rate, x. As was done in the case of the MgO substrates, several etch runs were performed at various incident beam angles. The results are illustrated graphically in Fig. 7.16. In this figure we can see the relative etch is again minimised at $\alpha = 30^o$ where the etch rate of the PBCO almost matches that of the photoresist. It is clear that the PBCO etch rate is significantly faster than that of MgO (compare to Fig. 7.5). The step angles could now be re-evaluated for a given incident beam angle and variable rotational angle. To serve as further validation of our model, the value of α was chosen as 60^0, allowing a relatively wide range of obtainable shading angles which is below the photoresist angle.

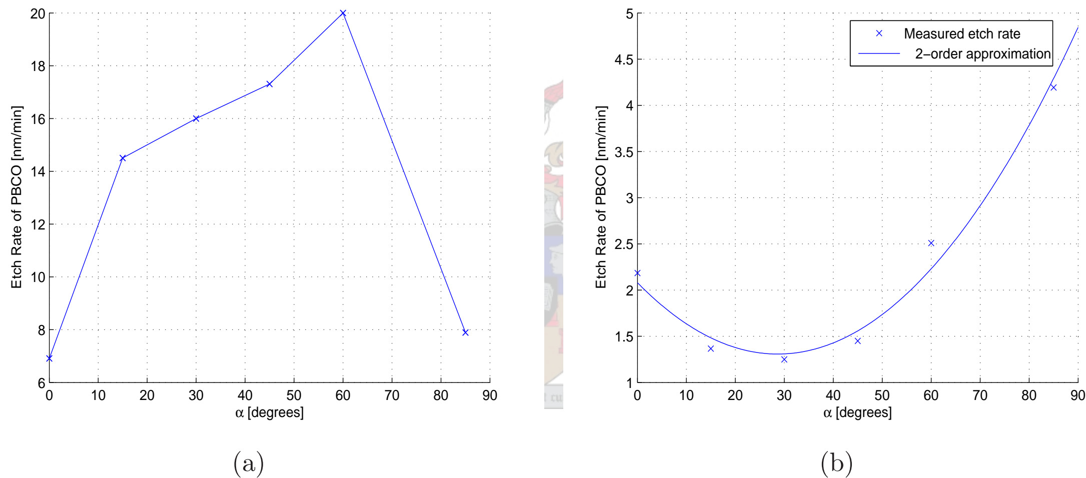

(a) (b)

Figure 7.16: Results of PBCO etching: (a) PBCO etch rates and (b) relative etch rates

The results of the theoretically predicted and practically obtained step angles are shown in Fig. 7.17. Again these values correspond quite well for shading angles not exceeding the resist angle (from Fig. 7.4, for a tilt angle of 60°, β should be larger than 13° to produce a shading angle less than 70°). The step angle that was obtained, easily exceeded the required 10°. The step profiles showed minimal redeposition and sharp edges, making this a very promising template for our Josephson junction (see Fig. 7.18).

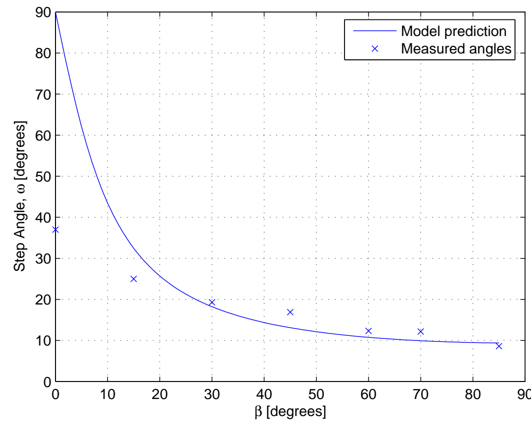

Figure 7.17: Predicted versus measured PBCO step angles

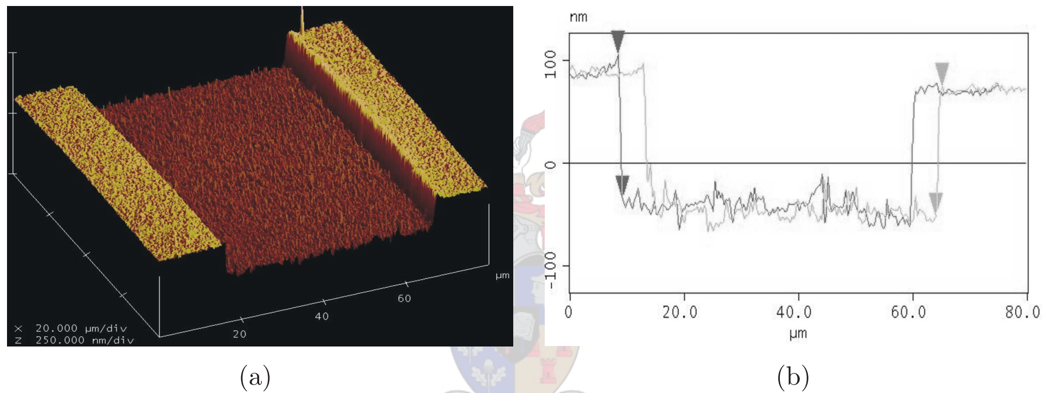

(a) (b)

Figure 7.18: Step profile of a PBCO step-edge for $\alpha = 60^o$, $\beta = 15^o$ and $\omega = 25^o$

7.6 Annealing of Steps

Once a desired step profile has been obtained, it is necessary to anneal the milled step in a pure oxygen environment. After bombarding the substrate/buffer layer with energetic ions, the crystal structure is inevitably damaged in some regions. These regions can thus inhibit epitaxial thin film growth. The situation can be remedied by allowing the material to re-oxygenate at an appropriate temperature. In the case of MgO substrates, this anneal process will occur at 1100°C. Since PBCO was used as a template layer, the annealing of the step can take place at much lower temperatures. Due to the similarity in chemical composition to YBCO, it was decided to anneal the step at 500°C for 30 minutes. The anneal process was performed in a PLD chamber after which the thin film was deposited without having to expose the step to an atmospheric environment.

7.7 Thin Film Deposition

After the step was annealed, a superconducting YBCO layer was deposited by pulsed reactive crossed beam laser ablation. This deposited thin film has to possess certain desirable qualities. These include a T_c as close to 90° as possible, a small ΔT, good surface roughness and pure c-axis growth. To ensure proper step coverage and to minimise on-chip parameter drifts, the film thickness should also be uniform over the substrate. PLD is, however, renowned for producing small-area uniformity, necessitating very good alignment of the plume and substrate. Magnetron Sputtering was not used for step-edge film coverage owing to reports that the growth mechanisms can be unpredictable and not suited for producing step-edge junctions [13]. The unavailability of Transmission Electron Microscopy (TEM) analysis would also have limited characterising such a process. To realise a operational JJ, the thickness of the deposited film should also be monitored very carefully. If the film is too thick, the possibility exists that the step-edge would become too rounded. In such a case, the grain boundary close to the step-edge is shunted by a superconducting channel which dominates current transport properties. For this reason, all films thicknesses were about 70% of the step height.
The deposition conditions for YBCO (as optimised for deposition on MgO substrates) are listed in Table 7.3. Since YBCO has never before been grown onto PBCO at Stellenbosch University, it was necessary to re-establish the film characteristics.

Parameter	Value
T_{dep}	740^oC
Laser/Pulse frequency	16 Hz
P_{O_2}	5.10^{-2} mbar
Laser fluence	4.09 J/cm^2
Working Distance	60 mm
Focal Distance	15 mm
Deposition Time	11 min
T_{anneal}	30 min

Table 7.3: Optimal parameter set for YBCO deposition

To investigate the superconductivity of the film, a susceptance measurement was done (see Fig. 7.20). The measurement revealed a T_c of about 85° but a very poor transient profile with $\Delta T = 20^o$. This is an indication of poor uniformity in the film quality. Despite this fact, the film quality should prove sufficient to manufacture a JJ.

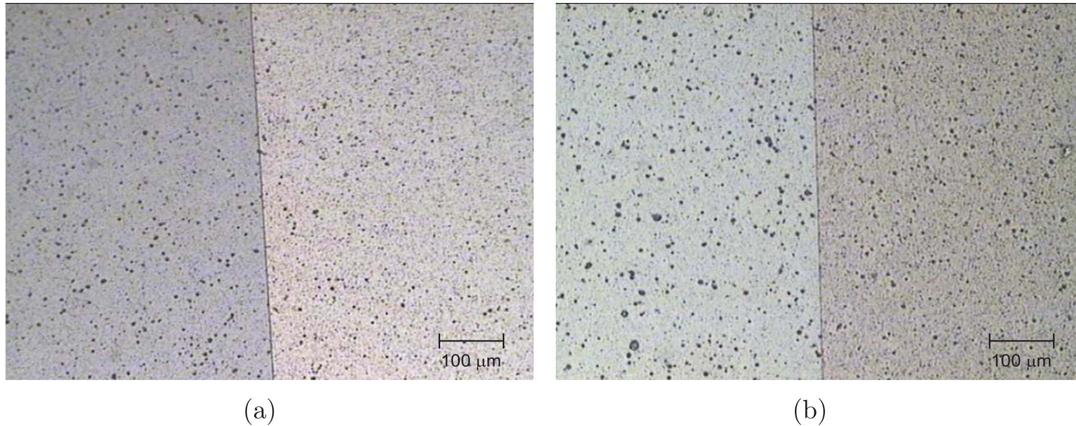

Figure 7.19: Optical microscope images of milled step (a) before and (b) after an YBCO layer is deposited

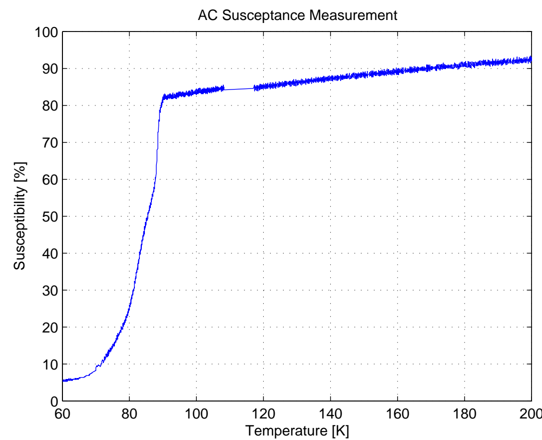

Figure 7.20: Susceptance measurement of YBCO film on PBCO step

7.8 Circuit Patterning: Photolithography and Argon Milling

After film deposition, the superconducting circuit can be patterned. Pattern transfer was achieved by the standardised photolithography process that was explained in Chapter 3. The chrome mask that was used for contact exposure is shown in Fig. 7.21. The mask consists of ten tracks, a ground plane, contact pads and alignment marks. Each track has a region of constricted width that should coincide with the position of the milled step upon mask alignment. The widths of these track-constriction regions vary in size whereby the outer tracks are 10 μm wide scaling down to 4 μm for the center tracks. These widths

are smaller than $4\lambda_J$ (a short junction) and an applied field will penetrate the junction uniformly allowing flux dynamics to be neglected when performing circuit testing.

After the photoresist is patterned, the sample can be argon-ion milled. The sample was tilted to 60° (optimal YBCO etch rate) without rotation to allow for a short milling time of the YBCO film (no step angle considerations is now applicable, only time considerations). This avoids the risk of the resist burning which becomes a factor when milling time approaches 45 minutes. Instead, by using this substrate orientation, a mill time of only 10 minutes is needed, allowing the easy removal of the resist after milling. The mill parameters are listed in Table 7.4.

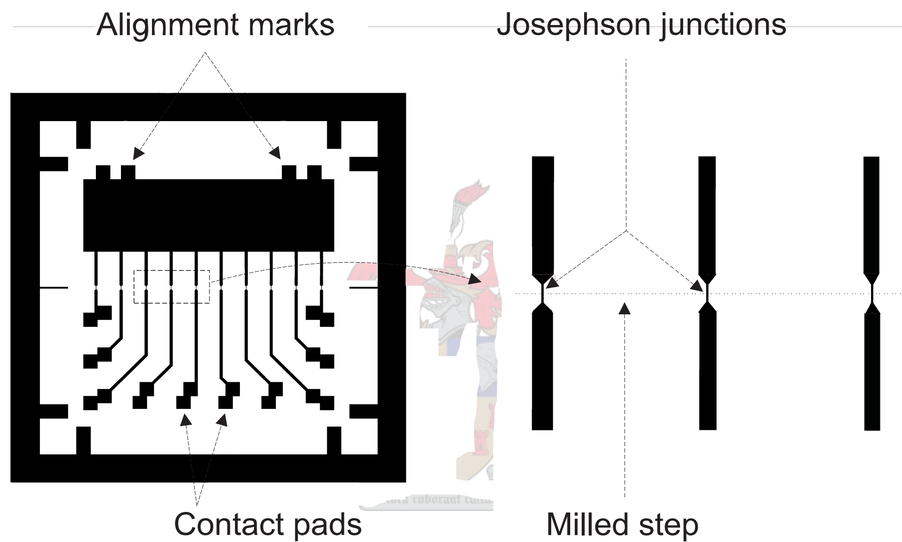

Figure 7.21: Chrome mask used during contact exposure

Parameter	Value
V^+	1 kV
V^-	2 kV
I^+	3.8 mA
I^-	3.2 mA
P_{RF}	50 W
P_{Ar}	3.10^{-4} mbar
Mill time	10 min

Table 7.4: Parameter set for Argon Ion milling of YBCO

Due to the color similarity between PBCO and YBCO, optical inspection is not reliable to know when the YBCO layer is completely milled. For this reason, milling was continued until the MgO substrate was visible, eliminating the possibility of unwanted short circuits. Fig. 7.22 illustrates the patterned YBCO circuit with the aligned step edge clearly visible.

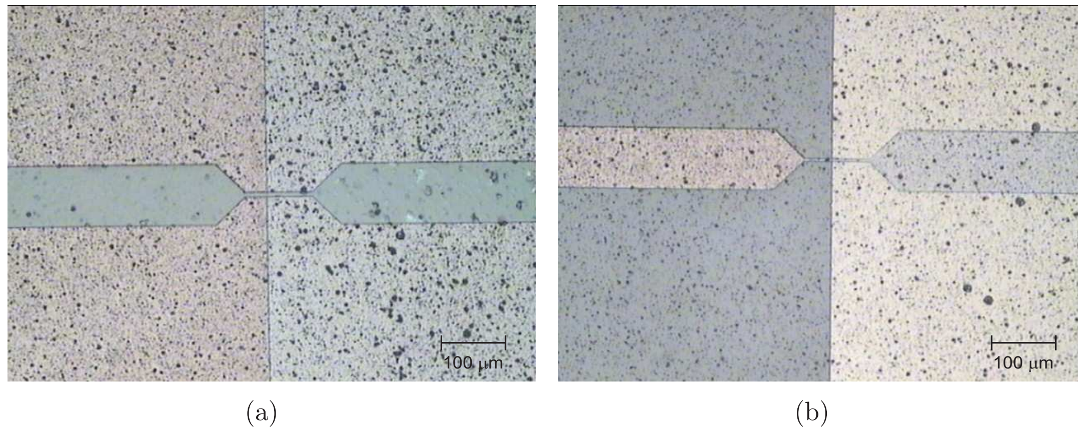

(a) (b)

Figure 7.22: Optical microscope images of (a) patterned photoresist before milling (b) patterned YBCO after milling

7.9 Establishing Electrical Contact

The final step in production is to establish an electrical contact to the superconducting circuit. From literature, two materials are generally used as contact materials: silver (Ag) and gold (Au). These metals are well-suited for this purpose, allowing for good adhesion while not reacting chemically with the YBCO film.

Before 2005, a thermal evaporation technique was used to deposit silver contact pads. This technique did not produce good electrical contact which was the reason for many produced circuits to be labeled “untestable”. As a result, it was decided to develop a new technique: depositing gold with conventional PLD. The main advantages of this technique are that the gold can be deposited at temperature in a pure oxygen environment after which an anneal process can be preformed in situ. This technique provided excellent electrical contact (see Table 7.5 for parameter set used during deposition). Before deposition can commence, however, an alignment of the contact pads with a protective mask is required. This was accomplished using a metal mask with 0.5 mm holes drilled where the gold pads

should be deposited on the patterned YBCO. The alignment was performed with the aid of an optical microscope.

Parameter	Value
T_{dep}	480^oC
Laser frequency	16 Hz
P_{O_2}	2.10^{-1} mbar
Laser fluence	4.09 J/cm^2
Working Distance	30 mm
Focal Distance	0 mm
Deposition Time	50 min
T_{anneal}	30 min

Table 7.5: Optimal parameter set for gold deposition

Once the gold pads were deposited and annealed, the circuit was wire-bonded to a PCB. The PCB that was used is illustrated in Fig. 7.23. The YCBO circuit was firmly pasted onto a copper base which was fitted into an opening in the PCB to ensure better thermal contact to the sample during cryo-testing. Next, 20 μm thick gold wires were bonded. To lower interface resistance, 4/5 wires were bonded from each gold pad to the corresponding copper pad on the PCB (see Fig. 7.24).

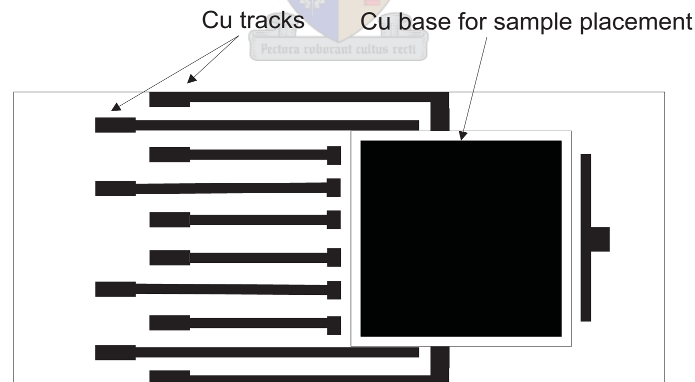

Figure 7.23: PCB used for circuit packaging

This completed the fabrication of the step-edge Josephson junction. Testing could now be performed to establish if the circuit was indeed operational.

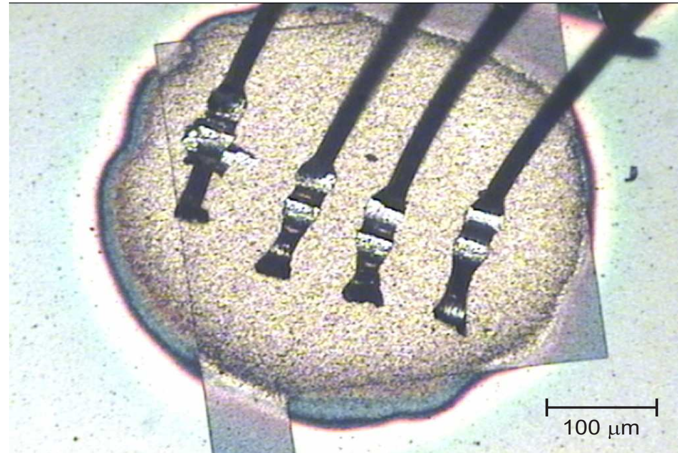

Figure 7.24: Illustration of 4 wirebonds on a gold pad

7.10 Chapter Overview

This chapter presented an entire fabrication process for step-edge JJs. Each stage of the process was handled in detail to ensure a complete understanding of the underlying mechanisms involved. A model for the dry-etching of step-edges was given and validated. The model allowed for the recognition of critical process parameters. In particular, the influence of selectivity on the attainable step profiles required considerable attention. The novel idea to fabricate buffered step-edge junctions originated from this selectivity problem. This buffer layer was characterised and integrated successfully into the fabrication process. Finally, the past problem of unreliable electrical contact was also resolved.

Chapter 8

Experimental Results

After establishing a complete fabrication technique for Josephson junction structures, it was necessary to test the circuit and determine if junction behaviour is in fact manifested. Junction classification depends on the presence/absence of the dc and ac Josephson effects. A complete study of the IV-characteristics displayed by a proposed junction will confirm such a classification as well as provide additional insight into junction operation. This chapter presents the procedure followed to test the junctions and interprets the results that were obtained.

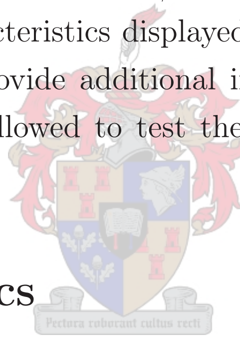

8.1 IV-Characteristics

To evaluate critically the IV-characteristics of a Josephson junction, a few concepts need to be explained in more detail. Typically, we can classify "junction-like" IV-characteristics with the sharp onset of the voltage state when the critical current of the junction is exceeded. The transition profile into the finite voltage state should, however, be included in our "junction-like"-definition. The transition profile should follow an upward concavity

$$V \propto (I^2 - I_c^2)^{\frac{1}{2}} \tag{8.1.1}$$

to be classified as a Josephson junction. In many instances, IV-characteristics are mistaken for junctions where in fact flux flow behaviour is exhibited. Many acceptable junctions (exhibiting upward concave IV-profiles near T_c) can become mere superconducting filaments as temperature is decreased exhibiting flux flow dynamics (see Section 8.1.1) [16]. This transition can only be recognised by correct interpretation of the IV-profile.

8.1.1 Flux Flow

When a transport current flows in a type II HTS in the mixed state, flux vortices threading the superconductor, will be subjected to a Lorentz force. This force is perpendicular to the direction of current flow and acts to move these vortices in a transverse direction to the current flow

$$F_L = J \times B. \tag{8.1.2}$$

This vortex movement lead to the onset of resistance and power dissipation. Defects in the superconducting film reduce the effect of flux flow by pinning flux vortices at defected sites in the film. This natural occurrence of defects in HTS films produce sufficient barriers to suppress vortex-motion. As the transport current is increased, the Lorentz force can become large enough to unpin these vortices. Flux flow can also become more prominent as temperature is increased. The average pinning force decreases exponentially with temperature due to thermally activated flux mobility [7]. Flux motion can be divided in two categories:

- Flux creeping, associated with a stabilised flux distribution where magnetic pressure is relieved in a controlled manner.
- Flux jumps, occurring when avalanches of flux bundles are released. This phenomenon is usually associated with high temperatures (near T_c) where the pinning forces are significantly reduced.

Flux flow can be identified by a downward concavity in the transition profile occurring just above I_c. This is illustrated in Fig. 8.1.

8.2 Test Setup

To test the fabricated junctions, the sample (mounted on an PCB) was positioned on a copper base inside the cold finger cryo-unit. To ensure better thermal contact, heat conducting paste was used. The cold finger has four probe wires available to provide circuit excitation and to monitor circuit response. Excitation was provided by a Mr. SQUID Electronics unit [54] generating a triangular waveform, sweeping current in the range 0 - 3.5 mA (the neglegible junction resistance does not load the unit which can be seen as a variable current source). The response of the circuit was fed back to the

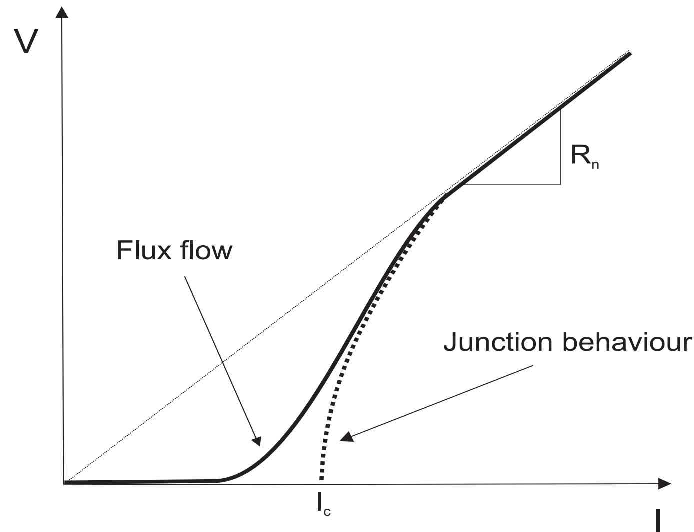

Figure 8.1: A depiction of junction-like and flux-flow behaviour

Mr. SQUID Electronics unit where a built-in low noise amplifier amplified the signal to be displayed on an oscilloscope. A mu-metal shield was position around the sample to minimise ambient noise from the vacuum pump, cryo-cooler etc. A simple wire antenna (a high frequency cable), was installed inside the cold finger and placed over the mounted PCB. This cable was then connected to a 2-18 GHz rf source to provide rf excitation whereby the presence/absence of Shapiro steps could be investigated (see Fig. 8.2).

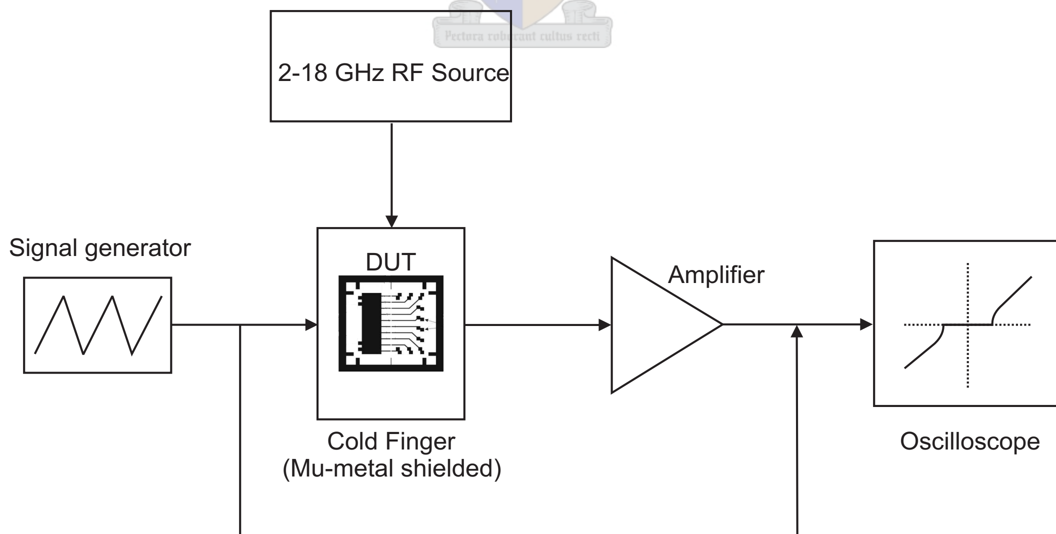

Figure 8.2: Schematic of the basic test setup

The final component of the test setup, was to introduce a magnetic field in the vicinity of the junction. For this test, the mu-metal shield had to be removed to allow magnetic flux to reach the sample. This was accomplished by mounting a 2-coil system over the cold finger. The coils were positioned so that the magnetic field lines would orientate perpendicular to the sample and the direction of current flow. A Hall probe was used to calibrate the magnetic field beforehand.

8.3 Buffered Step-edge Measurements

Each sample, prepared according to the PBCO buffered step-edge junction technique, comprised 10 junctions of variable size as determined by the mask used. The first junction to be tested was a 10 μm wide YBCO track grown over a 25^0 PBCO step-edge. Initial testing was only focused on circuit response to DC excitation. The obtained IV-curves showed very well-defined IV-characteristics.

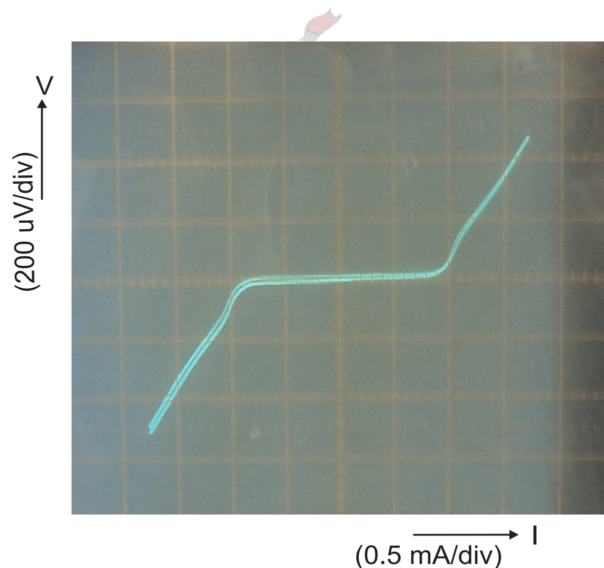

Figure 8.3: Measured IV characteristics at 70 K

From the IV-curve shown, it can be seen that true junction-like behaviour is present without any downward concavity indicating flux-flow. From this initial test, it can be concluded that the junction is electro-magnetically small and demonstrates a current-voltage (IV) characteristic predicted by the resistively and capacitively shunted junction (RCSJ) model. The junction is also overdamped, corresponding to a McCumber parameter $\beta_c < 1$, which is evident by the absence of hysteresis. No "kinks" in the IV-profile could be detected

suggesting that only one grain boundary is present which defines the critical current of the junction. It is thus reasonable to assume that the step angle was too shallow to give rise to the formation of a second junction (in series) at the bottom edge of the PBCO step.

The quality factor of the JJ is defined by the product $I_c R_n$. Accordingly, an I_c-T and a R_n-T profile were measured. Asymmetry in IV-characteristics is quite common. This is probably due to trapped flux in the grain boundary or in the vicinity of the abutting grains. Accordingly, I_c was taken as half the sum of the measured I_c in both directions. The cryo-cooler could, however, only reach 38 K limiting the testing range somewhat. The obtained profiles are illustrated in Fig. 8.4.

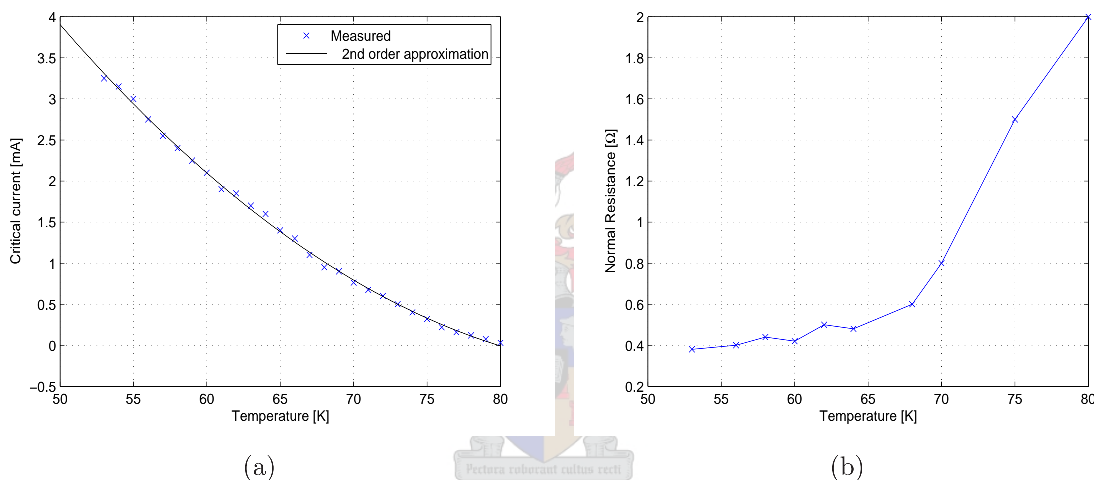

(a) (b)

Pectora roborant cultus recti

Figure 8.4: (a) I_c and (b) R_n as a function of temperature

From these figures it can be seen that the I_c values obtained for the junction are quite large, and follows a quasi-quadratic profile

$$I_c \propto (1 - \frac{T}{T_c})^2. \tag{8.3.1}$$

Furthermore, I_c values were only recorded from 53 K. This was due to the limited current that could be supplied by the Mr. SQUID unit. Thus, the classification of the I_c-T dependency as a quasi-quadratic profile does not necessarily apply for lower temperatures. If indeed this should be the case, it would render the results quite remarkable considering an I_c of 3.2 mA at 53 K extrapolated to around 17 mA at 4 K. If a linear extrapolation

is used instead, a critical current of 9 mA at 4K would result. The other important datapoint of note is the value of I_c at 77 K (the boiling point of liquid nitrogen) being 160 μA. This value is undoubtedly restricted by the film quality. The transient profile that was obtained from the susceptance test illustrated a gradual transition into the superconducting state extending from 85 K to 65 K. This will inevitably affect the junction quality as the increasing density of normal regions inside the film will restrict its current carrying abilities. The definition for the junction-T_c was taken to be the extrapolated temperature at which I_c reaches zero. This measurement was, however, made difficult by the presence of Lorentzian noise observed for temperatures above 75 K. This noise originates in part from hopping of trapped flux vortices between pinning sites due to increased thermal energy. The approximate value of T_c was determined to be 80 K.

The R_n-T curve illustrates the expected independence of the junction normal resistance on temperature for the low temperature domain extending to 60 K. R_n in this region corresponds to about 0.5 Ω. Accordingly, the I_cR_n of the junction at 53 K is 1.6 mV. The junction resistance increases as temperature exceeds 65 K. This was again contributed to the film quality and the emerging normal regions within the film and adjacent to the grain boundary.

The next test was to investigate the influence of rf power on the junction behaviour. Shapiro steps is widely considered as the fingerprint of a true Josephson junction, and observing such a phenomenon would prove indisputably that the circuit is in fact a JJ. The test was conducted by sourcing 8 dBm rf power through the wire antenna to the circuit[1]. By varying the frequency of the rf source distinct variation in the IV-curves could be detected. Finally at 8.891 GHz (at 40 K), well-defined Shapiro steps were seen (see Fig. 8.5). Shapiro steps are the most precise method of determining the Voltage Standard and used by the National Institute of Standards. The step sizes can be used to calculated the theoretical constant e/h. To verify this fact with our measurement will, however, introduce some degree of uncertainty. This is due to the rounded nature of the observed steps which occur possibly because of small fluctuations in the frequency generated by the rf source or because of thermal noise (usually more dominant at temperatures near 70 K). From (2.4.7),

$$V_0 = n(\frac{\Phi_0}{2\pi})\omega_s \tag{8.3.2}$$

[1]Impedance mismatching would severely limit the coupled power

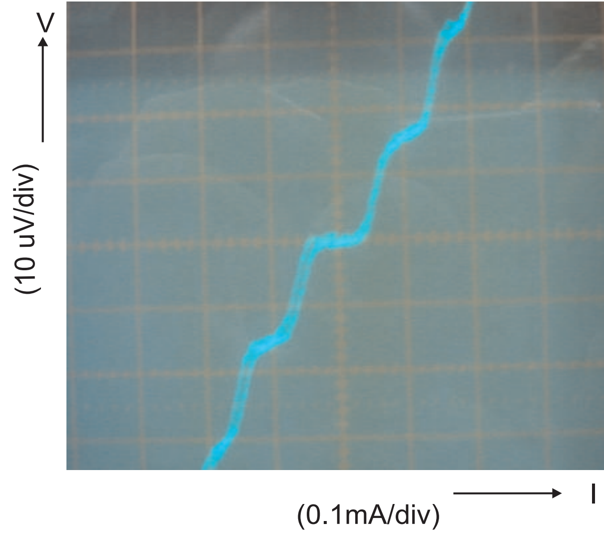

Figure 8.5: Shapiro Steps measured at 40 K at 8.891 GHz

which is equivalent to

$$V_0 = n(\frac{h\omega_s}{4\pi e}) = n\frac{hf_s}{2e} \tag{8.3.3}$$

where $\Phi_0 = \frac{h}{2e}$. This equation can now be rewritten to yield the theoretical constant $e/h = 2.417967\text{x}10^{14}$ Hz/V, formulated as

$$\frac{e}{h} = n(\frac{f_s}{2V_0}). \tag{8.3.4}$$

From Fig. 8.5, it can be seen that V_0 is approximately 18 μV and according to the test setup, $f_s = 8.891$ GHz. Substituting these values into (8.3.4), we obtain e/h $= 2.46944\text{x}10^{14}$ Hz/V. This value corresponds quite well with the theoretically predicted value.

8.3.1 Parameter Variation

To investigate the on-chip parameter spread, the other junctions on the sample were tested. As each chip contains two tracks of the same dimensions, the results measured for the second 10 μm track could be compared with the results provided above. These two tracks are situated on opposite ends of the sample and should give a good representation of the sample homogeneity. The I_c-T and R_n-T profiles observed for this second 10 μm track are given in Fig. 8.6. The values obtained for this track compare very well to the first track tested. Again a quasi-quadratic I_c-T dependence can be observed. The I_c of 3.5

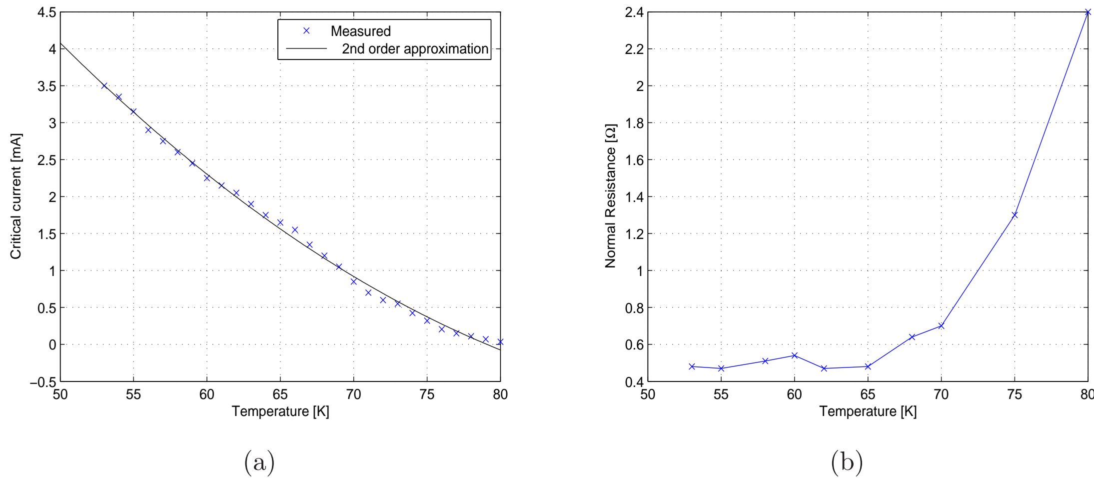

(a) (b)

Figure 8.6: (a) I_c and (b) R_n as a function of temperature for the second 10 μm track

mA at 53 K is, however, slightly higher (a 9% increase). The values of R_n are again fairly constant around 0.5 Ω for lower temperatures. At higher temperature, the measurement uncertainty increases and a higher variation in I_c was seen (14% at 77 K). The measured critical temperature was again 80 K indicating good uniformity with respect to film quality. Possible variations in thin film thickness (PLD deposition method can produce inhomogeous films due to small deposition areas obtainable) and step profile could in part explain the observed variations. These results compare fairly well to the typical 10-20% variation in I_c encountered for step-edge junctions reported in literature [13], [10].

As a final test, a 6 μm track near the center of the chip was tested. Again well-defined IV-characteristics and Shapiro steps were observed (see Fig. 8.7). As expected, slightly lower values for I$_c$ were obtained compared to the wider tracks (see Fig. 8.8). At 53 K, I_c had a value of 1.6 mA (compared to 3.2 mA and 3.5 mA for the 10 μm tracks). This fact enabled the testing range to be extended to 38 K to provide a more representative view of the I_c-T profile. The profile, however, remained quasi-quadratic without any indication of becoming linear. The R_n-T curve demonstrate a higher normal state resistance of 0.8 Ω corresponding to the 0.4 μm reduction in junction width.

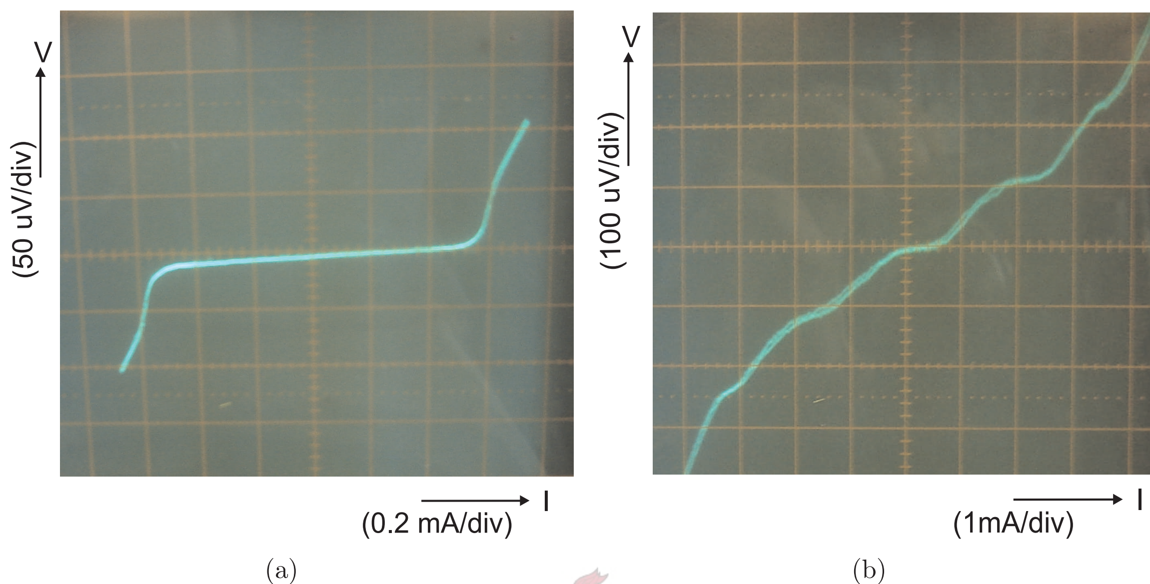

Figure 8.7: (a) The measured IV-characteristic at 70 K and (b) the corresponding Shapiro steps at 11.54 GHz

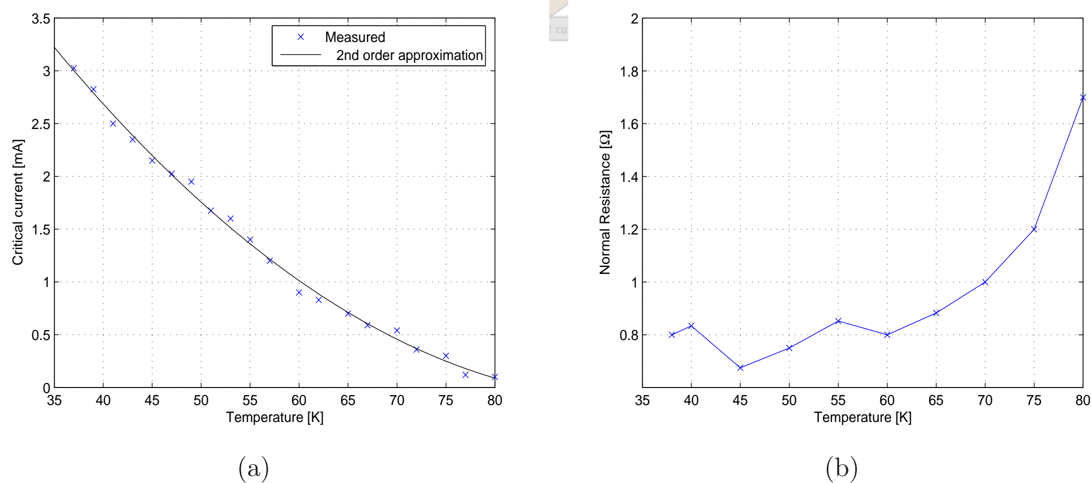

Figure 8.8: (a) I_c and (b) R_n as a function of temperature for a 6 μm track

8.3.2 Magnetic Behaviour

The magnetic behaviour of a junction can reveal much about the physical characteristics of the junction. The magnetic field will preferentially penetrate the grain boundary region of a junction verifying the fact that a grain boundary is a region of weakened superconductivity. The regularity of the I_c modulation pattern corresponds to the uniformity of the current density distribution inside the junction [13]. Due to the inhomogeneous edge-properties of a typical step-edge which can lead to differential YBCO growth, regular Fraunhofer patterns are, however, quite rare in SEJs. The magnetic field that the junction can withstand without modulation, also provides information about the physical dimensions of the junction. The observed modulation pattern is thus strongly dependent on the grain-misorientation angle introduced by the step-edge.

From literature, the critical current of a typical large-angle grain boundary junction is extremely sensitive to small applied magnetic fields. An experimental setup capable of producing magnetic fields in the range of 0-100 G was accordingly used during initial testing. No I_c suppression could be observed within this field range. Even at higher temperatures where magnetic sensitivity increases, no modulation could be detected. This magnetic insensitivity was very intriguing and quite unexpected considering the relatively large structural dimensions of the YBCO tracks. Accordingly, a stronger magnetic field was applied to the junction. Only at 1 kG (0.1 T) could a slight modulation in the value of I_c be noticed. Due to the unavailability of a larger power supply, the magnetic field strength could not be further increased.

It is known that for shallow misorientation angles (less than 10°), I_c is rather insensitive to an applied field corresponding to a narrow region of weakened superconductivity (in the order of a few Angstroms). At angles approaching 25°, the field dependency typically becomes more pronounced and a Fraunhofer-like pattern starts to emerge [8]. Few reports exist of Josephson junctions not exibiting modulation in the presence of such strong fields (unless the junction area is very small such as the case with intrinsic junctions [55]). Däumling et al. reported 100 μm-wide 25° [001]-tilt grain boundary junctions subjected to 5 T magnetic field strength [56]. These junctions exhibited strong modulation around 0.1 T with little modulation occurring beyond 1 T. It is quite possible that the junctions fabricated in-house would exhibit similar characteristics for slightly larger fields. A similar dependency was found by the Oak Ridge group [57].

8.3.3 General Remarks

Initial testing of the junctions revealed very favourable electrical characteristics. Junctions with such high I_cR_n values and low magnetic sensitivity are ideal for RSFQ application. The mechanism of grain boundary formation is still under debate. It is, however, clear that no series junction formation exists over the step-edge. Typically, 90° grain-boundary formation takes place on step-edges milled into perovskite substrates when step angles exceed 45°. For more shallow angles, only flux flow behaviour is seen and no Shapiro steps are obtainable. PBCO (used as a buffer for the in-house step-edge fabrication) is also a perovskite material, but despite the shallow angle of 25° junction behaviour was clearly observed. One possible explanation is that a [001]-tilt grain boundary was formed at the step-edge (similar to step-edges junction fabricated on MgO substrates). This is, however, only speculation and should be confirmed with TEM analysis.

Finally, the junctions were tested several times and no significant deterioration in device performance could be observed, suggesting good thermal cycling capability. More testing still needs to be performed to establish a detailed parameter spread analysis. Due to insufficient laser energy and time considerations, further film depositions could not be done before the completion of this thesis.

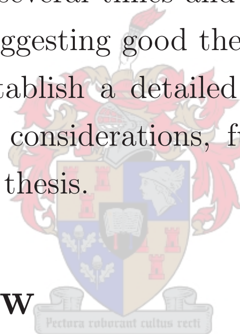

8.4 Chapter Overview

This chapter presented the testing procedure and results obtained for fabricated Josephson junctions. The IV-characteristic obtained for the novel PBCO buffer JJ was presented and interpreted. Results showed very good junction behaviour including Shapiro justifying Josephson junction classification.

Chapter 9

Conclusion and Recommendations

This chapter will attempt to give a general overview of the research presented in this thesis, highlighting the most important accomplishments that were achieved. Several possibilities for new projects are suggested to serve as motivation for current and future researchers.

9.1 Thesis Review

This thesis addressed a wide range of fabrication challenges related to HTS technology. The research facilities that existed before the commencement of this thesis had severe performance limitations and needed to be improved before any attempts toward device fabrication could be made. An brief overview of some advances made is listed below.

1. The first process that was studied was the photolithography process. The resolution obtained in mask transfer was insufficient to realise devices which require sharp edge profiles. As a result, this entires process was re-optimised. This allowed for results close to optimal values quoted in literature.

2. The in-house argon ion mill needed an in depth characterisation. Previously the mill did not possess a uniform etch profile exhibiting focused ion beam characteristics. Several experiments were conducted in an attempt to optimise the system but with limited success. It was finally decided to change the extraction system of the mill completely. By introducing a three-gridded ion source and a plasma bridge neutraliser, a significant improvement to the etch profile could be observed. The system was optimised to ensure predictable, stable operation.

3. The only method of thin film deposition until 2005 was the PLD. The results obtained were good from a superconducting perspective, but lacking with respect to surface morphology. Accordingly, the system operation was revised and after fitting a pulsed oxygen valve to the system, significant improvement to the surface quality of the films was observed. Again the system was re-optimised for this new configuration.

4. While the PLD produce relatively satisfactory results, there existed an urgent need for a second deposition system. Accordingly, a DC Inverted Cylindrical Magnetron was designed and built. A deposition process for YBCO thin films was characterised in detail using several analysis methods such as XRD, RBS, AFM and susceptibility testing. The results were excellent and comparable to commercial standards.

5. The next stride was to investigate a method to fabricate a Josephson junction. It was decided to fabricate a conventional step-edge junction on a (001) MgO substrate, but due to insufficient selectivity of the etch process, this idea was abandoned. The novel idea to use an insulative PBCO buffer layer as a template for a step-edge was attempted. This required the fabrication of a PBCO target and establishing appropriate PLD deposition parameters for this new process. After fabricating the PBCO step-edge, coating it with YBCO and patterning an appropriate circuit, the testing of the device could commence.

6. Testing of superconducting devices could never be conducted conclusively at the University of Stellenbosch due to the inability to establish good electrical contact to the superconducting films. This problem was remedied by converting to a PLD process of gold deposition (conducted at high temperature) which produced excellent contact.

7. After PCB mounting and wire-bonding, the Josephson junction circuits were tested for IV-characteristics in response to dc and ac excitation. Well-defined josephson-like behaviour (including Shapiro steps) was observed. This marked the first complete and successful in-house fabrication of a Josephson junction at the University of Stellenbosch.

9.2 Future Research Proposals

The future of HTS research at Stellenbosch seems very promising when considering all the improvements and successes that were attained over the past two years. Some interesting problems and new research opportunities emerged as a direct result.

Finalising Current Projects

Due to time constraints, some questions still remained unanswered concerning the fabricated Josephson junction. The growth mechanism of the PBCO step-edge is not completely clear, especially when considering the large magnetic field insensitivity of the junction. This should be confirmed with TEM analysis in the near future. The testing environment of the junction devices should also be significantly improved. The setup used was by far too noisy, and more time and funding should be dedicated to this effort. Furthermore, the cold-finger configuration (in its current state), can only reach 38 K. To obtain a complete set of results, testing needs to be conducted at temperatures approaching 4 K.

Multilayer technology

The ICM can currently produce very high quality YBCO thin films. The only immediate concern is the inadequate base pressures that the system roughing pump can realise. A turbo molecular pump should be fitted to the system to improve performance even further. Since the ICM can only produce thin films from conducting target materials, the possibility to design a rf sputter system should be considered to aid in the development of multilayer circuits. The PLD process does not meet the surface requirements to fabricate a device with more than two layers. Some initial testing in this regard revealed surface roughness reaching 50 nm after the third layer was deposited which is not up to standard.

Device Fabrication

After the successful fabrication of Josephson junctions, the next logical step is to produce SQUID devices. A chrome mask for SQUID patterning is already available and the fabrication process should be not be difficult. The Mr. SQUID Electronics unit can be used to aid in the characterisation of these devices.

Pectora roborant cultus recti

Now that high quality thin films on MgO substrates (low permittivity) are a reality, the fabrication of superconducting filters is also a very attractive prospect for the future. The test setup for such devices would probably be the biggest challenge.

9.3 Conclusion

The results obtained in this thesis mark the beginning of an exciting new era for HTS research at the University of Stellenbosch. Great strides were made toward improving the research environment by studying, optimising and characterising the individual processes. This systematic approach enabled the first Josephson junction to be fabricated successfully after many years of failed attempts. The fabricated step-edge junctions utilise the novel concept of a PBCO buffer and displayed good electrical characteristics. The introduction of a second deposition technique, the ICM, now makes the fabrication of 4 nm superconducting thin films a mere formality. This in itself is a major achievement as it opens possibilities related to filter technology and more complex multilayer technology.

List of References

[1] L. H. Snetler, “High Temperature Superconductor Step-Edge Fabrication for the Implementation of RSFQ Circuits,” Master’s thesis, University of Stellenbosch, January 2005.

[2] P. Chaudhari, J. Mannhart, and D. Dimos, “Direct Measurement of the Superconducting Properties of Single Grain Boundaries in YBCO,” *Physical Review Letters*, vol. 60, pp. 1653–1656, 1988.

[3] B. D. Josephson, “Possible New Effects in Superconductive Tunneling,” *Physics Letters*, vol. 1, pp. 251–253, July 1962.

[4] C. J. Fourie, “A 10 GHz Oversampling Delta Modulating Analogue-to-Digital Converter Implemented with Hybrid Superconducting Digital Logic,” Master’s thesis, University fo Stellenbosch, March 2001.

[5] R. P. Feynman, *The Feynman Lectures on Physics*, vol. III. Addison-Wesley, 1965.

[6] T. P. Orlando and K. A. Delin, *Foundations of Applied Superconductivity.* Addison-Wesley Publishing Company, Inc, 1991.

[7] T. van Duzer and C. W. Turner, *Principles of Superconductive Devices and Circuits.* Prentice Hall PTR, second edition ed., 1999.

[8] H. Hilgenkamp and J. Mannhart, “Grain Boundaries in High-Tc Superconductors,” *Review of Modern Physics*, vol. 74, April 2002.

[9] D. Dimos, P. Chaudhari, and J. Mannhart, “Superconducting Transport Properties of Grain Boundaries in YBCO Bicrystals,” *Physical Review B*, vol. 41, pp. 4038–4049, 1990.

Pectora roborant cultus recti

[10] R. Gross and L. Alff, "Physics and Technology of High Temperature Superconducting Josephson Junctions," *IEEE Transactions*, vol. 7, pp. 2929–2935, June 1997.

[11] A. W. Kleinasser and K. A. Delin, "High-Tc SNS Josephson Junctions: Moving Beyond Adolescence," *IEEE Transactions on Applied Superconductivity*, vol. 7, pp. 2964–2967, June 1997.

[12] K. P. Daly, W. D. Dozier, J. F. Burch, and R. W. Simon, "Substrate Step-edge YBCO RF SQUIDs," *Applied Physics Letters*, vol. 58, pp. 543–545, 1991.

[13] N. Khare, *Handbook of High-Temperature Superconductor Electronics.* Marcel Dekker, Inc., 2003.

[14] W. Reuter, M. Siegel, and K. Herrmann, "Fabrication and Characterisation of YBCO Step-edge Junction Arrays," *Applied Physics Letters*, vol. 62, pp. 2280–2282, 1993.

[15] K. Char, M. S. Colclough, S. M. Garrison, N. Newman, and G. Zaharchuk, "Biepitaxial Grain Boundary Junctions in YBCO," *Applied Physics Letters*, vol. 59, pp. 733–735, 1991.

[16] K. A. Delin and A. W. Kleinsasser, "Stationary Properties of High-Critical-Temperature Proximity Effect Josephson Junctions," *Supercond. Sci. Technol*, vol. 9, pp. 227–269, 1996.

[17] M. J. Madou, *Fundamentals of Microfabrication.* CRC Press, 2 ed., 2002.

[18] P. A. Rottier, "Establishing a Process for the Fabrication of High-Quality HTc SQUIDS," Master's thesis, University of Stellenbosch, December 2002.

[19] M. A. Lieberman and A. J. Lichtenberg, *Principles of Plasma Discharges and Materials Processing.* John Wiley and Sons, Inc, 2005.

[20] D. Boonyawan, P. Suanpoot, and T. Vilaithong, "A 13.56 MHz Multicusp Ion Source for Gaseous Ion-beam Production," *Surface and Coatings Technology*, vol. 112, pp. 314–317, 1999.

[21] G. Ashton, H. R. Kaufman, and P. J. Wilbur, "Ion Beam Divergence Characteristics of Two-Grid Accelerator Systems," *AIAA Journal*, vol. 16, no. 5, pp. 516–524, 1978.

Pectora roborant cultus recti

[22] H. Schlemm, "Ion Assisted Deposition of Optical Layers with JENION ACC-Plasma Sources." http://www.jenion.de, 2003.

[23] G. Aston and H. R. Kaufman, "Ion Beam Divergence Characteristics of Three-Grid Accelerator Systems," *AIAA Journal*, vol. 17, no. 1, pp. 64–70, 1978.

[24] H. R. Kaufman and R. S. Robinson, "Ion Source Design for Industrial Applications," *AIAA Journal*, vol. 20, no. 6, pp. 745–760, 1982.

[25] H. W. Loeb, "Plasma-based Ion Beam Sources," *Plasma Physics and Controlled Fusion*, vol. 47, 2005.

[26] M. Armacost, "Plasma-etching Processes for VLSI Semiconductor Circuits," *IBM J. Res. Develop*, vol. 43, no. 1, pp. 39–72, 1999.

[27] H. R. Kaufman and R. S. Robinson, "Ion Beam Neutralization," technical note, Kaufman and Robinson, Inc., 2003.

[28] A. R. Sampson, "Scanning Electron Microscopy." World Wide Web, December 1997.

[29] R. Wördenweber, "Growth of High-Tc Thin Films," *Supercond. Sci Technol*, vol. 12, 1999.

[30] C. V. Thompson, "Structure Evolution during Processing of Polycrystalline Films," *Annual Review of Material Science*, vol. 30, pp. 159–190, 2000.

[31] Z. Zhang and M. Lagally, "Atomistic Processes in the Early Stages of Thin-Film Growth," *Science*, vol. 276, April 1997.

[32] M. Ohring, *The Material Science of Thin Films.* Academic Press, 1992.

[33] Z. H. Barber, "The Control of Thin Film Deposition and Recent Developments in Oxide Film Growth," *Journal of Materials Chemistry*, vol. 16, pp. 334–344, 2006.

[34] D. B. Chrisey and G. K. Hubler, *Pulsed Laser Depostion of Thin Films.* John Wiley and Sons, Inc., 1994.

[35] A. Gupta and B. W. Hussey, "Laser Deposition of YBCO Film using a Pulsed Oxygen Source," *Applied Physics Letters*, vol. 58, no. 11, pp. 1211–1213, 1991.

[36] P. R. Willmott, H. Spillmann, and J. R. Huber, "Design and Synthesis of Novel Thin Films and Structures by Reactive Crossed-Beam Laser Ablation," tech. rep., University of Zurich, 1998.

[37] A. A. Voevodin, P. Stevenson, and C. Rebholz, "Active Process Control of Reactive Sputter Deposition," *Journal of Vacuum Science and Technology*, vol. 46, no. 7, pp. 723–729, 1995.

[38] C. Blue and P. Boolchanda, "In Situ Preparation of Superconducting YBCO Thin Films by On-axis RF Magnetron Sputtering from a Stoichiometric Target," *Applied Physics Letters*, vol. 58, p. 2036, 1991.

[39] U. Buttner, "The Development of Equipment for the Fabrication of Superconducting Nano-Structures." 2006.

[40] J. R. Hook and H. E. Hall, *Solid State Physics.* John Wiley and Sons, 1991.

[41] J. W. Lynn, *High Temperature Superconductivity.* Springer-Verlag New York Inc, 1990.

[42] R. S. Sokhi and P. W. Gilbert, "Investigation of Films of YBCO using Rutherford Backscattering Spectrometry," *Nuclear Instruments and Methods in Physics Research B*, vol. 50, p. 140, 1990.

[43] M. Thompson and L. Doolittle, *RBS Analysis and Simulation Package.* http://www.genplot.com, 2004.

[44] R. Y. Naidoo, *Growth and Characterisation ofThin Film Superconductors on Oxides, Silicon and Silicides.* PhD thesis, University of Cape Town, October 1993.

[45] C. L. Pettiette-Hall, J. A. Luine, J. Murduck, and J. F. Burch, "YBCO Step Edge Junctions on Various Substrates," *IEEE Transactions on Applied Superconductivity*, vol. 5, pp. 2087–2090, June 1995.

[46] F. Lombardi and Z. G. Ivanov, "The Influence of the Top and Bottom Grain Boundaries on the Current Transport in YBCO Step-edge Josephson Junctions," *Applied Superconductivity*, vol. 6, pp. 437–443, 1998.

[47] S. Tanaka, H. T. Kado, T. Matsuura, and H. Itozaki, "Step-edge Junction of YBCO Thin Films on MgO Substrates," *IEEE Transactions on Applied Superconductivity*, vol. 3, pp. 2365–2368, March 1993.

Pectora roborant cultus recti

[48] C. P. Foley, E. E. Mitchell, S. K. H. Lam, and B. Sankrithyan, “Fabrication and Characterisation of YBCO Single Grain Boundary Step Edge Junctions,” *IEEE Transactions on Applied Superconductivity*, vol. 9, pp. 4281–4284, June 1999.

[49] C. H. Wu and J. C. Chen, “High Quality Step-edge Substrates for High-Tc Superconducting Devices,” *Review of Scientific Instruments*, vol. 77, no. 033901, pp. 1–6, 2006.

[50] J. Wang, J. B. Han, G. Chen, Q. Yang, and T. Cui, “Micromachining of Highly Reproducible Step Substrates for High-Tc Step Junction DC-SQUIDs,” *Microsystem Technologies*, vol. 9, no. 480-483, 2003.

[51] H. R. Yi, Z. G. Ivanov, and D. Winkler, “Improved Step Edges on Substrates by using Amorphous Carbon Etch Masks,” *Applied Physics Letters*, vol. 65, pp. 1177–1179, August 1994.

[52] C. L. Pettiette-Hall and J. A. Luine, “YBCO Step Edge Junctions on Various Substrates,” *IEEE Transactions on Applied Superconductivity*, vol. 5, pp. 2087–2090, June 1995.

[53] H. H. Wang, R. P. Wang, and Y. L. Zhou, “Growth and Characterisation of PBCO Thin Film Used as Template Layer on STO Substrate,” *Journal of Superconductivity*, vol. 13, no. 3, pp. 447–451, 2000.

[54] Conductus, *Mr. SQUID User’s Guide*. Conductus Inc, 969 West Maude Avenue, Sunnyvale, California, USA, 2 ed., 1992.

[55] R. Keiner and P. Muller, “Intrinsic Josephson Effects in High-Tc Superconductors,” *Physical Review B*, vol. 49, no. 2, pp. 1327–1339, 1994.

[56] M. Daumling, E. Sarnelli, P. Chaudhari, and A. Gupta, “Critical Current of a High-Tc Josephson Grain Boundary Junction in High Magnetic Field,” *Applied Physics Letters*, vol. 61, pp. 1355–1357, 1992.

[57] D. T. Verebelyi, D. K. Christen, R. Feenstra, and C. Cantoni, “Low Angle Grain Boundary Transport in YBCO Coated Conductors,” *Applied Physics Letters*, vol. 76, pp. 1755–1757, 2000.

Pectora roborant cultus recti

Appendices

Appendix A

$PB_2C_3O_{7-\delta}$ Fabrication

Target Fabrication

A planar PBCO target was fabricated for use in the PLD process to realise the deposition of buffer layers in multilayer circuit fabrication. This section will describe the process followed to manufacture these targets.

The manufacture process of the $PB_2C_3O_{7-\delta}$ was performed very similar to the process followed for $YB_2C_3O_{7-\delta}$ target fabrication. Pure Pr_6O_{11}, BaO_2 and CuO powders were mixed to attain an atomic ratio of 1:2:3 for Pr, Ba and Cu respectively. This can be formulated as

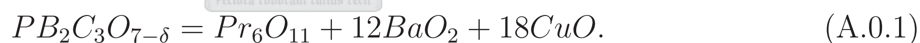

$$PB_2C_3O_{7-\delta} = Pr_6O_{11} + 12BaO_2 + 18CuO. \tag{A.0.1}$$

Pectora roborant cultus recti

The quantities (in grams) of the compounds in the 1-2-3 mixture were calculated using the molecular weights of the respective materials. Table A.1 illustrates the values used.
The compounds were measured within an accuracy of 0,0001 g to minimise the probability of secondary phase formation. The powders were thoroughly mixed and grounded with the aid of a glass mortar and pestle to yield a fine dark-gray powder. Acetone was used to assist in the mixing of the compounds.

Compound	Molecular Weight [g/mol]	Weight Used [g]
Pr_6O_{11}	1021.46	2.558
BaO_2	169.33	5.089
CuO	79.55	3.586

Table A.1: Compound weights used for PBCO fabrication

Next, the powder mixture was pressed into a planar target using a high-quality stainless steel mould. Stainless steel was suitable for this purpose to limit contamination and for its ability to withstand the pressure involved without significant deformation. 10 Tonnes of pressure was supplied by a pneumatic press to yield the moulded target. The pressed pellet is inevitably very brittle and requires extreme handling care.

After pressing the target, it was baked in a furnace with regulated oxygen flow. The temperature profile used is shown in Fig. A.1.

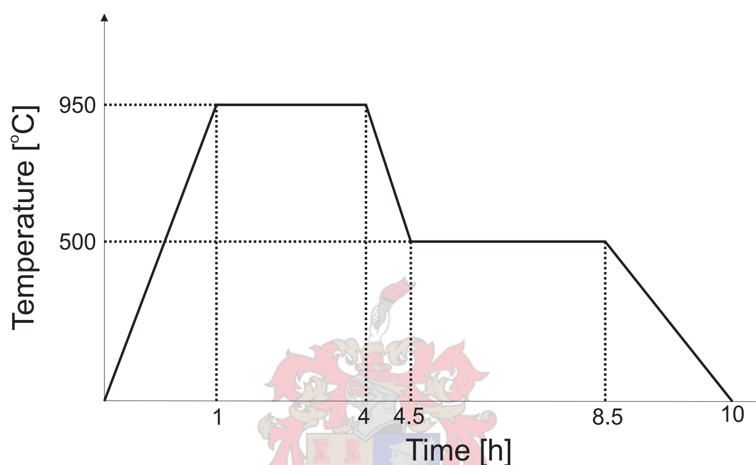

Figure A.1: Temperature profile for bake process of PBCO target

During the baking process the furnace is heated to 950 ^{o}C where the target is sintered and the compound $PB_2C_3O_6$ is formed. The furnace temperature was lower after four hours to 500°C allowing oxygenation of the target resulting in the desired $PB_2C_3O_{7-\delta}$ stoichiometry.

Appendix B

Bicrystal Fabrication

The availability of a 24° symmetric bicrystalline $SrTiO_3$ substrate coated with a 200 nm YBCO film, made it possible to perform an initial evaluation of the entire fabrication process and the proposed test setup. These substrates are, however, very expensive and not a viable method to research junction behaviour at Stellenbosch on a large scale.

The fabrication procedures included

- Photolithography
- Argon ion milling
- Deposition of gold pads by PLD.
- PCB mounting and wire-bonding

Bicrystal Alignment

The procedure followed to perform the mask alignment requires special mention. To accurately align the bicrystalline with the photoresist mask is crucial and not trivial. When the substrate is illuminated with a light source through a microscope lens, the angle of incident light to the bicrystalline is 90°. Light reflected from the bicrystalline cannot be distinguished from the light reflected from the rest of the substrate. To overcome this problem, a secondary light source was used to illuminate the bicrystal. Using an angle of incidence of about 45° to the substrate, diffraction from the bicrystalline was observed. This was used as a guideline for mask-alignment (see Fig. B.1).

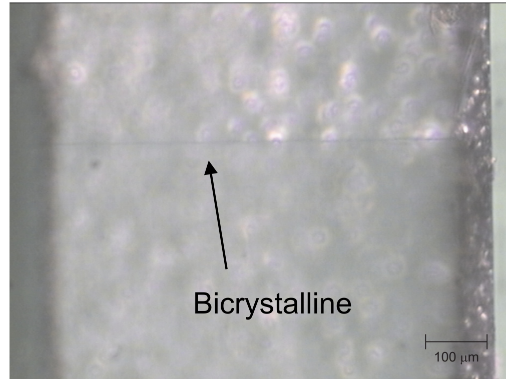

Figure B.1: Illustration of bicrystalline

Milling

The sample was milled using the high-etch mode of the Argon ion mill. The parameters used are shown in Table B.1.

V^+	V^-	I^+	V^-	Tilt angle	Mill Time
1 kV	2.5 kV	3.7 mA	3.1 mA	60°	14 min

Table B.1: Parameter set used for bicrystalline milling

Pectora roborant cultus recti

Gold Deposition and Wire Bonding

After the milling was complete, electrical contact to the patterned circuit was established by depositing gold pads by PLD (see Table B.2). An aligned metal mask ensured correct positioning of the contact pads. The sample was accordingly mounted on a PCB and gold wires were bonded between the copper tracks of the PCB and the gold pads. The bicrystal was then ready to be tested.

Testing Procedure

To test for IV characteristics, the PCB was firmly mounted in the cold finger using heat sink paste. This was followed by the proper connection of the four probe wires from the Mr SQUID Electronics unit to the circuit. After reaching temperatures below 85 K, the circuit started to show junction-like IV characteristics. This was the first working HTS Josephson junction ever fabricated at Stellenbosch.

T_{dep}	480°C
Laser frequency	16 Hz
P_{O_2}	2x10^{-1} mbar
Laser fluence	3.82 J/cm^2
Working Distance	30 mm
Focal Distance	0 mm
Deposition Time	1 h
T_{anneal}	45 min

Table B.2: The parameter set used for gold deposition

Unfortunately, the sampled reacted with water vapour upon a warm-up procedure before complete measurements could be performed. This caused severe deterioration to the sample surface and restricted any further testing of the sample. Nonetheless, the results confirmed the fact that the in-house fabrication process and test setup used were now well developed for the production and testing of JJs.

Appendix C

Argon Ion Mill Operation Procedure

Start Up Procedure

1. Turn on cooling water to the diffusion pump.
2. Open the room's window and let out the roughing pump exhaust.
3. Turn on the diffusion and the roughing pumps (Make sure the valve of the diffusion pump is closed and that the roughing pump valve is turned to the middle between roughing and backing positions).
4. Wait for 15 minutes for the diffusion pump to warm up.

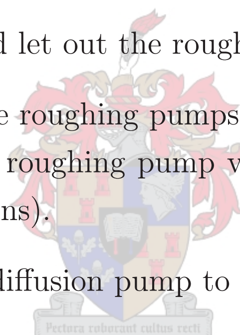

Mounting Sample Into Mill

1. The mill should initially be under vacuum. Make sure the valves to both pumps are closed before venting the system through the valve switch on the side of the workbench.
2. Remove the rf and high voltage connections.
3. Remove the head of the mill carefully to avoid excessive bending of the water pipes.
4. Cover the sample-holder with heat-sink paste for improved thermal conduction. Place the sample on the sample-holder using tweezers. Avoid touching the sample surface or allowing the paste to top the sample.
5. Orientate the sample holder tilt angle and rotational angle according to milling requirements.

6. Check the bottom chamber o-ring to make sure no particles gathered during the process of sample mounting. Remove such particles and reapply vacuum grease if necessary.

7. Carefully put back the top of the mill.

8. Reconnect the rf and high voltage cables.

Starting an Etch Process

1. Check extraction system connections according to "etch mode" requirements. The positive HV is always connected to the top grid connector mounted on the plasma chamber. For low etch rate mode connect the negative HV cable to the middle grid and ground the bottom grid. For high etch rate mode, reverse the negative HV and ground connections.

2. Close the secondary/side valve on the argon gas cylinder and open the gas inlet valve on the workbench. This will ensure that the gas feed is also rid from any reactive gases during pump down.

3. Turn the roughing pump valve to roughing. Wait for the pressure to reach 20 Torr (should take about 30 minutes if no vacuum leaks exist on the system).

4. Switch the roughing valve to backing. It now backs up the diffusion pump. Open the diffusion pump valve.

5. Switch on the high vacuum gauge. Wait for vacuum to reach 2x10^{-5} mbar. This should take about 15 minutes.

6. Switch on the water cooling to the magnets and sample holder while checking that there are no water leaks.

7. Close the argon gas inlet valve on the workbench. Open the primary and secondary valves at the argon gas cylinder.

8. Optional: Flush the system with argon gas regulated by the gas inlet on the workbench.

9. Place the cover of the mill over it to serve as protection against rf radiation.

10. Adjust the gas inlet valve on the workbench to obtain a chamber pressure of $2x10^{-4}$ mbar.

11. Switch on the rf source and set the rf input power to 50 W. Obtain impedance matching by adjusting the matching network knobs. Reflected power should be below 5 W.

12. Switch on the high voltage to the desired values (see chapter on argon mill for operating values).

13. Sample is now milled for desired time period.

Etching with Neutralisation

1. Follow the exact same procedure listed in Section “Starting an Etch Process”.

2. Now open argon inlet to PBN until a total pressure of $3.5x10^{-4}$ mbar is reached.

3. Switch on filament current source and adjust variac to obtain values ranging between 2-3.5 A. These values will vary according to filament history. Filament erosion leads to smaller current requirement. Keep a history of filament currents to aid in this respect.

4. Switch on discharge regulator and emission current sources.

Pectora roborant cultus recti

5. Adjust regulator voltage to 30 V and emission source to 50 V. Small deviations from these values may be necessary.

6. As soon as a plasma bridge is established, neutralised milling will commence.

7. If an ion measurement plate is in position, the filament current can be reduced to minimise excess electons and so prolong the lifetime of the filament.

Sample Removal

1. Turn off the high voltage.

2. Turn off the rf source.

3. If neutralisation was used, switch of filament current followed by discharge regulator and emission current sources.

4. Close gas valves on workbench and at gas cylinder.
5. Turn off the water cooling.
6. Take off the cover of the mill and remove the rf and high voltage cables.
7. Close the diffusion pump valve and turn the roughing pump valve to the middle position.
8. Switch of high vacuum gauge and only then vent the system.
9. Remove the top part of the ion mill
10. Inspect sample and remove if etching is completed.

System Shutdown

1. Replace the top chamber of the mill.
2. Turn the roughing valve to roughing. The mill should always be kept under vacuum if not in use.
3. Close roughing valve if sufficient vacuum (typically less that 50 Torr) has been reached.

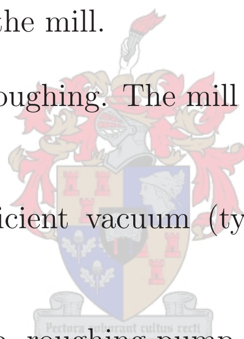

4. Switch off the diffusion pump, roughing pump and workbench.
5. Return the roughing pump exhaust inside and close the window.
6. Wait for 20 minutes before turning of the water cooling to the diffusion pump.

Appendix D

ICM Operation

Since the same vacuum system was used for the ICM and the Argon ion mill, the start-up procedures are exactly the same.

Chamber Preparation and Sample Mounting

1. After making sure that the valves to both the roughing and diffusion pumps are closed, vent the ICM system.
2. Remove all cable connections and take off the ICM-head.
3. If ICM has not been in use for a while, use a fine sanding paper to clean the cylindrical target.
4. Clean heater surface from excess silver paste from previous ICM-runs to yield a smooth surface.
5. Mount thermocouple firmly inside appropriate heater-slot with the aid of silver paste for better thermal contact. Check controller for correct temperature reading.
6. Make sure the heater configuration is mounted firmly on the water-cooled base. Center the heater to yield better film uniformity
7. Cover heater with an adequate amount of silver paste. Too much silver paste will cause bubbling during the heat-up process which may tilt the sample or top the sample edges. Do not apply the paste if the heater temperature is above 30^oC as this will harden the paste immediately and inhibit good thermal contact with the sample.

Pectora roborant cultus recti

8. Position the sample on the heater and slightly apply pressure to the sample edges for better coverage of the silver paste.

9. Check o-rings for particles (particularly silver particles). Apply vacuum grease if necessary.

10. Place ICM-head back on deposition chamber.

Starting a Deposition Process

1. Close the secondary/side valves on the argon and oxygen gas cylinders and open the gas inlet valves on the workbench.

2. Turn the roughing pump valve to roughing. Wait for the pressure to reach 20 Torr (should take about 30 minutes if no vacuum leaks exist on the system).

3. Switch the roughing valve to backing and open the diffusion pump valve.

4. Switch on the high vacuum gauge. Wait for vacuum to reach 8x10^{-6} mbar. This should take about 15 minutes.

5. Close the gas inlet valves on the workbench and open the primary and secondary valves at both gas cylinders.

6. To protect the diffusion pump during deposition, close diffusion pump valve and return the roughing pump valve to roughing. The chamber pressure should will now stabilise at 1x10^{-2} mbar.

7. Establish the appropriate gas mixture (typically 2:1 oxygen to argon) by adjusting the gas inlet valves on the workbench.

8. Switch on the water cooling to the magnets and heater while checking that there are no water leaks.

9. Turn on heater current supply and adjust variac to deliver 1.5 A. Wait until the heater temperature exceeds 150^oC (temperature at which solvent in the silver paste is baked out) before further increasing current. The resulting rate of temperature increase should prevent the silver paste from excessive bubbling.

10. Increase current to 4.1 A (should correspond to 740^oC).

11. Connect the negative terminal of the sputtering power supply to the ICM cathode and the positive terminal to ground. Ground the ICM anode and the substrate heater.

12. Switch on the power supply (operated as a constant current sources) to deliver 400 mA.

13. Sputtering now commences (see chapter on ICM for deposition rates).

Ending a Deposition Process

1. After a suitable amount of deposition time has elapsed, switch off sputtering power supply.

2. Close argon gas inlet valve on workbench.

3. Reduce heater temperature by decreasing heater current supply to 2.5 A. The temperature should now decrease to 500^oC.

4. During this cool-down process, slowly increase the oxygen flow into the chamber by adjusting the oxygen inlet valve on the workbench. At 550^oC, close the rouging pump valve.

5. At 500^oC the anneal process will commence. The chamber pressure should now be around 1 bar.

6. After following a desired anneal profile (typically 1 h duration), the current supply to the heater can be turned off. The heater temperature should now fall rapidly.

7. If the heater temperature reaches 300^oC, the oxygen gas feed valves on the workbench as well as at the gas cylinder can now be closed.

8. Remove all cable connections from the ICM and remove the ICM-head. The heater is still warm and care should be taken.

9. It was found that at these relatively high heater temperatures, it was easier to remove the samples without breaking. Sample removal is accomplished with a sharp scalpel.

The same procedure for Argon Mill shutdown applies to ICM shutdown.